UNIVERSITY OF GRANADA

FINAL MASTER PROJECT

MASTER IN PHYSICS AND MATHEMATICS

Chemical abundances in nearby galaxies from the Palomar Survey

Borja Pérez Díaz

July 2020

Directed by: Josefa Masegosa Gallego
Co-directed by: Isabel Márquez Pérez

Contents

Acknowledgments / Agradecimientos

Me gustaría agradecer en primer lugar a mis directoras de proyecto, Josefa Masegosa Gallego e Isabel Márquez Pérez, su paciencia, entrega, trabajo y cariño. No solo me han guiado durante este trabajo de investigación, sino que siempre me han ofrecido su ayuda y su tiempo para cualquier contrariedad que me pudiera encontrar a lo largo de mi primera experiencia formal investigadora. Ha sido un año enriquecedor en el que el aprendizaje constante con el equipo de Pepa e Isabel nunca ha cesado. Este año me ha marcado como investigador, como alumno y, especialmente, como persona, gracias a ellas.

En segundo lugar, quiero agradecer al Consejo Superior de Investigaciones Científicas por haberme otorgado la beca JAEIntro 2019, gracias a la cual he podido iniciar mi experiencia investigadora con el equipo de Pepa e Isabel en el Instituto de Astrofísica de Andalucía (IAA-CSIC). Quisiera extender este agradecimiento al propio IAA-CSIC y a todos sus integrantes, quienes me han hecho sentir siempre como uno más del centro y no como un mero visitante temporal. No hay palabras para describir la suerte que he tenido de poder trabajar con el equipo del IAA-CSIC: gracias a todos.

En tercer lugar, quiero agradecer a mi primer profesor de astrofísica y director de mi Trabajo Fin de Grado, Luigi Toffolatti, por haberme apoyado y motivado a continuar mis estudios en la rama de astrofísica. Gracias a sus clases en la Universidad de Oviedo descubrí este campo de la física tan apasionante, profundo e interesante.

Por último, y no por ello menos importante, quiero agradecer a mi familia y a mis amigos. Aunque la distancia y la peculiar situación de este año nos hayan separado por tanto tiempo, nunca han dejado de apoyarme, asesorarme, motivarme y, en ocasiones, aguantarme. Gracias de corazón a todos.

Abstract / Resumen

We present the results for the chemical abundances obtained from the nuclear spectra of a sample of nearby galaxies in the Palomar Spectroscopy Survey. These chemical abundances have been obtained using the code HII-CHI-MISTRY adapted for Active Galactic Nuclei (AGN). The code allows to consider both star forming galaxies and AGN, since both ionizing mechanisms are implemented on it. Whereas a number of recent works analyze the metallicity in Seyferts 2, a systematic analysis is still lacking for low-luminosity AGN, which are the most common in the local Universe. Our work provides a deep study of the metallicity in the nuclear regions of galaxies of all spectral types, providing the ionization mechanisms that leads to their emissions. Since we consider the most accurate measurements of the emission lines, we limit the original sample only for accurate measurements which amount a total of 234 galaxies: 107 are star-forming galaxies (45.7%), 23 Seyferts 2 (9.9%), 56 LINERs (23.9%) and 48 composites (20.5%). We also show how the different properties of the host galaxies, such as morphology, Supermassive Black Hole mass, absolute B-magnitude, H_α luminosity or stellar mass are related to the chemical abundances obtained for the different objects.

Keywords: Active, Nuclei, ISM, Abundances, Palomar.

Presentamos los resultados de las abundancias químicas obtenidas de espectros nucleares de una muestra de galaxias cercanas del Palomar Spectroscopic Survey. Estas abundancias químicas se han determinado usando el programa HII-CHI-MISTRY adaptado a Núcleos Galáctivos Activos (AGN). El programa permite considerar tanto galaxias con formación estelar como AGN, ya que ambos mecanismos están implementados en él. Mientras que varios estudios recientes analizan la metalicidad en Seyferts 2, aún no existe un estudio sistemático para AGN de baja luminosidad, que son los más abundantes en el Universo local. Nuestro trabajo proporciona un estudio en profundidad de la metalicidad en las regiones nucleares de galaxias de todos los tipos espectrales, teniendo en cuenta los mecanismos de ionización que originan sus emisiones. Puesto que solo consideramos líneas de emisión medidas con precisión, la muestra original del Palomar se reduce a un total de 234 galaxias agrupadas en: 107 galaxias con formación estelar (45.7%), 23 Seyferts 2 (9.9%), 56 LINERs (23.9%) y 48 galaxias compouestas (20.5%). También presentamos cómo las diferentes propiedades de las galaxias anfitrionas (morfología, masa del Agujero Negro Supermasivo, magnitud absoluta en la banda B, luminosidad en H_α o masa estelar) están relacionadas con las abundancias químicas obtenidas para los diferentes objetos.

Palabras clave: Activo, Núcleos, Medio-Interestelar, Abundancias, Palomar.

1. Introduction

This chapter provides the keys to understand the nuclear emission in galaxies and the differences between star formation and AGN photoionization. In addition, a briew review of the current state of the art in estimating chemical abundances is presented.

1.1 Active Galactic Nuclei

There are some galaxies in the Universe whose luminosity ($L \sim 10^{44} - 10^{46}\ erg \cdot s^{-1}$) cannot be explained by the nuclear fusion in stars [Woo and Urry (2002)]. The source of this excess is the accretion of matter onto a supermassive black hole (hereafter SMBH), with masses $M > 10^5\ M_\odot$ [Netzer (2015)], located in the center of the galaxy [Heckman and Best (2014); Netzer (2015)]. Those galaxies are called *Active Galactic Nuclei* (hereafter AGN). There are two arguments which favor this model: the variability, seen in small time scales, of many AGN shows that the central source is extremely compact (small size) [Peterson (2001)]; and, the asymmetric-relativistic profile of the FeKα line [Tanaka et al. (1995)].

The presence of a SMBH in the center of the galaxy is a necessary but no sufficient condition to classify a galaxy as an AGN [Netzer (2015)]. There are many galaxies that presents a SMBH but do not show any additional contribution in their luminosity[1]. Thus, an AGN is also characterized by the presence of matter in the very close neighborhood of the SMBH; during the accretion of the matter one part is translated into luminosity and the other into growth of the black hole. That luminosity is usually expressed in terms of the Eddington luminosity, which establishes an upper limit for the luminosity of any astrophysical object due to the balance between the radiation pressure and the gravitational force, that is defined as [Netzer (2015)]:

$$L_{Edd} \approx 1.5 \cdot 10^{38} \frac{M_{SMBH}}{M_\odot} \quad \left[erg \cdot s^{-1}\right] \tag{1.1}$$

The luminosity of an AGN verifies that $L_{AGN}/L_{Edd} \gtrsim 10^{-5}$ [Netzer (2015)]. The above criteria is somewhat arbitrary: it excludes our own galaxy (which is not an AGN) but it also includes the low-luminosity AGN (hereafter LLAGN), that present typical ratios of $L_{AGN}/L_{Edd} \sim 10^{-5} - 10^{-3}$ [González-Martín et al. (2009)].

The structure for an AGN can be seen in the schematic picture of Urry and Padovani [1995] (see

---

[1] For instance, our own galaxy (the Milky Way) presents a SMBH called Sagittarius A*, with a mass of $(4.148 \pm 0.014) \cdot 10^6\ M_\odot$ [The GRAVITY Collaboration et al. (2019)], but there is no sufficient matter in its neighborhood that could be constantly accreted to maintain a luminosity $L/L_{Edd} > 10^{-5}$.

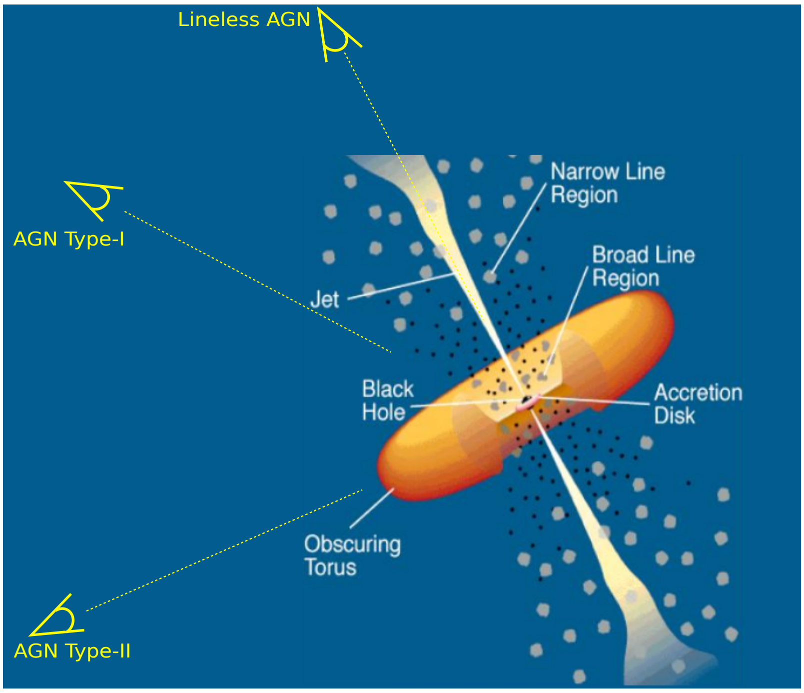

Figure 1.1: Scheme of the components of an AGN. Different types of AGN are indicated as a function of the view angle. Picture taken from Urry and Padovani [1995].

Figure 1.1). From inner to outer parts, an AGN presents:

- The **Supermassive Black Hole (SMBH)**. In the center of an AGN there is a SMBH whose activity is the responsible of the AGN luminosity. A proxy to the mass of the SMBH, that can be used for many galaxies, is an empirical function of the central velocity dispersion ($\sigma_{central}$) in the galaxy [Heckman and Best (2014)] given by:

$$\log_{10}\left(\frac{M_{SMBH}}{M_\odot}\right) = 8.32 + 5.64\log_{10}\left(\frac{\sigma_{central}}{200\ km\cdot s^{-1}}\right) \tag{1.2}$$

- The **accretion disk**. Surrounding the SMBH there is an accretion disk. The geometry of this structure changes depending on the accretion rate ($\dot{M}$) of the gas [Heckman and Best (2014); Netzer (2015)]. In order to establish a criterion for quantifying the accretion rate, the Eddington luminosity (Equation (1.1)) can be translated into an accretion rate since the luminosity of the process is given by $L = \epsilon\dot{M}c^2$, where ϵ is the efficiency of the process and $\dot{M}$ the accretion rate. Therefore, the Eddington rate is defined as:

$$L_{Edd} = \epsilon\dot{M}_{Edd}c^2 \;\Rightarrow\; \dot{M}_{Edd} = \frac{2.643\cdot 10^{-9}}{\epsilon}\frac{M_{SMBH}}{M_\odot}\ \left[M_\odot\cdot yr^{-1}\right] \tag{1.3}$$

When the accretion rate is of the same order or just below the Eddington rate, the accretion process is efficient, and the angular momentum is lost due to winds and viscosity forces in the own disk [Shao (2013)], so an inflow of gas is created. In this situation, the geometry of the disk is thin while it is optically thick [Heckman and Best (2014)]. When the accretion rate is low ($\dot{M} \ll \dot{M}_{Edd}$), the inner parts of the disk change into a geometrically thick structure, where the cooling time of the gas is larger than the inflow time so the gas flows by an advective-dominated flow, hence the formation of jets is favored [Heckman and Best (2014); Netzer (2015)].

This structure presents a radial profile of temperature $T(r)$ through its extension, from $r \sim R_{Sch}$ to $r \sim 10^3 R_{Sch}$ (being R_{Sch} the Schwarzschild radius[2]) [Hawkins (2007)]. The emission of the accretion disk extends from the ultraviolet to the soft X-ray range.

- The **hot corona**. The accretion disk is surrounded by another structure of gas with high temperatures ($T > 10^7\ K$ [Cao (2009)]), whose emission in the X-ray is not only intrinsic since it also reflects the emission of the accretion disk by Compton-reflection [Cao (2009); Meyer-Hofmeister et al. (2017)]. This structure is located at approximately $r \sim 10 R_{Sch}$ with a size from $40 - 60 R_{Sch}$ [Reis and Miller (2013)].

- The **Broad Line Region (BLR)**. At a distance of 0.01 − 1 pc [Netzer (2015)] from the SMBH, there are clouds of gas ionized by the radiation emitted from the accretion disk and the corona. These clouds emit radiation as emission lines but, due to the proximity to the black hole, those lines are broadened, as a consequence of their motion around the SMBH [Alloin et al. (2006)], with widths of $10^3 - 10^4\ km \cdot s^{-1}$ [Shao (2013)]. This is the so-called *Broad Line Region* (hereafter BLR). The detection of such broad lines is an unambiguous probe that the host galaxy has an AGN since the required temperature to generate such widths (in case they were thermal broadened $3k_B T = mv^2$) would be high enough to have all the gas completely ionized and no emission line would be detected, so the velocity of the gas is the consequence of the orbital motion of the whole cloud. The general temperature of these clouds is around $T_e \sim 10^4\ K$ and presents densities of $n_e \sim 10^9\ cm^{-3}$ [Alloin et al. (2006)].

- The **dusty torus**. There is a distance from the SMBH where the temperature T is below that required to sublimate molecular grains of dust. This is the inner radius for a structure called *dusty torus*, whose outer radius can reach 30 pc [Mor et al. (2009)]. With typical values of the column density between $10^{23} - 10^{25}\ cm^{-2}$ [Heckman and Best (2014)], this structure absorbs the radiation from the optical, ultraviolet and soft X-ray range, remitting it as thermal emission in the infrared band. For the highest columns density $> 10^{24}\ cm^{-2}$ [Comastri (2004)], the hard X-ray emission is also absorbed (these AGN are called *Compton thick AGN*), so the inner parts (accretion disk, hot corona and BLR) cannot be directly detected [Urry and Padovani (1995); Alloin et al. (2006); Heckman and Best (2014); Netzer (2015)].

- The **Narrow Line Region (NLR)**. Just from the cone aperture of the torus, another region populated with gas clouds is found. This gas also radiates energy as emission lines, as the BLR, but the width of those lines is smaller $\sim 200 - 1000\ km \cdot s^{-1}$ [Vaona et al. (2012)]. For this reason, this region is called *Narrow Line Region* (hereafter NLR). The NLR and the BLR do not only differ in the width of the emission lines, but in the distance from the SMBH (the NLR extends from the $\sim 10^2\ pc$

---

[2] For any spherical object of mass M, the Schwarzschild radius is defined as:

$$R_{Sch} = \frac{2GM}{c^2}$$

and it represents the last stable orbit.

to a few kpc [Bennert et al. (2006)]). The density in the NLR is also lower ($n_e \sim 10^2 - 10^5\ cm^{-3}$ [Alloin et al. (2006); Vaona et al. (2012); Netzer (2015)]). However the temperature is similar to that of the BLR, $T_e \sim 10^4\ K$ [Bennert et al. (2006); Alloin et al. (2006); Vaona et al. (2012)]. More details on the NLR and the BLR can be found in subsection 1.2.3.

- The **jet**. Finally, in some AGN collimated outflows (jets) can be formed, reaching the scales of Mpc [Blandford et al. (2019)] (even greater than their own host galaxy). The formation of the jets in AGN is an open question: the role of the magnetic field, the efficiency in the cooling of the gas and the accretion rate are some of the keys that many models try to determine [Shao (2013); Heckman and Best (2014); Romero et al. (2017); Blandford et al. (2019)]. Nevertheless, since those jets are made of electromagnetic particles (electrons, protons,...) accelerated at relativistic velocities, they radiate in the radio range due to synchrotron emission.

Since the first detection of an AGN [Schmidt (1963)], many attempts have been made in order to establish a taxonomy of all the types of AGN that are observed. Many examples of this classification can be found in the works of Antonucci [1993], Urry and Padovani [1995; 2017], Heckman and Best [2014] or Netzer [2015] among many others.

Following the classification by Netzer [2015], there are four main types of AGNs:

- **AGN Type-I**: These AGN are characterized by the presence of broad (widths with the same order as the BLR) emission lines [Urry and Padovani (1995); Netzer (2015)].

- **AGN Type-II**: These AGN are characterized by the lack of broad emission lines. There is a distinction between *false* AGN Type-II (AGN Type-I whose broad lines can be detected in polarized light) and *true* AGN Type-II (AGN that not present any detectable broad emission line) [Netzer (2015)], but this result is still controversial (see the review of Antonucci [2012] for more details).

- **LINERs**: These AGN present strong low-ionization emission lines. The presence or not of broad emission lines leads to a similar sub-classification as that presented above [Padovani et al. (2017)].

- **Lineless AGN**: These AGN are characterized by their extremely weak (or even undetected) emission lines and, in some cases, for their continuum variability [Netzer (2015)].

The above classification is based on an observational point of view, but some other classifications are based also on a physical point of view. For instance, Heckman and Best [2014] introduced another classification with only two types of AGN: *radiative-mode* and *jet-mode* . The main difference between these classes is that in the former one, the radiation is the most efficient energy output while in the later one is the mechanic energy associated to the relativistic jets. This is a similar (but no identical) classification to that presented by Padovani [2017], where he introduced the terms of *non-jetted* and *jetted*.

Many of these classes of AGN merge into one according to the *Unified Model of AGN* [Antonucci (1993); Urry and Padovani (1995)]. AGN Type-I and Type-II are the same, the only difference is the angle of observation: observing an AGN parallel to the dusty torus implies that the dusty torus is absorbing the emission from the BLR and, therefore, no broad lines will be detected. In addition, the lineless AGN can be explained through this model too: observing the AGN with a small angle measured from the jet implies that its radiation is beamed (this also justifies the variability in the continuum). This picture of the Unified Model can be seen in Figure 1.1. However, there are still intrinsic differences such as the presence or not of jets that lead to the classification of Heckman and Best [2014] or Padovani [2017].

The above *unification* can be used to merge different types of AGN such as Seyferts (1 and 2), radio-loud AGN or blazars. However, the extrapolation of this picture is more complicated when the LINERs are taken into account, since it is possible that the Unified Model needs, in addition to orientation, another parameter that is the luminosity of the AGN [Márquez et al. (2017)].

1.2 Spectroscopy of galaxies

In general, galaxies are gravitationally bound systems composed by stars, interstellar gas and dust (the interstellar medium, hereafter ISM) and dark matter. The stars, which are the second most perfect blackbodies in the Universe (after the Cosmic Microwave Bakground [Kolb and Turner (1990)]), radiate from the ultraviolet to the near infrared range depending on their temperature: O and B stars, which are massive ($M > 8M_{\odot}$) and hot ($T_{eff} > 10^4\ K$), emit most of their radiation in the ultraviolet and optical-blue range; K and M stars which are less massive ($M < M_{\odot}$) and cooler ($T_{eff} < 4000\ K$), emit most of their radiation in the optical-red and near infrared range [Sparke and Gallagher III (2007)]. As the stars are surrounded by ISM, part of their emission is absorbed by the dust, increasing its temperature and leading to a thermal re-emission in the infrared, and by the gas (which is mainly composed by hydrogen) that leads to absorption and emission in well determined wavelengths (spectral lines).

Therefore, most of the stellar luminosity of the galaxies is detected in the ultraviolet, optical and near infrared range of the spectrum. However, there are stars in their late stages of their evolution, such as X-ray binaries [Giacconi et al. (1962)], pulsars [Hewish et al. (1968)] or also supernovae [Galama et al. (1998)] that emit in radio, X-ray or Gamma-ray. There are some non-stellar processes that leads to emission at different ranges, for instance the bremsstrahlung emission from the ISM can be detected in the radio and X-ray ranges. In galaxies that do not host an AGN, the majority of their luminosity comes from the ultraviolet, optical and infrared range, but in AGN, as consequence of the different components (see section 1.1 for more details), the emission in other spectral ranges from radio to X-ray cannot be neglected.

1.2.1 Spectral lines: general considerations

The spectral lines are the results of the emission or absorption of photons with a particular frequency λ (a given energy $E_{\gamma} = h\nu$) that is the difference between two energy states of the quantum systems (such as atoms, ions or molecules) when radiation scatters with matter. If the initial level was above the final one, then a photon is emitted which leads to an emission line. If the initial level was below the final one, then a photon is absorbed to excite the atom and this leads to an absorption line. The stars present different molecules and atoms in their surfaces, so many spectral lines are observed in their spectrum. On the other hand, the stars are immersed in the ISM, therefore the stellar radiation scatters with the matter presented in the ISM, leading to the production of spectral lines. As a consequence of that, many emission and absorption lines can be seen in the galactic spectrum.

The interstellar gas is composed mainly by hydrogen and helium due to the Big Bang Nucleosynthesis [Burbidge et al. (1957)]. The ionization potential of the hydrogen is $E = 13.6\ eV$ while for the helium is $E = 24.6\ eV$ [Osterbrock and Ferland (2006)]. The helium presents two electrons, so it can be doubly ionized, but the energy required to ionize He^{+} is $E = 54.4\ eV$ [Osterbrock and Ferland (2006)]. The hot, massive stars that ionized the hydrogen in HII regions can also reach the ionization potential of the helium. However, the energy $E = 54.4\ eV$ is above their emission, so there is no helium doubly ionized. This is not the case in AGN, since the ionization sources are the accretion disk and the hot corona, which emit such energetic photons that not only the helium is doubly ionized, but other elements such as the neon are forth times ionized (that requires a energy $E = 97\ eV$) [Maddox (2018)]. In the optical range, considering the hydrogen, the recombination of an electron in an energy level above $n > 3$ to the level $n = 2$ leads to emission lines which are called *Balmer lines*. The corresponding wavelengths are: 4102 Å (from $n = 6$); 4340 Å (from $n = 5$); 4861 Å (from $n = 4$); and 6563 Å (from $n = 3$) [Lequeux et al. (1979)]. These lines are respectively named as H_δ, H_γ, H_β and H_α (a schematic picture of these transitions can be seen in Figure 1.2). In the case of the helium, optical emission lines from the neutral state (HeI) at the wavelengths of 3889 Å, 4026 Å, 4472 Å, 4713 Å, 4921 Å, 5876 Å, 6678 Å and 7065 Å can be detected, while in the case of the single ionized helium (HeII) there is an emission line at 4686 Å [Lequeux et al. (1979)].

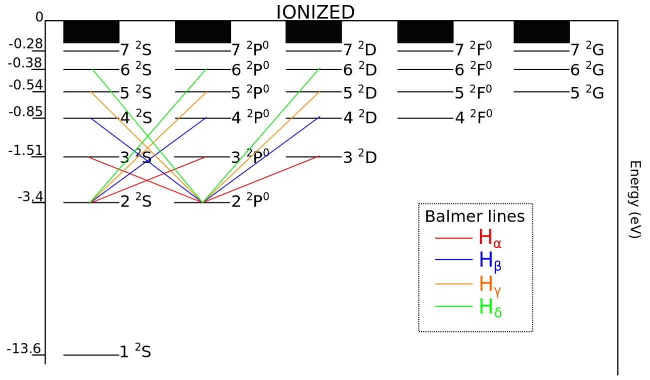

Figure 1.2: Gotrian diagram of the energy levels of the hydrogen. In different colors are represented the Balmer lines and their corresponding transitions.

In addition to the photons that excite the atoms, the collisions between atoms and electrons (or even protons) have a similar effect [Kewley et al. (2019)]. The collisions between an atom and an electron produce $A + e \rightarrow A^{*} + e$ where A is the initial state of the atom and A^{*} is the excited state. The emission line is then produced by the decay of the state, i.e., $A^{*} \rightarrow A + h\nu$. In order to observe this emission line, either the state must decay rapidly or there must be a low density of particles since any other collision could excite the A^{*} level [Sparke and Gallagher III (2007)]. These emission lines are called *collisional excited lines* (hereafter CEL).

The strength of the emission lines depends on the rate that de-excitations (from a state j to a state i) are produced.

- For the radiative ones, the rate per unit of volume is given by the density of ions in the upper level

j (N_j) and the spontaneous transition probability (A_{ji}) as [Kewley et al. (2019); Hilborn (1982)]:

$$R_{ji}^{rad} = N_j A_{j,i} = N_j \frac{2e^2\omega_{ji}^3}{3\epsilon_0 hc^3} \sum_{m_i \in i} |\langle m_i|\vec{r}|m_j\rangle|^2 \tag{1.4}$$

which only depends on the oscillation between the levels ω_{ji} (i.e. their energy) and in their quantification (but not on the temperature).

- For the CEL, the rate of excitations is expressed as [Kewley et al. (2019)]:

$$R_{ij} = n_e N_i \left[\frac{2\pi\hbar^4}{k_B m_e^3}\right]^{1/2} \frac{\Omega_{ij}}{g_i} T_e^{-\frac{1}{2}} \exp\left(-\frac{E_{ij}}{k_B T_e}\right) \tag{1.5}$$

  that depends on the quantification of the levels (E_{ij}, g_i), the number of ions in the ground level i (N_i), the density of electrons (n_e) and the so-called *collisional strength* (Ω_{ij}), whose values are tabulated thanks to numerical simulations. The de-excitation rate per unit of volume is given then by [Kewley et al. (2019)]:

$$R_{ji}^{coll} = n_e N_j \left[\frac{2\pi\hbar^4}{k_B m_e^3}\right]^{1/2} \frac{\Omega_{ji}}{g_i} T_e^{-\frac{1}{2}} \tag{1.6}$$

  The collisional strength Ω_{ij} also shows a slighty dependence with the temperature T_e.

The most important difference between these processes is that only the collisional de-excitation shows a dependence with the temperature (which is called *electronic temperature*). The electronic temperature, T_e, is defined as the average temperature of the distribution of electrons. Since the electrons are lighter than the ions, the electronic temperature is higher than the temperature of the ions.

From the above theory, the electron density (n_e) and the electronic temperature (T_e) are extremely important to quantify the CEL produced in a mass of gas, so for this main reason both parameters are used to characterize it. Another important parameter for that purpose is the *ionization parameter* q, which is defined as the ratio of the flux ionization photons for the hydrogen Φ_0 (i.e. photons with energy above 13.6 eV or wavelength below 912 Å) and the density number of hydrogen atoms n_H. This flux is always referred to the inner radius R of the gas that surrounds the ionization source [Kewley et al. (2019)]:

$$q \equiv \frac{\Phi_0}{n_H} = \frac{L\,(E > 13.6\ eV)}{4\pi R^2 n_H} \tag{1.7}$$

This parameter is defined in terms of the hydrogen ionization since it is the most abundant element in the Universe [Kolb and Turner (1990); Sparke and Gallagher III (2007); Maiolino and Mannucci (2019)]. The parameter q has units of velocity, so it can be understood as the velocity of the front of ionization from a source [Kewley et al. (2019)]. Therefore, it is more widely used [Pérez-Montero (2014); Pérez-Montero (2015); Dors et al. (2015); Kojima et al. (2017); Pérez-Montero et al. (2019); Maiolino and Mannucci (2019); Dors et al. (2019)] the dimensionless parameter U, also called *ionization parameter*, defined as [Kewley et al. (2019)]:

$$U \equiv \frac{q}{c} = \frac{L\,(E > 13.6\ eV)}{4\pi R^2 c n_H} \tag{1.8}$$

The ionization parameter U can be understood as the efficiency of the source in ionizing the environment.

1.2.2 Star-forming regions

The stellar radiation can be a source of ionization for the gas in the ISM. Since that gas is rich in hydrogen, stars must emit photons with $E_\gamma > 13.6\ eV$ in order to ionize it. This energy limit (also called *Lyman limit* [Kewley et al. (2019)]) is only reached for photons with wavelengths in the ultraviolet range. Hot and massive stars such as O and B stars are the most important stars for the ionization of the ISM. These stars have the shortest[3] life-times ($\tau \leq 2.8 \cdot 10^7\ yr$ [Sparke and Gallagher III (2007)]), and for this main reason they are called star-formation regions: observing the ionization from these stars implies that they have been formed recently. As the most abundant element is hydrogen H, which is ionized by these young stars into H^+, these masses of gas are called *HII regions* or *star-forming regions*.

Some galaxies present many young stars in their nuclei, so their nuclear spectra correspond to a huge HII region. These are the so-called *extragalactic HII regions* or *star-forming galaxies*. The effective temperature (the one considering all the ionization stars as one blackbody) of the sources are in the range of $T_{eff} \sim 10^4\ K$ and the gas is characterized by an electronic density $n_e \sim 10^2 - 10^4\ cm^{-3}$ and velocities $v \sim 10\ km \cdot s^{-1}$ [Osterbrock and Ferland (2006)]. Under these conditions, the optical spectra retrieved from them is rich in CEL and Balmer lines. The typical values of the ionization parameter are $-3.2 < \log_{10} U < -2.9$ [Kewley et al. (2019)].

1.2.3 BLR and NLR

Considering a galaxy that shows nuclear activity (a SMBH with active accretion), there are two regions where the emission lines come from: the BLR and the NLR. As explained in section 1.1, the accretion disk of an AGN emits ultraviolet radiation, which makes it another important source of photoionization for the gas. There are two different regions of gas (located at different distances) surrounding the source: the BLR and NLR. These regions present different physical conditions and, therefore, the effects of this photoionization changes:

- The BLR presents temperatures of $T_e \sim 10^4\ K$ but densities of $n_e \sim 10^9\ cm^{-3}$. As a consequence of such high densities (compared those measured in star-forming regions), only optical emission lines from the radiative recombination can be detected. Therefore, in the optical range only the Balmer lines present a width of $10^3 - 10^4\ km \cdot s^{-1}$.

- The NLR presents temperatures of $T_e \sim 10^4\ K$ and densities of $n_e \sim 10^4\ cm^{-3}$, closer to the physical conditions of the star-forming regions. As the range of the ionization (the continuum emission from the accretion disk) is greater than in star-forming regions [Osterbrock and Ferland (2006)], a wider variety of emission lines can be observed in the NLR spectra. All of these lines present smaller widths, about $\sim 500\ km \cdot s^{-1}$ [Alloin et al. (2006)].

The ionization parameter U is practically the same for both regions, but it changes through different types of AGN. For example, for Seyferts in the local Universe, the ionization parameter presents values of

---

[3] For example, the lifetime of a star like the Sun is expected to be $\tau \sim 1.2 \cdot 10^{10}\ yr$ [Sparke and Gallagher III (2007)].

$\log_{10} U \approx -2.0 \pm 0.5$ whereas for LINERs many estimations lead to $\log_{10} U \approx -3.5 \pm 1.0$ [Ho et al. (2003)].

However, the photoionization is not the only mechanism that must be considered for some AGN. Theoretical models postulate the possibility that the emission from LLAGN (such as LINERs) could arise in shocks of gas due to the interaction with jets or galactic winds [Dopita et al. (1996); Groves (2006)], and it seems to be the case in some of them [Groves (2006)]. The possibility that hot post-AGB stars and white dwarfs could be the ionization source in some LLAGN has also been proposed [Stasińska et al. (2008); Cid Fernandes et al. (2011)]. Nevertheless, this is still an open question in the current study of AGN, especially in the low-luminosity ones [Márquez et al. (2017)].

1.2.4 Extinction on the emission line fluxes

The ISM is not only composed by gas but also by dust, i.e., molecular grains with sizes of $0.00025-0.1\ \mu m$ [Kim et al. (1994)]. The dust interacts with the radiation in two ways: scattering and absorption. The combination of these two effects implies that the emission in a particular wavelength is attenuated, i.e., $I_\lambda = I_{\lambda,0} \exp\left(-\tau_\lambda\right)$ (where I_λ is the intensity detected, $I_{\lambda,0}$ is the intensity emitted by the source and τ_λ is the attenuation).

Observational data have shown that the parameter τ_λ can be expressed as $\tau_\lambda = Cf\left(\lambda\right)$, where C is a constant for each source and $f\left(\lambda\right)$ is a function of the wavelength which is practically identical for all sources [Osterbrock and Ferland (2006)]. Therefore, the dust extiction can be expressed as:

$$I_\lambda = I_{\lambda,0} 10^{-Cf(\lambda)} \tag{1.9}$$

So as to work with nebular emission, the emission lines are always normalized to the emission line H_β [Osterbrock and Ferland (2006); Pérez-Montero (2014); Pérez-Montero et al. (2019)]. By using Equation (1.9), then the ratio will be attenuated as:

$$\frac{I_\lambda}{I\left(H_\beta\right)} = \frac{I_{\lambda,0}}{I\left(H_\beta\right)_0} 10^{-C\left[f(\lambda)-f\left(H_\beta\right)\right]} = \frac{I_{\lambda,0}}{I\left(H_\beta\right)_0} 10^{-c\left(H_\beta\right)\left[\frac{f(\lambda)}{f\left(H_\beta\right)}-1\right]} \tag{1.10}$$

where the constant C has been normalized as $c\left(H_\beta\right) \equiv Cf\left(H_\beta\right)$ and $f\left(\lambda\right)$ is a function only of the wavelength and is called *extinction curve*.

The extinction curves have been studied for many years either by assuming fixed values for the most frequent emission lines [Lequeux et al. (1979)] or by giving an explicit form for the function [Seaton (1979); Howarth (1983); Cardelli et al. (1989)]. Following the parametrization by Howarth [1983], the extinction curve is calculated as:

$$f\left(\lambda\right) = \begin{cases} R_V + 2.56\left(x-1.83\right) - 0.993\left(x-1.83\right)^2 & if\ 1.83 \leq x \leq 2.75 \\ \\ \left[\left(1.86-0.48x\right)x - 0.1\right]x & if\ 0 \leq x \leq 1.83 \end{cases} \quad \text{where } x \equiv \frac{1}{\lambda\left[\mu m\right]} \tag{1.11}$$

The parameter R_V is defined as the ratio between the extinction magnitude A_V, the difference between the observed and the expected apparent magnitude of the source, and the excess color $E\left(B-V\right)$, both referred to the Johnson system of filters [Cardelli et al. (1989); Osterbrock and Ferland (2006)]:

$$R_V \equiv \frac{A_V}{E\left(B-V\right)} = \frac{A_V}{\left(m_{B,obs} - m_{V,obs}\right) - \left(m_{B,theo} - m_{V,theo}\right)} = \frac{A_V}{A_B - A_V} \tag{1.12}$$

This parameter is called *total-to-selective extinction ratio* and only depends on the grain (of the dust) composition, shape and size [Osterbrock and Ferland (2006)]. Despite this value presents a strong dependence on the line of sight (having values between $2.6 \leq R_V \leq 5.5$ [Cardelli et al. (1989)]), it is assumed to have a mean value of $R_V = 3.1$ when general diffuse ISM is considered [Osterbrock and Ferland (2006); Howarth (1983); Cardelli et al. (1989)]. The ratio R_V is also related to the coefficient $c\left(H_\beta\right)$ as [Osterbrock and Ferland (2006)]:

$$c\left(H_\beta\right) = \frac{E\left(B-V\right)}{0.707} = \frac{A_V}{0.707 R_V} \tag{1.13}$$

From the extinction curve (Equation (1.11)) it can be seen that the shorter wavelenghts (i.e. the bluest light) are more affected than the longer ones (i.e. the reddest light). This is the reason why the result of the extinction is also called *reddening*.

1.3 Diagnostic diagrams

As explained in subsection 1.2.2 and subsection 1.2.3, star-forming galaxies and AGN present emission lines in their spectra but with important differences. First of all, the width associated to the Balmer lines in AGN Type I (i.e. emission lines detected from the BLR) are not presented in star-forming galaxies since the motion of the source around a massive object (the SMBH) is required. Since the dusty torus can intercept the emission from the BLR, the above distiction between star-forming galaxies and Type-II AGN cannot be applied. The emission source in star-forming galaxies (O and B stars) is different from that on the AGN (continuum emission from the accretion disk), hence, those differences are also translated into the intensity of the emission lines in their spectra [Baldwin et al. (1981)]. In the early 1980s, Baldwin, Phillips and Terlevich proposed to use different emission line ratios to distinguish between star-forming galaxies and AGN [Baldwin et al. (1981); Veilleux and Osterbrock (1987); Kewley et al. (2006)].

The BPT diagrams are plots (see Figure 1.3) where two emission line ratios are established as the axes. Depending on the position of each galaxy, given by the value of its emission line ratios, the galaxy is classified as belonging to the group of star-forming galaxies or regions, planetary nebulae, objects photoionized by power law and objects photoionized by shock-heating [Baldwin et al. (1981)]. The emission lines (corrected from reddening) that are used to build these diagrams are[4]: $[OII]\,\lambda3727$, H_β (at $\lambda = 4861$ Å), $[OIII]\,\lambda5007$, $[OI]\,\lambda6300$, H_α (at $\lambda = 6563$ Å) and $[NII]\,\lambda6584$ [Baldwin et al. (1981)]. By using a sample of 141 objects, they showed how the different diagrams can be used. The diagram $I\left([OIII]\,\lambda5007\right)/I\left(H_\beta\right)$ vs $I\left([OII]\,\lambda3727\right)/I\left([OIII]\,\lambda5007\right)$ (Figure 1.3 (a) and (b)) allows to distinguish between all the different ionization mechanisms. The same results are obtained with the diagrams $I\left([NII]\,\lambda6584\right)/I\left(H_\alpha\right)$ vs $I\left([OII]\,\lambda3727\right)/I\left([OIII]\,\lambda5007\right)$ (Figure 1.3 (c)) and $I\left([OIII]\,\lambda5007\right)/I\left(H_\beta\right)$ vs $I\left([NII]\,\lambda6584\right)/I\left(H_\alpha\right)$ (Figure 1.3 (e)). The best diagram to distinguish between HII regions and planetary nebulae and between

---

[4] Hereafter, the notation $[OIII]\,\lambda5007$ indicates the emission line of the specific atom (in this case O^{++}) and the wavelength (in this case $\lambda = 5007$ Å).

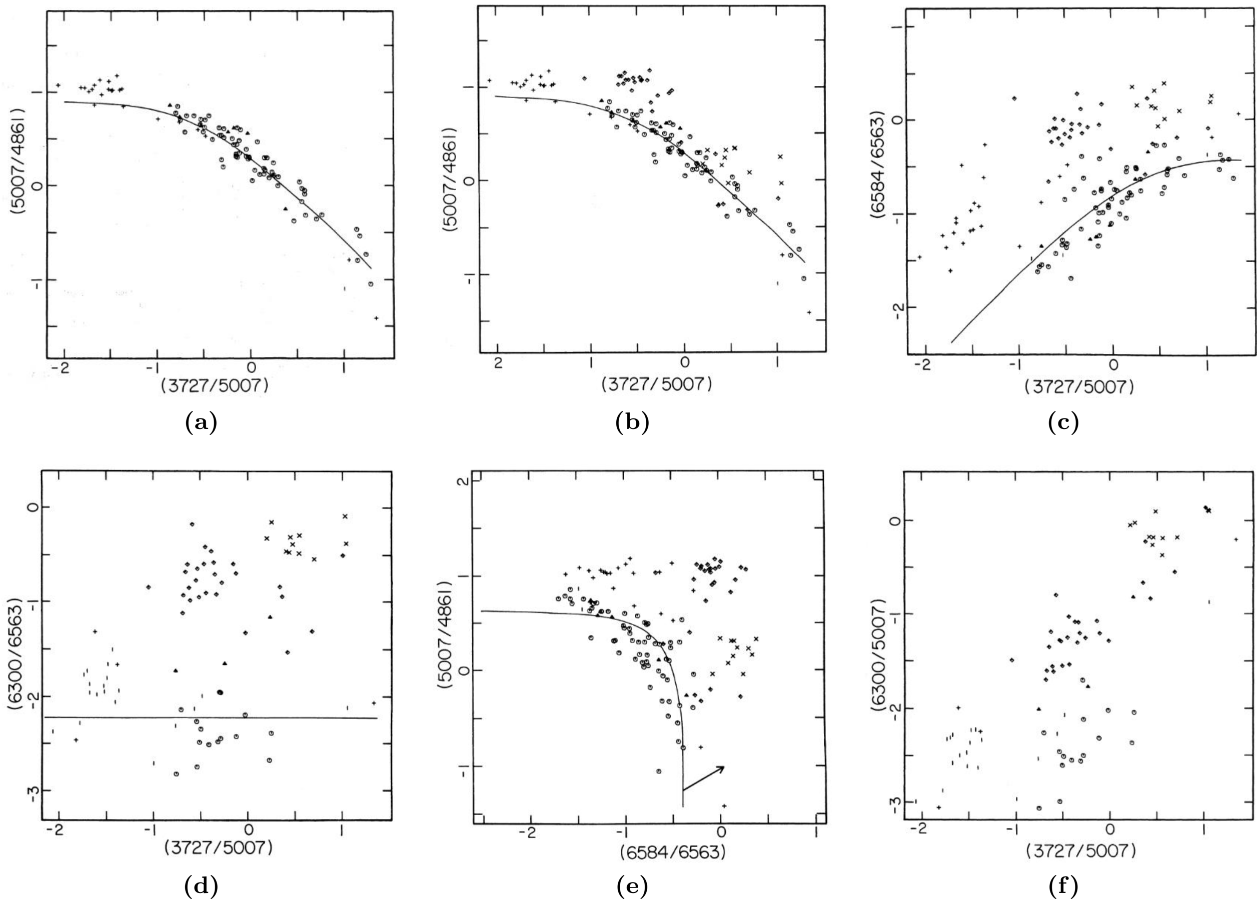

Figure 1.3: The original BPT diagrams. The emission line ratios corrected from reddening are indicated as the wavelengths between brackets. The different types of objects are: HII regions (octagons), star-forming galaxies (triangles), planetary nebulae (+), objects photoionized by power law (diamonds) and objects shock-heated (x). Taken from Baldwin, Phillips and Terlevich [1981].

power law and shock-heating ionization is $I\left([OI]\,\lambda 6300\right)/I\left(H_\alpha\right)$ vs $I\left([OII]\,\lambda 3727\right)/I\left([OIII]\,\lambda 5007\right)$ (Figure 1.3 (d)).

The BPT diagrams were constructed in many emission line ratios that are strongly affected by the interstellar extinction due to the separation in their wavelengths (see subsection 1.2.4). In order to avoid the difficulties on the measurement (due to the intensity or the blending with other lines) and the reddening (which depends also on the classification as it is discussed in section 3.1), Veilleux and Osterbrock [1987] proposed another diagnostic diagrams based on the emission lines: H_β, $[OIII]\,\lambda 5007$, $[OI]\,\lambda 6300$, H_α, $[NII]\,\lambda 6583$ and the doublet $[SII]\,\lambda\lambda 6716, 6731$. Following the same procedure as Baldwin, Phillips and Tervelich [1981], they used a sample of 264 objects (where planetary nebulae were not considered) and they proposed the diagrams $I\left([OIII]\,\lambda 5007\right)/I\left(H_\beta\right)$ vs $I\left([OI]\,\lambda 6300\right)/I\left(H_\alpha\right)$, $I\left([NII]\,\lambda 6583\right)/I\left(H_\alpha\right)$ and $I\left([SII]\,\lambda\lambda 6717, 6731\right)/I\left(H_\alpha\right)$ for distinguishing between star-forming galaxies, Seyferts 2 (AGN Type-II) and LINERs [Veilleux and Osterbrock (1987)]. In addition to the above classes, Veilleux and Osterbrock also considered *narrow emission-line galaxies* (hereafter NELG), which are galaxies with emission line ratios smaller than those measured in Seyferts 2 [Veilleux and Osterbrock (1987)]. NELG are considered to be a mixture between star-forming galaxies and LLAGN [Veilleux and Osterbrock (1987); Ho et al. (1997a)] and they are also called *transition objects* or *composite galaxies*. However, the nature of these objects remains unclear [Ho (2004); Panessa et al. (2005); Davies et al. (2014b)].

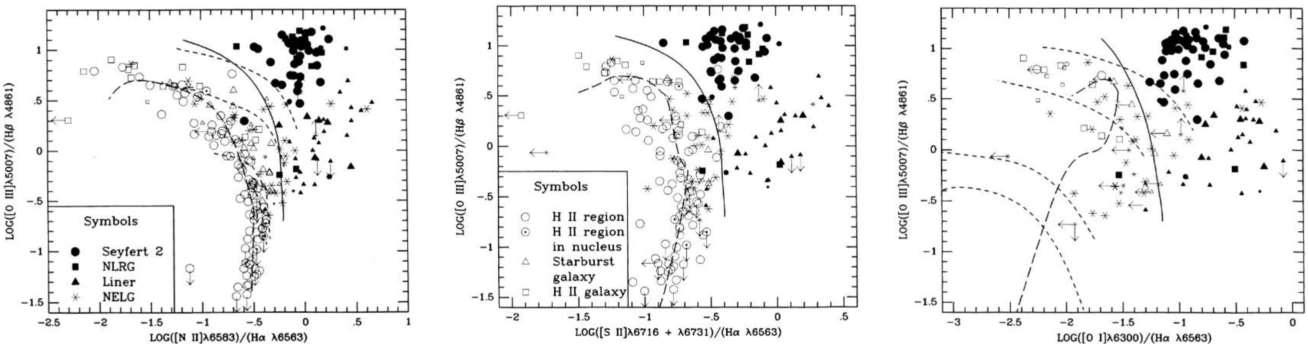

(a) (b) (c)

Figure 1.4: Diagnostic diagrams presented by Veilleux and Osterbrock [1987]. NELG are the narrow emission-line galaxies.

The three diagrams proposed by Veilleux and Osterbrock [1987] are shown in Figure 1.4. Despite not providing a criterion for separating the different regions, other authors such as Ho et al. [1997a] have proposed separators for each diagram. According to Ho et al. [1997a], there are:

- Star-forming galaxies lie in the region defined by:

$$\log_{10}\left(\left[OI\right]/H_\alpha\right) < -1.097 \tag{1.14}$$

$$\log_{10}\left(\left[NII\right]/H_\alpha\right) < -0.222 \tag{1.15}$$

$$\log_{10}\left(\left[SII\right]/H_\alpha\right) < -0.398 \tag{1.16}$$

  i.e. they verify (1.14) $\wedge$ (1.15) $\wedge$ (1.16).

- Seyferts 2 are located in the region defined by:

$$\log_{10}\left(\left[OIII\right]/H_\beta\right) \geq 0.477 \tag{1.17}$$

$$\log_{10}\left(\left[OI\right]/H_\alpha\right) \geq -1.097 \tag{1.18}$$

$$\log_{10}\left(\left[NII\right]/H_\alpha\right) \geq -0.222 \tag{1.19}$$

$$\log_{10}\left(\left[SII\right]/H_\alpha\right) \geq -0.398 \tag{1.20}$$

  i.e. they verify (1.17) $\wedge$ (1.18) $\wedge$ (1.19) $\wedge$ (1.20).

- LINERs lie in the region defined by (1.19), (1.20) and:

$$\log_{10}\left(\left[OIII\right]/H_\beta\right) < 0.477 \tag{1.21}$$

$$\log_{10}\left(\left[OI\right]/H_\beta\right) > -0.770 \tag{1.22}$$

i.e. they verify (1.21) ∧ (1.22) ∧ (1.19) ∧ (1.20).

- Finally, composite galaxies are located in the region defined by (1.21), (1.19), (1.20) and the condition:

$$-1.097 \leq \log_{10}\left(\left[OI\right]/H_\alpha\right) \leq -0.770 \tag{1.23}$$

  i.e. they verify (1.21) ∧ (1.23) ∧ (1.19) ∧ (1.20).

Thanks to spectroscopic surveys such as the *Sloan Digital Sky Survey* (hereafter SDSS), the data for a huge number of galaxies is available. As the diagnostic diagrams presented by Veilleux and Osterbrock are slightly affected by reddening, those diagrams have been tested in order of magnitudes larger samples of galaxies [Kewley et al. (2006)]. Therefore, new definitions of the regions have been presented and checked [Kewley et al. (2006)]:

- The emission lines of a star-forming galaxy must verify (1.24) ∧ (1.25) ∧ (1.26), where:

$$\log_{10}\left(\left[OIII\right]/H_\beta\right) < \frac{0.61}{\log_{10}\left(\left[NII\right]/H_\alpha\right) - 0.05} + 1.30 \tag{1.24}$$

$$\log_{10}\left(\left[OIII\right]/H_\beta\right) < \frac{0.72}{\log_{10}\left(\left[SII\right]/H_\alpha\right) - 0.32} + 1.30 \tag{1.25}$$

$$\log_{10}\left(\left[OIII\right]/H_\beta\right) < \frac{0.73}{\log_{10}\left(\left[OI\right]/H_\alpha\right) + 0.59} + 1.30 \tag{1.26}$$

- The emission lines of a composite galaxy verify (1.27) ∧ (1.28), where:

$$\log_{10}\left(\left[OIII\right]/H_\beta\right) > \frac{0.61}{\log_{10}\left(\left[NII\right]/H_\alpha\right) - 0.05} + 1.30 \tag{1.27}$$

$$\log_{10}\left(\left[OIII\right]/H_\beta\right) < \frac{0.61}{\log_{10}\left(\left[NII\right]/H_\alpha\right) - 0.47} + 1.19 \tag{1.28}$$

- The emission lines of a Seyfert 2 must verify (1.29) ∧ (1.30) ∧ (1.31) ∧ (1.32) ∧ (1.33), where:

$$\log_{10}\left(\left[OIII\right]/H_\beta\right) > \frac{0.61}{\log_{10}\left(\left[NII\right]/H_\alpha\right) - 0.47} + 1.19 \tag{1.29}$$

$$\log_{10}\left(\left[OIII\right]/H_\beta\right) > \frac{0.72}{\log_{10}\left(\left[SII\right]/H_\alpha\right) - 0.32} + 1.30 \tag{1.30}$$

$$\log_{10}\left(\left[OIII\right]/H_\beta\right) > \frac{0.73}{\log_{10}\left(\left[OI\right]/H_\alpha\right) + 0.59} + 1.30 \tag{1.31}$$

$$\log_{10}\left(\left[OIII\right]/H_\beta\right) > 1.89\log_{10}\left(\left[SII\right]/H_\alpha\right) + 0.76 \tag{1.32}$$

$$\log_{10}\left(\left[OIII\right]/H_\beta\right) > 1.18\log_{10}\left(\left[OI\right]/H_\alpha\right) + 1.30 \tag{1.33}$$

- And, finally, the emission lines of a LINER verify (1.29) ∧ (1.30) ∧ (1.31) ∧ (1.34) ∧ (1.35), where:

$$\log_{10}\left(\left[OIII\right]/H_\beta\right) < 1.89\log_{10}\left(\left[SII\right]/H_\alpha\right) + 0.76 \tag{1.34}$$

$$\log_{10}\left(\left[OIII\right]/H_{\beta}\right) < 1.18\log_{10}\left(\left[OI\right]/H_{\alpha}\right) + 1.30 \tag{1.35}$$

The new regions that Kewley et al. [2006] have proposed can be seen in Figure 2.2.

1.4 Measuring chemical abundances of the gaseous phase

The information derived from the metallicity in different regions of galaxies is key for the study of their evolution. The enrichment of the interestellar medium (ISM) is caused by the metals that are formed in the core of the stars and are driven to the surface by convective flows and deposited into the ISM by stellar winds in their final stages of their evolution.

The metallicity (Z) of a particular object is defined as the ratio between the mass of elements heavier than helium (these elements are called *metals*) and the total mass of elements (total mass of baryons) which is dominated by hydrogen and helium:

$$Z \equiv \frac{M_{metals}}{M_{baryons}} = \frac{M_{metals}}{M_{H} + M_{He} + M_{metals}} \tag{1.36}$$

Among those metal elements, the most abundant in mass is oxygen [Maiolino and Mannucci (2019)], so the metallicity is usually analyzed through the relative density numbers (N) of the oxygen to the hydrogen. This is the so called *oxygen abundance* and, in order to have always solar positive values [Asplund et al. (2009)], it is expressed as:

$$12 + \log_{10}\left(O/H\right) \equiv 12 + \log_{10}\left(N_{O}/N_{H}\right) \tag{1.37}$$

Equation (1.37) can be generalized for any other heavy element. In many publications, the oxygen abundance is said to be sub-solar, solar or supra-solar. This adjectives are assigned after a comparison with the solar value of the oxygen. The most used value for this comparison is that presented by Asplund et al. [Asplund et al. (2009)]:

$$12 + \log_{10}\left(O/H\right)_{\odot} = 8.69 \pm 0.05 \tag{1.38}$$

Another important value in the study of the chemical abundances of a gas is the ratio of nitrogen to oxygen since it is used to measure the chemical evolution. This ratio is, by definition, insensitive to the hydrogen inflows, and it is produced due to the CNO nuclear cycle in stars that can be primary (if the carbon and oxygen requiered are produced by the helium burning in massive stars) or secondary (if the carbon and oxygen are presented in the star formation due to the enrichment of the gas) [Vila-Costas and Edmunds (1993)]. This abundance is defined as:

$$\log_{10}\left(N/O\right) \equiv \log_{10}\left(N_{N}/N_{O}\right) \tag{1.39}$$

Before analyzing the different techniques that can be used to calculate or estimate the chemical abundances, two important considerations must be taken into account. First of all, the chemical abundances are just only approximations to the real metallicity, since they are calculated for a few elements. Secondly, the following review of the techniques is focused on optical measurements, but there are other tools developed to estimate them at other spectral ranges.

1.4.1 Chemical abundances in star-forming regions

This section provides a brief review of the different techniques or methods that can be applied to calculate the chemical abundances (i.e. the values (1.37) and (1.39)) of the ISM presented in such regions.

The electronic temperature T_e method (direct method)

The flux of each CEL is characterized by the abundance of the element that originates it (the ionic specie), so once the emissivity of the line (the efficiency in the thermal emission) is measured, the chemical abundance of the element is constrained [Maiolino and Mannucci (2019)]. The volumetric emissivity of a CEL produced by an atom X, as a consequence of the excitation to an upper level B and the radiative de-excitation to the level A (this de-excitation can only occur in low density regimes), can be calculated as [Osterbrock and Ferland (2006)]:

$$J_{BA} \approx n_e n_X \exp\left[-\frac{E_{BA}}{k_B T_e}\right] \tag{1.40}$$

where n_e is the electronic density, T_e the electronic temperature, E_{BA} the energy difference between the two levels and n_X the density of the ion (the reason why this method leads to a constrain in the chemical abundance). Therefore, it is necessary to measure n_e and T_e, and to do that, other emission lines must be used.

The electronic density (n_e) is usually calculated from doublets of emission lines that are extremely sensible to this parameter. This is the case for the doublet $[SII]\,\lambda\lambda 6717, 6731$, that allows its calculation. Nowadays, there are many codes (such as PYNEB in Python) or subroutines (such as the task *temden* in IRAF) that calculate it. In addition, it is required an initial value of the electronic temperature T_e [Osterbrock and Ferland (2006)].

The electronic temperature (T_e) requires the measurement of the *auroral lines*, which are $[OIII]\,\lambda 4363$, $[NII]\,\lambda 5755$, $[NeIII]\,\lambda 3343$ and $[SIII]\,\lambda 6312$. These emission lines are extremely difficult to measure, but their measurement in combination to other CEL lines allow the calculation of T_e. For example, in the case of the oxygen, the relation is given by [Osterbrock and Ferland (2006)]:

$$\frac{I\left([OIII]\,\lambda 4949\right) + I\left([OIII]\,\lambda 5007\right)}{I\left([OIII]\,\lambda 4363\right)} = \frac{7.90 \exp\left(\frac{3.29\cdot 10^4\ K}{T_e}\right)}{1 + 4.5\cdot 10^{-4}\frac{n_e}{\sqrt{T_e}}} \tag{1.41}$$

Again, the problem that the parameters n_e and T_e are coupled in their calculation is presented.

Once these two parameters are retrieved, the abundances of the ionized oxygen O^+, O^{++}, the ionized nitrogen N^+ and the ionized hydrogen H^+ can be calculated by Equation (1.40), using emission lines as $[OII]$, $[OIII]$, $[NII]$ and any Balmer line. Then, the chemical abundances are assumed to be [Pérez-Montero and Contini (2009); Pérez-Montero (2014)]:

$$O/H \approx O^+/H^+ + O^{++}/H^+ \tag{1.42}$$

$$N/O \approx N^+/O^+ \tag{1.43}$$

where the notation used in Equations (1.37) and (1.39) is followed.

This method presents therefore two problems. First, the essential parameters needed to use Equation (1.40) are coupled: it is necessary to estimate (or assign) previously one of them to calculate the other. This is an avoidable problem since both can be just calculated in an iterative process that could stop when the difference between the new calculation and the last one are below an specific limit (the precision of the technique). Secondly, the lines required to calculate T_e are extremely faint (between 10-100 times fainter than the Balmer lines [Maiolino and Mannucci (2019)]) so this method is not always possible to be used.

Photoionization models

An alternative to the direct method of the chemical abundances is the use of photoionization models to replicate the emission lines that are detected from the spectra. The method consists on employing a computational code to generate a grid of ionization sources (varying the ionization parameter U and the effective temperature of the stars T_{eff}) and another grid of the metallicity $12 + \log_{10}(O/H)$ for the gas. For each grid, the resulting theoretical spectrum is calculated and used to match the emission lines (the code inputs) to the optimal parameters (U, T_{eff} and $\log_{10}(O/H)$). [Pérez-Montero et al. (2019)]. Consequently, not only the metallicity is derived, but also the ionization parameter, which has an important effect in the emission line fluxes [Osterbrock and Ferland (2006)]. Examples of this code are CLOUDY, Mappings or NebulaBayes [Maiolino and Mannucci (2019); Pérez-Montero et al. (2019); Thomas et al. (2019); Carvalho et al. (2020)].

Despite this method is an approach not based on any empirical or semi-empirical calibration (as we will discuss later with the estimators), it also presents a critical problem. A photoionization model depends on many parameters and, thus, it is necessary to fix some of them such as the geometry. In addition to this, some of them also fix relations between metallicity parameters such as $12 + \log_{10}(O/H)$ and $\log_{10}(N/O)$ which makes them semi-empirical methods [Maiolino and Mannucci (2019)]. Additionally, the codes must present an important balance between the complexity of the code and the computational time.

Empirical calibrations based on strong optical emission lines

The direct method presents a great disadvantage since it requires the measurement of extremely faint emission lines, such as $[OIII]\,\lambda 4363$. In order to obtain more tools to analyze the chemical abundances in large sample of galaxies, many attempts have been made to calibrate the chemical abundances derived from the direct method (or through photoionization models) with other emission line ratios which can be measured for almost all the galaxies. This constitutes the basis of the estimators based on strong emission lines.

In the last years, there has been many improvements in those estimations. A thorough discussion has been published in the review by Maiolino and Manucci [2019]. Our attention will be focused on the estimators based on optical strong emission lines (specially, in the estimators R23, O3N2, N2O2 and N2S2).

- One of the estimators that can be used to calculate the chemical abundance is the so called R23

[Pagel et al. (1979)] defined as:

$$R23 \equiv \log_{10}\left(\frac{I\left([OII]\,\lambda 3727\right)+I\left([OIII]\,\lambda\lambda 4959,5007\right)}{I\left(H_{\beta}\right)}\right) \tag{1.44}$$

that uses both states of ionization of oxygen, i.e., O^{+} and O^{++}. As discussed since its proposal, the main problem with this parameter arises in that it is doubly valued as can be seen in the most recent parametrization [Strom et al. (2018)]:

$$\begin{aligned} &\text{Upper branch} \quad 12+\log_{10}\left(O/H\right)=8.24+\sqrt{0.85-0.87\cdot R23} \\ &\text{Lower branch} \quad 12+\log_{10}\left(O/H\right)=8.24-\sqrt{0.85-0.87\cdot R23} \end{aligned} \tag{1.45}$$

In addition to this problem, the estimator R23 highly depends on the ionization parameter U (for instance, the initial calibrations used estimators of the ionization parameter [Kobulnicky et al. (1999)]) so this estimator is frequently used with the estimator O32 defined as:

$$O32 \equiv \log_{10}\left(\frac{I\left([OIII]\,\lambda 5007\right)}{I\left([OII]\,\lambda 3727\right)}\right) \tag{1.46}$$

based on the recent parametrization [Strom et al. (2018)]:

$$\log_{10}\left(U\right)=0.79\cdot O32-2.95 \tag{1.47}$$

An additional problem to the R23 estimator is that, since the CEL $[OII]\,\lambda 3727$ and the Balmer line H_{β} (with $\lambda 4861$) are considerably separated in wavelength, it is affected by reddening.

- In order to solve the problem of the reddening in the R23 estimator, it was proposed the estimator O3N2 [Alloin et al. (1979)] defined as:

$$O3N2 \equiv \log_{10}\left(\frac{I\left([OIII]\,\lambda 5007\right)}{I\left([NII]\,\lambda 6584\right)}\frac{I\left(H_{\alpha}\right)}{I\left(H_{\beta}\right)}\right) \tag{1.48}$$

Since each CEL is referred to its closest Balmer line, the ratio is not significantly affected by dust extinction, and the problem of the double valuation also disappears for this estimator. The most recent parametrization establishes the relation [Strom et al. (2018)]:

$$12+\log_{10}\left(O/H\right)=8.75-0.21\cdot O3N2 \tag{1.49}$$

- Another widely used estimator for the chemical abundances in galaxies is N2O2 [Kewley and Dopita (2002)] defined as :

$$N2O2 \equiv \log_{10}\left(\frac{I\left([NII]\,\lambda 6584\right)}{I\left([OII]\,\lambda 3727\right)}\right) \tag{1.50}$$

which estimates the relative abundance of nitrogen to oxygen (N/O) through the parametrization [Strom et al. (2018)]:

$$\log_{10}\left(N/O\right)=0.51\cdot N2O2-0.65 \tag{1.51}$$

but also presents the problem that, due to the separation in wavelength of the CEL, it is affected by reddening.

- Another estimator to trace the N/O ratio is the N2S2 [Kewley and Dopita (2002)] defined as:

$$N2S2 \equiv \log_{10}\left(\frac{I\left([NII]\,\lambda 6584\right)}{I\left([SII]\,\lambda\lambda 6717, 6731\right)}\right) \tag{1.52}$$

  by using the parametrization [Strom et al. (2018)]:

$$\log_{10}\left(N/O\right) = 0.85 \cdot N2S2 - 1.00 \tag{1.53}$$

These estimators can be classified as oxygen abundance (R23, O3N2) and nitrogen abundance (N2O2, N2S2) estimators. However, by assuming a relation between O/H and N/O abundances, all of them can be used in the determination of any of these abundances.

1.4.2 Chemical abundances in AGN

In the case of AGN, it is widely accepted that the main mechanism responsible for the emission in the NLR is photoionization [Shuder (1981); Alloin et al. (2006); Nagao et al. (2006); Thomas et al. (2019); Dors et al. (2019); Pérez-Montero et al. (2019)]. In these cases, the radiation comes from the accretion disk that surrounds the SMBH in the center of the galaxy. Since the source of radiation varies between star-forming galaxies and AGN, those differences are also translated into the estimations of chemical abundances that were reviewed above.

The electronic temperature T_e method (direct method)

Assuming the photoionization emission in the NLR of AGN, the same T_e-method presented for star-forming regions can be applied to AGN. In addition, T_e-method in AGN is parametrized by separating two ionization zones (high and low) that is valid for the typical range of electronic densities n_e (that are calculated with the same method as in the case of star-forming regions) presented in those regions:

- In the high-ionization zone, the electronic temperature is calculated by the parametrization [Dors et al. (2015)]:

$$\frac{T_{e,high}}{10^4\ K} = 0.8254 - 0.0002415\frac{I\left([OIII]\,\lambda 4959\right) + I\left([OIII]\,\lambda 5007\right)}{I\left([OIII]\,\lambda 4363\right)} + 47.77\frac{I\left([OIII]\,\lambda 4363\right)}{I\left([OIII]\,\lambda 4959\right) + I\left([OIII]\,\lambda 5007\right)} \tag{1.54}$$

  Then, Equation (1.54) is used to calculate the abundance of the ionized oxygen O^{++} relative to H^+ as [Dors et al. (2015)]:

$$12 + \log_{10}\left(O^{++}/H^{+}\right) = \log_{10}\left(\frac{I\left([OIII]\,\lambda 4959\right) + I\left([OIII]\,\lambda 5007\right)}{I\left(H_\beta\right)}\right) + 6.144 + \frac{1.251 \cdot 10^4\ K}{T_{e,high}}$$

$$- 0.55 \log_{10}\left(\frac{T_{e,high}}{10^4\ K}\right) \tag{1.55}$$

- In the low-ionization zone, the electronic temperature is calculated from the high-ionization one by the relation [Dors et al. (2015)]:

$$\frac{T_{e,low}}{10^4\ K} = \frac{1}{\frac{6.93\cdot 10^3\ K}{T_{e,high}} + 0.281} \tag{1.56}$$

With this temperature, the abundances of ionized oxygen O^+ and N^+ can be calculated as [Dors et al. (2015); Kojima et al. (2017)]:

$$12 + \log_{10}\left(O^+/H^+\right) = \log_{10}\left(\frac{I\left([OII]\,\lambda 3727\right)}{I\left(H_\beta\right)}\right) + 5.992 + \frac{1.583\cdot 10^4\ K}{T_{e,low}}$$

$$- 0.681 \log_{10}\left(\frac{T_{e,low}}{10^4\ K}\right) + \log_{10}\left(1 + 2.3\frac{n_e}{10^4\ cm^{-3}}\right) \tag{1.57}$$

$$\log_{10}\left(N^+/O^+\right) = \log_{10}\left(\frac{[NII]\,\lambda 6584}{[OII]\,\lambda 3727}\right) + 0.400 - \frac{7.26\cdot 10^3\ K}{T_{e,low}}$$

$$- 0.02 \log_{10}\left(\frac{T_{e,low}}{10^4\ K}\right) + 0.007\frac{T_{e,low}}{10^4\ K} \tag{1.58}$$

With the above calculations, the relative abundances of $12 + \log_{10}(O/H)$ and $\log_{10}(N/O)$ are calculated with the approximations (1.42) and (1.43) respectively. The differences between this method and the T_e-method for star-forming galaxies are presented in the coefficients of the relations.

Photoionization models

The methodology employed to derive chemical abundances in star-forming regions using models to reproduce the emission lines ratios observed in the spectra can be applied for AGN, with the only difference that those models must reflect the difference in the source of ionization (from young-massive stars to accretion disks). Therefore, instead of varying the effective temperature T_{eff} (which is a property of the ionizing stars) these codes vary the power law that characterizes the emission from the inner parts of the AGN [Pérez-Montero et al. (2019)].

Empirical calibrations based on strong optical emission lines

The T_e-method for AGN lies on the measurement of the auroral lines, which are difficultly measured. Thus, in the same way as for star-forming galaxies, calibrations for the chemical abundances based on the same estimators as the ones used in star-forming galaxies have been attempted.

- The first calibrations derived for AGN where presented by Storchi-Bergmann et al. [1998]. These calibrations do not use any of the estimators defined for star-forming galaxies (see subsection 1.4.1), but they are constructed upon the same recurrent emission lines. For the first one, they defined the parameters:

$$x \equiv \log_{10}\left(\frac{I\left([NII]\,\lambda\lambda 6548, 6584\right)}{I\left(H_{\alpha}\right)}\right) \quad ; \quad y \equiv \log_{10}\left(\frac{I\left([OIII]\,\lambda\lambda 4959, 5007\right)}{I\left(H_{\beta}\right)}\right) \tag{1.59}$$

which are slightly affected by reddening (see subsection 1.2.4 for more details). Their relation to obtain the chemical abundance is:

$$\begin{aligned}(O/H)_1 &= 8.34 + 0.212x - 0.002y + 0.007xy - 0.002x^2y \\ &+ \left(6.52 \cdot 10^{-4}\right) y^2 + \left(2.27 \cdot 10^{-4}\right) xy^2 + \left(8.87 \cdot 10^{-5}\right) x^2y^2\end{aligned} \tag{1.60}$$

For the second calibration, they defined the parameters:

$$u \equiv \log_{10}\left(\frac{I\left([OII]\,\lambda\lambda 3727, 3729\right)}{I\left([OIII]\,\lambda\lambda 4959, 5007\right)}\right) \quad ; \quad v \equiv \log_{10}\left(\frac{I\left([NII]\,\lambda\lambda 6548, 6584\right)}{I\left(H_{\alpha}\right)}\right) \tag{1.61}$$

where the first parameter is highly dependent on the dust extinction. The relation to obtain the chemical abundance is:

$$\begin{aligned}(O/H)_2 &= 8.643 - 0.275u + 0.164u^2 + 0.655v - 0.154uv - 0.021u^2v + 0.288v^2 \\ &+ 0.162uv^2 + 0.0353u^2v^2\end{aligned} \tag{1.62}$$

For both parametrizations, the results show that a correction is needed, [Storchi-Bergmann et al. (1998); Dors et al. (2019)] based on the electronic density n_e (that must be obtained in the same way as the T_e-method):

$$(O/H) = (O/H)_{1,2} - 0.1\log_{10}\left(\frac{n_e}{300\ cm^{-3}}\right) \tag{1.63}$$

- In the recent years, another calibration was proposed based on the estimator N2O2 (1.50). The derived calibration is [Castro et al. (2017)]:

$$12 + \log_{10}\left(O/H\right) = 12 - 3.31\log_{10}\left(1.08 \cdot N2O2^2 + 1.78 \cdot N2O2 + 1.24\right) \tag{1.64}$$

In both cases, only the relative abundance of oxygen to hydrogen is derived because all of the calibrations assume a relation between N/O and O/H, based on the results obtained for star-forming galaxies.

1.5 The Palomar Spectroscopic Survey

Between 1982 and 1990, a spectroscopic survey was carried out at the Palomar Observatory, with the Double Spectrograph in the Hale 5m telescope [Ho et al. (1995)]. This is the so-called *Palomar Spectroscopic Survey* (hereafter Palomar Survey). The magnitude limit for the survey [Ho et al. (1995)] was $B_T \leq 12.5$ and, as a consequence of the position of the observatory, all galaxies in the survey have $\delta > 0$. In total, the spectra from 486 galaxies in the local Universe were retrieved thanks to this survey. The sample of galaxies observed constituted a complete survey of the local Universe, having lead to the discovery of four Seyfert galaxies that had not been previously observed and probing that LLAGN were the most abundant. Due to the effective aperture of 2”x4” of the spectrograph, the Palomar Survey provides the spectra from the nuclear regions (i.e. $r \leq 200$ pc) of nearby galaxies. The spectra, with a resolution of 4Å for short (blue) wavelengths and 2.5Å for long (red) wavelengths, cover the optical ranges of 4200Å-5200Å and 6200Å- 6900Å [Ho et al. (1995)].

The Palomar Survey was studied in great detail by Ho et al. [1995; 1997a; 1997b; 1997c; 2003; 2009], where they also presented the spectra of the galaxies after subtracting the contribution from the stellar population. To achieve that, they used templates (constructed from spectra of well-known galaxies) to match each galaxy and, thus, assigning the stellar contribution. Once this component was subtracted, there are two possibilities: either the final spectrum does not show any particular emission or either it shows and additional contribution primarily from emission lines. In the first situation, the galaxy adjusts well to the template galaxy and, therefore, it does not show any nuclear emission. Since it was the case for 68 galaxies, the original sample of 486 galaxies was reduced to 418 galaxies with nuclear emission [Ho et al. (1997a)].

In addition, many physical properties of the host galaxies were compiled from the literature [Ho et al. (1997a,b, 2009)], which makes this survey one of the most complete of AGN and their environment in the local Universe. However, the metallicity in this sample has only been studied for individual galaxies (as is the case of NGC 3998 [Devereux (2017)]) or for particular types of galaxies (ellipticals [Tang et al. (2009)], star-forming galaxies [Pilyugin et al. (2004)] or Seyferts 2 [Dors et al. (2015)]), but not for all type of galaxies with a systematic methodology.

2. Sample and methodology

This chapter presents the construction of our sample of galaxies from the Palomar Survey, justifying the different criteria used to select them. Finally, a discussion on the technique employed to estimate chemical abundances is also provided.

2.1 Selection of the sample

While the Palomar Survey presents a limited coverage (from 4200Å to 5200Å and from 6200Å to 6900Å) and other surveys improve this range (for instance the SDSS has a coverage from 3900Å to 6200Å and from 5800Å to 9200Å [Anderson et al. (2001)]), the choice of the former one has been made upon several reasons.

The Palomar Survey constitutes a complete spectroscopic optical survey of the local Universe. Since the publication of the first paper related to this survey by Ho et al. [1995], many others were published analyzing different aspects for both the host galaxies and their nuclear regions [Ho et al. (1997a,c,b, 2003, 2009)]. As a consequence of these studies, a considerable amount of ancillary data can be used to study the chemical abundances in relation to other properties of the galaxies.

LLAGN are well represented in the Palomar Survey, being the most abundant type of AGN. However, systematic studies on chemical abundances are rather scarce. Most of them have being devoted to star-forming galaxies [Strom et al. (2018); Maiolino and Mannucci (2019)] and the NLR of high-luminosity AGN [Dors et al. (2019); Maiolino and Mannucci (2019); Carvalho et al. (2020)]. Therefore, our study of the metallicity of the NLR of LLAGN by analyzing the chemical abundances in the Palomar Survey is a novel approach.

Moreover, since the Palomar Survey also includes star-forming galaxies and Seyferts, they can be also used to check the soundness of the methodology of this study (see section 2.4 for more details) and to compare the results obtained in the local Universe to those published in the recent years [Dors et al. (2015, 2019); Thomas et al. (2019); Carvalho et al. (2020)], that uses as sample galaxies from the SDSS.

In summary, the Palomar Survey provides all the data needed to carry out a detailed and systematic investigation on the chemical abundances for all spectral type of galaxies, in particular for narrow-line AGNs which is the primary goal of this project.

2.2 Filtering the sample

In order to study the chemical abundances of both extragalactic star-forming regions and NLR of AGN, the nuclear spectra of the galaxies are required (see section 1.4). Thanks to the Palomar Survey, which provides the nuclear ($r \leq 200\ pc$) spectra of nearby ($d \leq 110\ Mpc$) galaxies, the spectroscopic information of the star-forming regions and the NLR of those galaxies (if present) is accessible. The first condition that the sample must verify is that all its galaxies show nuclear emission, either due to star-formation or accretion onto a SMBH. In order to determine whether or not nuclear activity is taking place, the contribution of the stars must be previously subtracted. This work was already done by Ho et al. [1995; 1997a], who concluded that 86% of the Palomar galaxies do not show nuclear emission. Therefore, after applying the first criterion (nuclear emission in their spectra), the original sample of 486 galaxies was reduced to 418.

The nuclear emission lines can be explained by two mechanisms: star-formation or AGN activity (see section 1.2 for more details). In the case of star-forming regions, only the emission lines from the ISM ionized by young stars are measured. The case of AGN is more tricky since there are the contribution from the NLR but also from the BLR (see section 1.1). In our study, only Type-II AGN are considered, whose BLR emission is intercepted by the dusty torus. Osterbrock [1977] showed that there is a continuum of AGN between Type-I and Type-II. In the case of Seyferts, there are Seyferts 1, 1.2, 1.5, 1.8, 1.9 and 2.0, whose classification depends on the strength of the broad and narrow component of H_α and H_β. A similar classification can be applied to LINERs [Netzer (2013)]. According to Osterbrock's classification [1977; 1981], AGN with types equal or earlier to 1.5 are discarded. This is the second condition that the sample must verify. Consequently 10 objects have been excluded from the sample. The remaining AGN are Seyferts 1.8, 1.9 or 2 (hereafter they are referred as Seyferts 2) and LINERs 1.9 or 2 (herafter they are referred as LINERs).

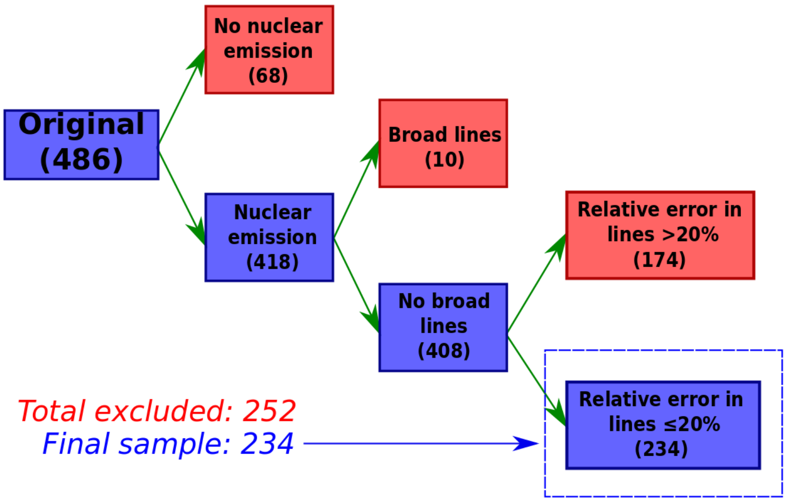

Figure 2.1: Schematic represention of the different steps (filters) that we follow to construct the final sample.

The derivation of the chemical abundances requires the measurement of emission lines, in spite of considering a simple estimator based on emission line ratios or a more sophisticated photoionization model to match the spectra (see section 1.4 for more details). To reduce the uncertainty in the chemical abundances, the emission lines must be retrieved accurately. So as to quantify this accuracy, the flux error is used: only galaxies with emission lines with a relative error up to 20% are considered. This criterion is applied not for all the emission lines but for the Balmer lines H_α and H_β and the CEL $[OIII]\,\lambda 5007$, $[NII]\,\lambda 6583$ and $[SII]\,\lambda\lambda 6717, 6731$. The choice of these emission lines is based on the following arguments: 1) they are needed to distinguish between star-forming galaxies, Seyferts and LINERs (i.e. they are used in the diagnostic diagrams); and, 2) the reddening correction of the emission lines is often applied for line ratios referred to H_β and it is also needed the use of H_α. In summary, the third (and last) condition that the galaxies of the final sample must verify is that the emission lines H_β, $[OIII]\,\lambda 5007$, H_α, $[NII]\,\lambda 6583$ and $[SII]\,\lambda\lambda 6717, 6731$ have a relative error in their flux measurement below 20%.

Considering all these restrictions (that can be easily followed in Figure 2.1), a total of 252 galaxies are excluded from the sample: 68 galaxies that do not show nuclear emission in their spectra [Ho et al. (1995)], 10 galaxies that are classified as Seyferts 1.2 or Seyferts 1.5 [Ho et al. (1997c)] and 174 galaxies that present a relative error above 20% in at least one of the emission lines required. Therefore, a final sample of 234 galaxies, composed by star-forming galaxies, Seyferts 2 and LINERs, will be used in this work.

2.3 Classification of the sample

Once the final sample is constructed, it is necessary to classify each galaxy. The sample is composed by both star-forming galaxies and Type-II AGN, so the diagnostic diagrams (see section 1.3) are used to classify the 234 galaxies. The diagnostic diagrams are based on emission lines, thus a good accuracy is required. Since this was one of the criteria to generate the sample, the spectroscopic classification is guaranteed.

In order to use a systematic classification, each diagnostic diagram is divided into the different regions that Kewley et al. [2006] proposed. However, two important considerations must be taken into account before using their criteria:

1. The equations that define the different regions in the diagrams (1.24), (1.25) and (1.26) show divergences as a consequence of the denominators. Therefore, additional restrictions to avoid problems in the classification must be added:

$$\begin{array}{l}\text{Star} - \text{forming} \\ \text{galaxies}\end{array} \left\{ \begin{array}{l} \log_{10}\left(\left[NII\right]/H_\alpha\right) < 0.05 \\ \\ \log_{10}\left(\left[SII\right]/H_\alpha\right) < 0.32 \\ \\ \log_{10}\left(\left[OI\right]/H_\alpha\right) < -0.59 \end{array} \right. \tag{2.1}$$

$$\text{Seyferts 2 and LINERs} \begin{cases} \log_{10}\left(\left[NII\right]/H_\alpha\right) > 0.47 \\ \log_{10}\left(\left[SII\right]/H_\alpha\right) > 0.32 \\ \log_{10}\left(\left[OI\right]/H_\alpha\right) > -0.59 \end{cases} \tag{2.2}$$

2. The four spectral types (star-forming galaxies, Seyferts 2, LINERs and composite galaxies) do not represent a disjointed partition of the sample, because there are some galaxies that can change their classification from one diagram to another. These objects will be called *ambiguous galaxies*.

This initial classification following Kewley's criteria (see the diagnostic diagrams in Figure 2.2) divides the sample in 103 star-forming galaxies, 47 composite galaxies, 16 Seyferts 2, 42 LINERs and 26 ambiguous galaxies. This initial result reinforces the statement that LLAGN (being LINERs a representative of this type of AGN) are the most numerous AGN in the local Universe.

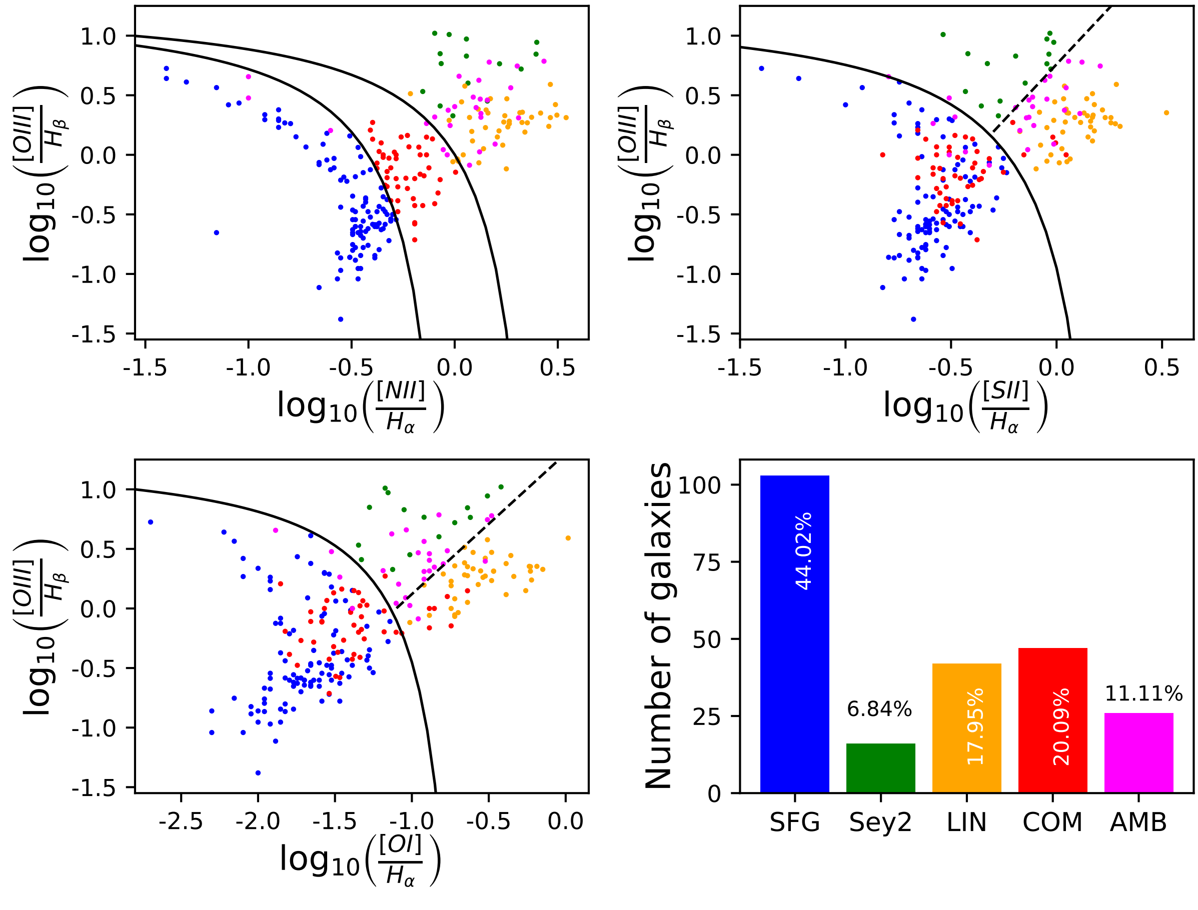

Figure 2.2: Classification on the BPT diagrams (two top panels and bottom-left) of our sample. The black lines are the limits established by Kewley [2006]. The bottom-right panel shows the statistics of each spectral class and the color codification used in this work.

In order to treat the whole sample, the ambiguous galaxies must be classified into one of the four spectral types. It should be noticed that the region of composite galaxies (given by Equations (1.27) and (1.28)) is defined only for one diagram, $I\left(\left[OIII\right]\lambda5007\right)/I\left(H_\beta\right)$ vs $I\left(\left[NII\right]\lambda6583\right)/I\left(H_\alpha\right)$, so no composite galaxy can be initially classified as an ambiguous one. In other words, the ambiguous galaxies

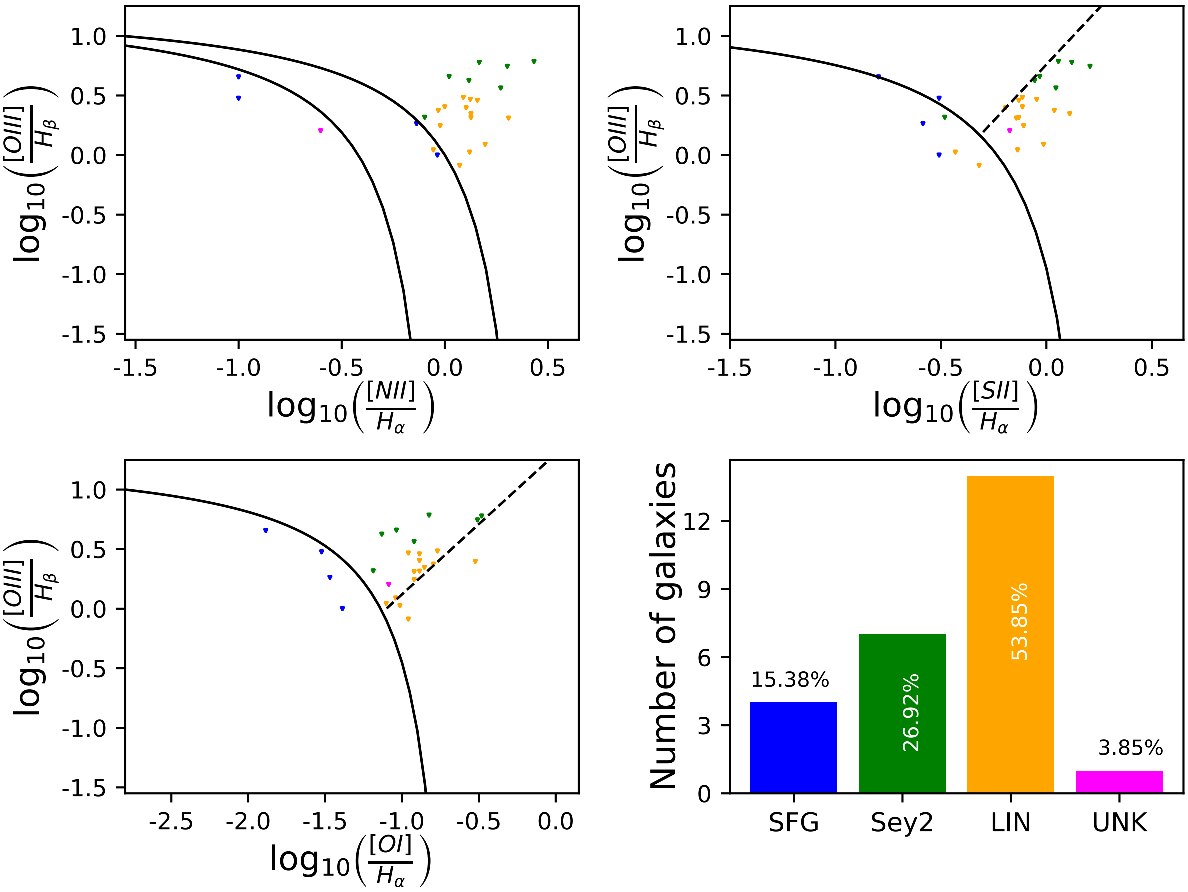

Figure 2.3: Classification of the ambiguous galaxies on the BPT diagrams (two top panels and bottom-left) of the final sample sample. The black lines are the limits established by Kewley [2006]. The bottom-right panel shows the statistics of each spectral class and the color codification.

can only be Seyferts 2, LINERs or star-forming ones. To classify the ambiguous galaxies, the criteria is smoothed and is applied to two out of the three diagrams: for instance, if a galaxy is classified as star-forming in two diagrams and as a Seyfert 2 in the other, then its classification is established as star-forming. In addition, for those AGN that in one diagram are located at the region of Seyferts and in other at the region of LINERs the Ho's criteria [1997a] is used to establish their classification.

After the classification of the ambiguous galaxies (see diagnostic diagrams in Figure 2.3), the final sample is divided in: 107 star-forming galaxies (103+4), 47 composite galaxies, 23 Seyferts 2 (16+7), 56 LINERs (42+14) and 1 unclassified galaxy. The last one, which is NGC 2541, verifies that for each diagnostic diagram it is located in a different region (see the red point in Figure 2.3). While NGC 2541 has been classified in the literature as both LINER and star-forming galaxy [Ho et al. (1997a); Filho et al. (2000)], in the present work it remains in the category of *unknown class*. For each spectral type, the ambiguous galaxies (once they are classified by the second iteration) are distinguished from those that were clearly classified in the first iteration, despite treating them as one class.

Spectral type	Non Ambiguous	Ambiguous	Total	Percentage (%)
Star-forming	103	4	107	45.7
Seyfert 2	16	7	23	9.9
LINER	42	14	56	23.9
Composite	47	–	47	20.1
Unknown	–	1	1	0.4
Sum	208	26	234	100.0

Table 2.1: Spectral classification of the sample. The percentages are referred to the final sample made of 234 galaxies.

2.4 Methodology in the derivation of chemical abundances

2.4.1 Selection of the method

In section 1.4 a review of the current and most used methods to derive chemical abundances from optical emission lines is presented. Since the spectral information provided by the Palomar Survey covers the ranges [4200Å, 5200Å] and [6200Å, 6900Å] (optical range), the method to calculate the chemical abundances in the final sample of 234 galaxies must be based on optical emission lines in these spectral ranges.

The methods presented in section 1.4 can be used for both star-forming galaxies and AGN. The T_e-method requires the measurement of extremely faint emission lines (the auroral lines). In the final sample of 234 galaxies, just only 19 of them have the measurement of such faint lines (mostly $[OIII]\,\lambda 4363$), which implies that this method can only be applied to 8.1% of the sample. On the other hand, some authors have reported that the T_e-method leads to wrong derivations in the chemical abundances in AGN [Dors et al. (2015); Maiolino and Mannucci (2019)]. Considering all these disadvantages, the T_e-method is discarded for our study.

Calibrations based on strong optical emission lines have being studied for many decades in the case of star-forming galaxies [Kobulnicky et al. (1999); Strom et al. (2018); Maiolino and Mannucci (2019)], although those calibrations presents several problems in the case of AGN. First of all, they have been only tested for Seyferts [Storchi-Bergmann et al. (1998)] but not for LINERs. Secondly, all the calibrations assumed a fixed relation between the abundances O/H and N/O which has been determined only in star-forming galaxies [Maiolino and Mannucci (2019)]. Finally, due to the spectral coverage of the Palomar Survey, the CEL $[OII]\,\lambda 3727$ is not measured for all galaxies, so in the case of star-forming galaxies only the calibrations for R23 (1.45) and O3N2 (1.49) can be used while in AGN only the calibration in Equation (1.60) can be applied. For all these reasons, the strong calibrations are not selected as the method to calculate chemical abundances.

Therefore, the photoionization models is the tool in this study for estimating chemical abundances. Among all the codes available (see subsection 1.4.2) to make such a study, HII-CHI-MISTRY (hereafter HCm) is being used for several reasons. First of all, while the HCm code was originally designed to calculate chemical abundances in star-forming galaxies [Pérez-Montero (2014); Pérez-Montero (2015)], a recent upgrade has been published so it can be also used for AGN [Pérez-Montero et al. (2019)]. In addition, the code does not make any assumption on the relation between O/H and N/O: they are calculated independently. Finally, the author of the code, Enrique Pérez-Montero, currently works in the same institution where this project was carried out, providing the possibility of a cooperative work that lead to an improvement of the code that is explained below.

2.4.2 The HCm code

The principle of work of the code is to match the emission lines ratios by using photoionization models to fix the following variables: 1) the source of the ionization (star-forming or AGN); 2) the chemical abundance $12+\log_{10}(O/H)$; 3) the chemical abundance ratio $\log_{10}(N/O)$; and, 4) the ionization parameter $\log_{10}(U)$. For the photoionization models the CLOUDY code [Ferland et al. (2013)] is used to calculate the emission line ratios from a particular one-dimensional distribution of gas and dust, which is excited by a particular spectral energy distribution (hereafter SED) [Pérez-Montero et al. (2019)].

Depending on the spectral type, there are two type of SED that are used as input for the CLOUDY code:

- For star-forming galaxies, the SED is constructed with the code POPSTAR [Mollá et al. (2009)]. The distribution of gas and dust has a fixed value of the distance between the ionization source and the inner part of the gas distribution (when its geometry is plane-paralleled) and a ratio between the mass of dust and gas of $M_{dust}/M_{gas} = 7.5 \cdot 10^{-3}$ [Pérez-Montero (2014)].

- For AGN, the SED is constructed as the composition of two components: a Big Blue Bump (hereafter BBB), originated by the thermal emission from the accretion disk, that reaches its maximum at $13.6\,eV$, and a power law with spectral index $\alpha_X = -1$ to represent the non-thermal X-ray emission. The transition between the X-ray to ultraviolet range is presented by another power law with spectral index $\alpha_{OX} = -0.8$ or $\alpha_{OX} = -1.2$. As a consequence of the last choice, for AGN there are two SED models. The gas and dust distribution follow that characterizing the NLR of AGN (see section 1.1) [Pérez-Montero et al. (2019)].

Once the SED is selected, the program generates a model for each value of $12+\log_{10}(O/H)$, $\log_{10}(N/O)$ and $\log_{10}(U)$. The first parameter takes values between $[7.1, 9.1]$ for star-forming galaxies and between $[6.9, 9.1]$ for AGN, in both cases in steps of 0.1 dex. The second one takes values between $[-2.0, 0.0]$ in steps of 0.125 dex for both star-forming galaxies and AGN. Finally, the ionization parameter takes values in the range $[-4.0, -1.5]$ for star-forming galaxies, $[-4.0, -0.5]$ for Seyferts 2 and $[-4.0, -2.5]$ for LINERs, in all cases in steps of 0.25 dex [Pérez-Montero (2014); Pérez-Montero et al. (2019)]. Thus, a total of 21x17x11=3927 models are considered for star-forming galaxies, for Seyferts a total of 23x17x15=5865 models and for LINERs a total of 23x17x6=2346.

Originally, the grids used in LINERs where the same one as those for Seyferts, i.e., the ionization parameter also took values in the range $[-4.0, -0.5]$. After some tests, bad determinations of the ionization parameter in LINERs were obtained as a consequence of the use of all the grids in LINERs. The problem arises in a bi-valuation of the ionization parameter U. In order to avoid this problem, the range of the ionization parameter in LINERs was limited to $[-4.0, -2.5]$, which is in good agreement with previous studies [Ho (2004); Kewley et al. (2006); Alloin et al. (2006)]. A summary of the models is presented in Table 2.2.

Spectral type	**SED**	**Grids**		
		12+log$_{10}$(O/H)	**log$_{10}$(N/O)**	**log$_{10}$(U)**
Star-forming galaxies	POPSTAR Burst of 10^6 yr Ratio Dust/Gas $7.5 \cdot 10^{-3}$	[7.1, 9.1] Nº Values: 21	[-2.0, 0.0] Nº Values: 17	[-4.0, -1.5] Nº Values: 11
Seyferts	BBB max. at 13.6 eV $\alpha_X = -1$ $\alpha_{OX} = -0.8$ or -1.2	[6.9, 9.1] Nº Values: 23	[-2.0, 0.0] Nº Values: 17	[-4.0, -0.5] Nº Values: 15
LINERs	BBB max. at 13.6 eV $\alpha_X = -1$ $\alpha_{OX} = -0.8$ or -1.2	[6.9, 9.1] Nº Values: 23	[-2.0, 0.0] Nº Values: 17	[-4.0, -2.5] Nº Values: 6
Steps	-	0.1 dex	0.125 dex	0.25 dex
Nº Models	-	3927 Star-forming	5865 Seyferts	2346 LINERs

Table 2.2: Summary of the input SED and grids that the HCm code uses to calculate the chemical abundances. Information taken from Pérez-Montero [2014; 2019].

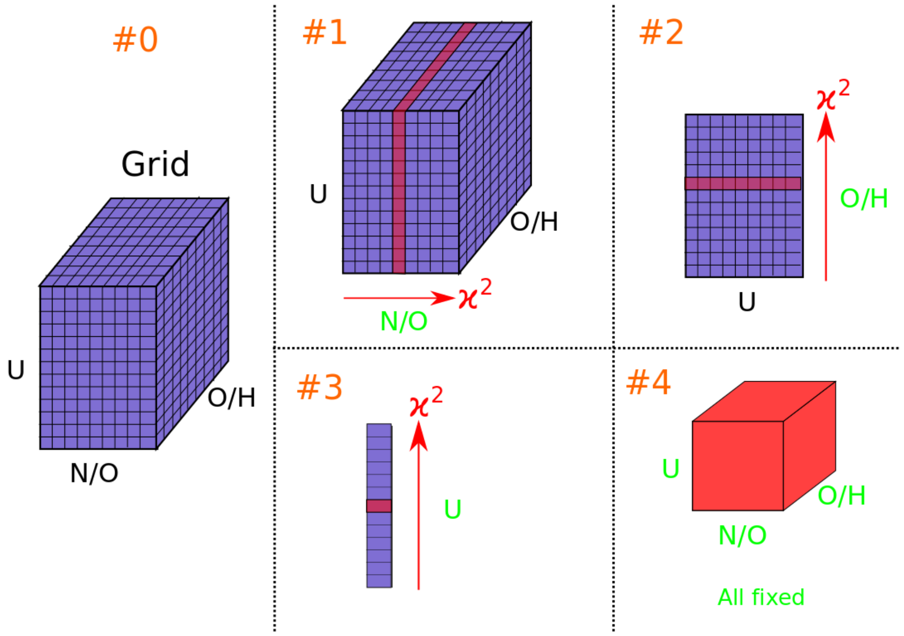

Figure 2.4: Schematic representation of the HCm code procedure. The sequence of the steps are presented in orange. The values that are fixed in each step are indicated with green color.

The code takes as input for each galaxy the emission lines ratios $[OII]\,\lambda3727$, $[NeIII]\,\lambda3868$, $[OIII]\,\lambda4363$, $[OIII]\,\lambda5007$, $[NII]\,\lambda6584$ and $[SII]\,\lambda\lambda6717, 6731$, all of them relative to the Balmer line H_β and corrected from dust extinction [Pérez-Montero et al. (2019)]. In a first step, the program searches for the values of N/O that best reproduce the emission line ratios provided, based on a χ^2-methodology. Then, the grids are reduced to those best of N/O (varying $12+\log_{10}(O/H)$ and $\log_{10}(U)$) and it searches for the best values of O/H and, finally, for the ionization parameter U [Pérez-Montero (2014)]. This procedure can be followed in Figure 2.4.

There are several advantages in using the HCm code. While the program takes six emission lines as input, it also works for a smaller subset (notice that the spectral information in the Palomar Survey provides three out the six inputs required and four just for only 19 galaxies). In addition, the code can be used for all the galaxies in the final sample with the only difference of setting previously the proper SED. And, finally, no relation between N/O and O/H is assumed in the code, so both calculations are independent.

3. Derivation of chemical abundances and ionization parameters

This chapter contains the main results of the chemical abundances and ionization parameters obtained for star-forming galaxies and AGN, analyzing the possible correlations among these parameters and comparing the different spectral types.

3.1 Emission line ratios and reddening correction

In order to use the HCm code, the emission line ratios used as input must be corrected from reddening. For the missing emission lines, namely $[OII]\,\lambda 3727$, $[NeIII]\,\lambda 3868$ and, in many cases, $[OIII]\,\lambda 4363$, the value of the flux and its error is set to 0, since this is the codification for the program to recognize these emission lines as not measured.

In spite of the fact that Ho et al. [1997a] presented some of the emission line ratios corrected from reddening following the Cardelli's extinction curve [1989], a new correction from the emission line ratios is applied. This new correction is motivated upon three reasons. Firstly, Ho et al. did not present the reddening correction for all the emission lines and it is necessary to correct some lines such as $[OIII]\,\lambda 4363$ that are needed by the code. Secondly, the extinction correction depends on the spectral classification of each galaxy, that is slightly different in this study because of the use of Kewley's criteria (notice that Ho et al. used Veilleux and Osterbrock's criteria [1987]). And, thirdly, the extinction magnitude A_V and the reddening values provided by Ho et al. show discrepancies which are important (the relative difference between our correction and Ho's correction can be up to 20%) for galaxies extremely affected by reddening as it is the case for IC 10.

Since the reddening is expressed as Equation (1.10), three values must be determined: the parameter $c\,(H_\beta)$ which depends on each galaxy, the value of the extinction curve at the wavelength λ and the value of the extinction curve at $\lambda = 4861$Å (the wavelength of H_β). The last two values are determined by using the extinction curve from Howarth [1983], shown in Equation (1.11), and assuming the standard value $R_V = 3.1$.

To determine the value of $c\,(H_\beta)$, the theoretical value of the ratio $I\,(H_\alpha)\,/I\,(H_\beta)$ is used. Assuming an electronic temperature $T_e \sim 10^4$ and an electronic density $n_e \sim 10^3\ cm^{-3}$, which are the typical values for both star-forming regions and NLR (see section 1.2 for more details), the expected value of this emission line ratio is, for case B recombination, 2.86 for star-forming galaxies and 3.1 for AGN [Osterbrock and Ferland (2006); Ho et al. (1997a)]. Since the Balmer lines H_α and H_β verify $\lambda_{H_\alpha} > \lambda_{H_\beta}$, the ratio $I\left(H_\alpha\right)/I\left(H_\beta\right)$ must increase due to the reddening. If a star-forming galaxy or an AGN shows an observed ratio below the theoretical value, then a value of $c\left(H_\beta\right) = 0$ is assumed. Otherwise, the value of $c\left(H_\beta\right)$ is calculated by using Equation (1.10) as:

$$c\left(H_\beta\right) = \frac{\log_{10}\left[\frac{\left(I(H_\alpha)/I(H_\beta)\right)_{Theo}}{\left(I(H_\alpha)/I(H_\beta)\right)_{Obs}}\right]}{\frac{f(H_\alpha)}{f(H_\beta)} - 1} \tag{3.1}$$

Name	$\boldsymbol{c\left(H_\beta\right)}$	$\frac{I([OII])}{I(H_\beta)}$	$\frac{I([NeIII])}{I(H_\beta)}$	$\frac{I([OIII]4)}{I(H_\beta)}$	$\frac{I([OIII]5)}{I(H_\beta)}$	$\frac{I([NII])}{I(H_\beta)}$	$\frac{I([SII])}{I(H_\beta)}$	**Class**
IC 10	2.00 ± 0.27	0.00 ± 0.00	0.00 ± 0.00	0.00 ± 0.00	3.71 ± 1.05	0.11 ± 0.04	0.15 ± 0.05	SFG
IC 1727	0.72 ± 0.27	0.00 ± 0.00	0.00 ± 0.00	0.00 ± 0.00	2.23 ± 0.63	2.87 ± 0.99	3.26 ± 1.05	L2
IC 2574	0.90 ± 0.27	0.00 ± 0.00	0.00 ± 0.00	0.00 ± 0.00	0.21 ± 0.06	0.20 ± 0.07	0.68 ± 0.22	SFG
NGC 63	0.98 ± 0.27	0.00 ± 0.00	0.00 ± 0.00	0.02 ± 0.01	0.038 ± 0.11	1.39 ± 0.48	0.87 ± 0.28	COM
⋮	⋮	⋮	⋮	⋮	⋮	⋮	⋮	⋮
UGC 3714	0.69 ± 0.27	0.00 ± 0.00	0.00 ± 0.00	0.00 ± 0.00	0.31 ± 0.09	1.31 ± 0.46	0.94 ± 0.30	SFG
UGC 3828	0.76 ± 0.27	0.00 ± 0.00	0.00 ± 0.00	0.00 ± 0.00	0.28 ± 0.08	1.11 ± 0.39	0.55 ± 0.18	SFG
UGC 4028	0.51 ± 0.27	0.00 ± 0.00	0.00 ± 0.00	0.00 ± 0.00	0.52 ± 0.15	1.34 ± 0.47	1.06 ± 0.34	COM
UGC 6484	0.04 ± 0.27	0.00 ± 0.00	0.00 ± 0.00	0.00 ± 0.00	0.41 ± 0.12	1.52 ± 0.53	0.97 ± 0.32	COM

Table 3.1: Values of $c\left(H_\beta\right)$, the emission line ratios (corrected from reddening) required for the HCm code and the spectral classification. Acronyms: SFG (star-forming galaxy), S2 (Seyfert 2), L2 (LINER) and COM (composite galaxies). An online version of this table with the complete set of parameters for the whole sample can be downloaded (in FITS format) at `https://cloud.iaa.csic.es/public.php?service=files&t=2a1e55eb8f3cd723fd82f21dfab5a995`.

Once $c\left(H_\beta\right)$ is calculated for each galaxy, then the emission line ratios required for HCm code (see subsection 2.4.2) are corrected from reddening following Equation (1.10). This information is provided in Table 3.1.

3.2 Previous considerations on the HCm code

3.2.1 Filtering the results

In order to retrieve reliable results, a criterion on the error of the chemical abundances and ionization parameter is established. Before explaining the criterion, the different sources of error and their corresponding propagation must be considered.

First of all, there are uncertainties in the flux of the emission line ratios that are introduced as input to the HCm code. These uncertainties can be decomposed onto two contributions: 1) the uncertainty in the measurement of the emission lines from the spectrum; and, 2) the uncertainty in the determination of the extinction parameter $c\left(H_{\beta}\right)$ coming from the reddening correction.

The HCm code takes into account two errors that combines in a quadratic sum to provide the final error in the estimation of each parameter [Pérez-Montero et al. (2019)]. The first error is that obtained on the χ^2-methodology used to select the optimal values for each parameter [Pérez-Montero (2014)]. The second error is calculated by a Monte Carlo simulation, where the outputs (chemical abundances and ionization parameter) are calculated for emission line ratios whose values are randomly taken in the intervals defined by the uncertainties in the inputs [Pérez-Montero et al. (2019)]. For our study, a total number of 50 iterations in the Monte Carlo simulations are made for each galaxy.

Considering the different sources of error and the step used to define the grids for the models (see subsection 2.4.2 for more details), only those results whose error is below $3\sigma_{step}$ (being σ_{step} the step in the grid for each parameter) are considered as reliable results and, therefore, analyzed in this study. In other words, the errors must verify:

$$\sigma_{O/H} \leq 0.3 \text{ dex} \quad ; \quad \sigma_{N/O} \leq 0.375 \text{ dex} \quad ; \quad \sigma_{U} \leq 0.75 \text{ dex} \tag{3.2}$$

3.2.2 Choice of α_{OX} in AGN

In the case of star-forming galaxies, only one SED can be selected in the HCm code. However, for AGN there are two options for the SED depending on the value of $\alpha_{OX} = -0.8$ or -1.2. The value of this parameter, which is the index of the power law used to model the transition between the X-ray and ultraviolet range, has been studied for many years and it is still under debate. For instance, a study of quasars at low ($z < 1$), intermediate ($1 < z < 2$) and high ($z > 2$) redshifts [Miller et al. (2010)] shows a large range of α_{OX}, $[-1.6, -0.8]$. The study of Seyferts in the SDSS presented by Liu et al. [2018] agrees with the interval $[-1.6, -0.8]$. In the case of LINERs, the study presented by Gliozzi et al. [2008] shows that this range is slightly changed to $[-1.5, -0.7]$.

Additionally, it is widely accepted that α_{OX} depends on the luminosity of the AGN [Gliozzi et al. (2008); Miller et al. (2010); Vagnetti et al. (2013); Liu et al. (2018)], hence the value of this parameter can vary from one galaxy to another even if they belong to the same spectral class. Moreover, the variability observed in some AGN can also produce changes in α_{OX} [Vagnetti et al. (2013)].

Since the HCm code only accepts two values for α_{OX}, -0.8 and -1.2, both were studied in order to determine which one is the best for the study of chemical abundances in AGN, distinguishing between Seyferts and LINERs. A Kolmogorov-Smirnov test [1933] (hereafter KS-test) for each distribution was performed in other to quantify the changes. Table 3.2 shows the resulting values.

- The results obtained for Seyferts are shown in Figure 3.1. For Seyferts, the change of α_{OX} does not have any particular effect in the chemical abundance ratio $\log_{10}(N/O)$ since both results are compatible within the errors and the p-value is 0.66 (see Figure 3.1 (b)). In the case of the chemical abundance $12 + \log_{10}(O/H)$, the histograms (Figure 3.1 (a)) show a saturation at ≈ 8.9 when $\alpha_{OX} = -1.2$, although the p-value does not indicate different distributions (p-value = 0.21). The

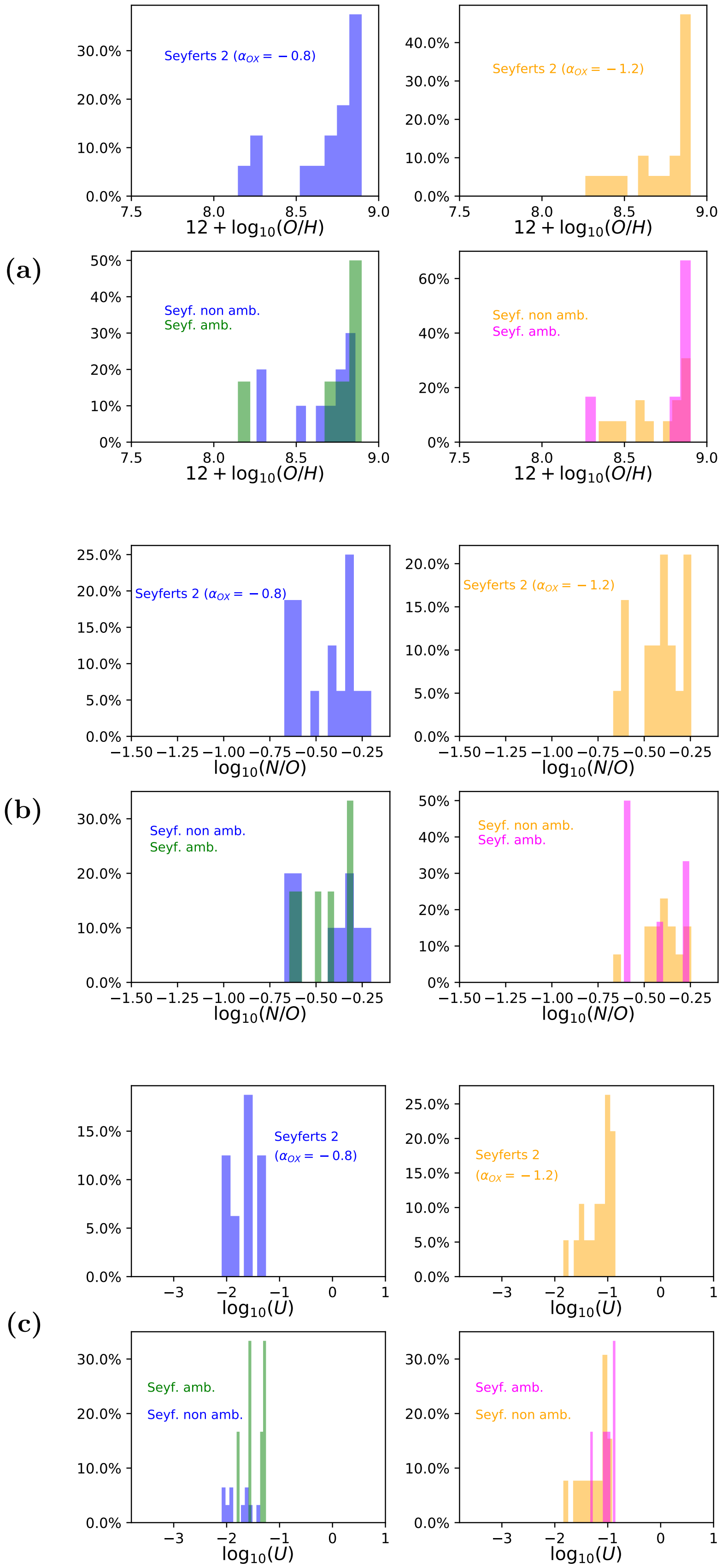

Figure 3.1: Histograms of the chemical abundance (a), the chemical abundance ratio (b) and the ionization parameter (c). The left (right) column shows the results for $\alpha_{OX} = -0.8$ ($\alpha_{OX} = -1.2$). The first row shows the global statistics for each spectral class while in the second one the ambiguous (amb.) and non ambiguous (non amb.) are separated.

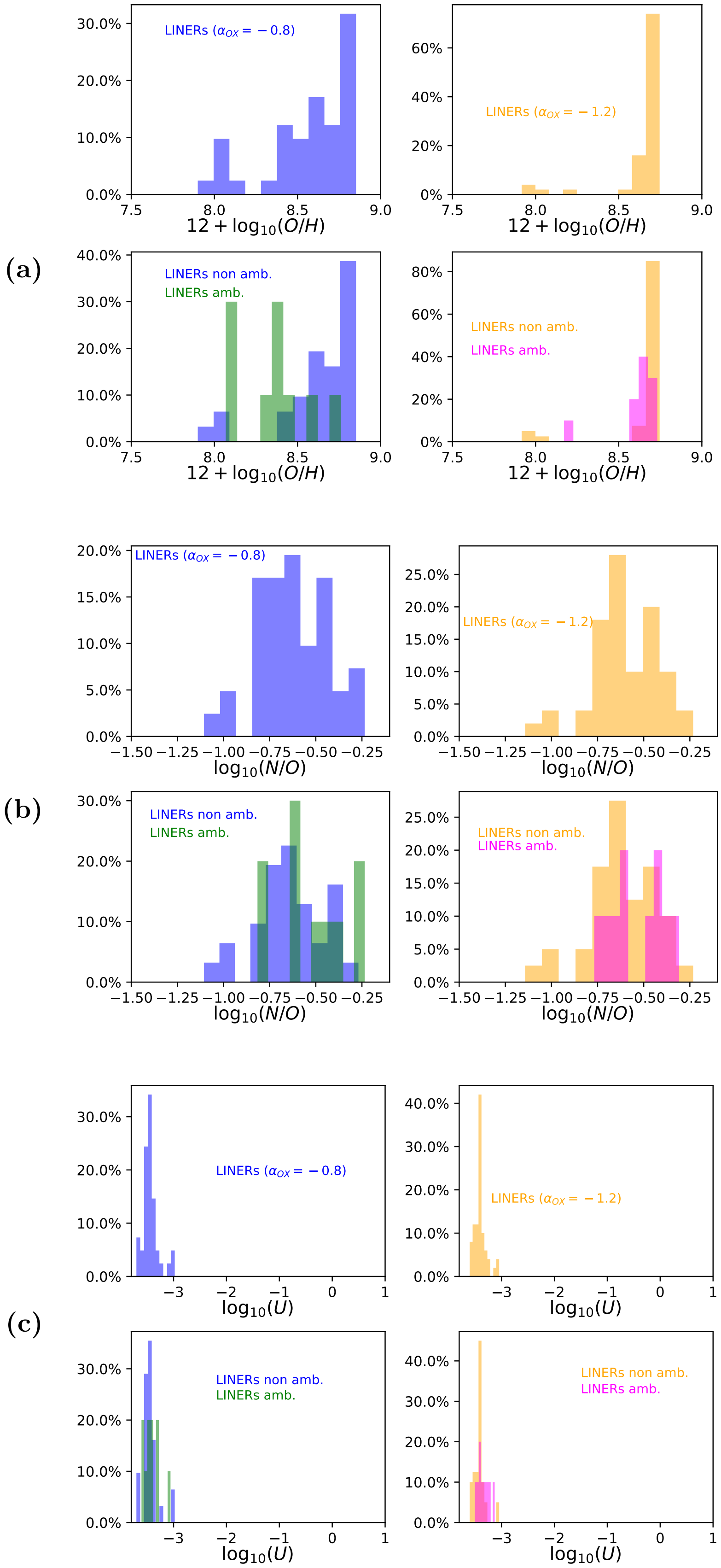

Figure 3.2: Same as Figure 3.1 but for LINERs.

ionization parameter U shows a slightly increase from $\alpha_{OX} = -0.8$ to $\alpha_{OX} = -1.2$ (see Figure 3.1 (c)), showing that both distributions are different (p-value = 0.00018). This last result is in good agreement with the previous study by Pérez-Montero et al. [2019].

- The results obtained for LINERs are shown in Figure 3.2. As for Seyferts 2, no significant changes are found in the chemical abundance ratio $\log_{10}(N/O)$ (the p-value in LINERs increases to 0.92). The saturation observed for Seyferts in $12 + \log_{10}(O/H)$ is clearer in the case of LINERs, but the saturation value is lower ($12 + \log_{10}(O/H) \approx 8.75$). In fact, both distributions are totally different (p-value = 0.00088). In contrast, the ionization parameter for LINERs does not change with α_{OX} as it is the case in Seyferts (see Figure 3.2 (c)), although the KS-test provides a low p-value (0.012).

Parameters	**Seyferts 2**	**LINERs**
$\mathbf{12 + \log_{10}(O/H)}$	0.21	0.00088
$\mathbf{\log_{10}(N/O)}$	0.66	0.92
$\mathbf{\log_{10}(U)}$	0.00018	0.012

Table 3.2: P-values of the KS-test comparing the distributions obtained with $\alpha_{OX} = -0.8$ and $\alpha_{OX} = -1.2$.

On the one hand, according to the previous study of the Palomar Survey [Ho et al. (2003)], LINERs present ionization parameters $\log_{10}(U) = -3.0 \pm 1.0$, which are in good agreement with the results obtained for both values of α_{OX}. However, Seyferts present values of $\log_{10}(U) = -2.0 \pm 0.5$, which are in better agreement with the results obtained for $\alpha_{OX} = -0.8$ than for the other value. On the other hand, the chemical abundance $12 + \log_{10}(O/H)$ shows a saturation for both types of AGN when $\alpha_{OX} = -1.2$ is chosen. For these reasons, the value of $\alpha_{OX} = -0.8$ is finally selected for the SED in AGN in our study.

3.2.3 Treatment of the galaxy NGC 2541

The galaxy NGC 2541 required a specific study as a consequence of its classification in the diagnostic diagrams (located in a different region on each one). Consequently, there is no criterion to select its SED. Both SEDs will be considered for this galaxy in order to avoid any bias.

3.3 Chemical abundances in the sample

3.3.1 Galaxies excluded

As explained in subsection 3.2.1, only galaxies verifying Equation (3.2) are studied. Consequently, the sample of 234 galaxies is reduced to 185 (79.1%) if composite and unknown galaxies are treated as SFG, or to 183 (77.8%) if composite and unknown galaxies are treated as AGN. The breakdown of these numbers is as follows:

- A total of 20 star-forming galaxies are excluded. From these 20 galaxies, 3 of them were initially classified as ambiguous galaxies.
- A total of 7 Seyferts are excluded, of which only one was initially classified as ambiguous galaxy.
- A total of 15 LINERs are excluded, of which 4 were initially classified as ambiguous galaxies.
- If composite galaxies are treated as SFG, 7 of these galaxies are excluded in the study. On the other hand, if they are treated as AGN, then the excluded galaxies increase to 10.
- In the case of the unknown galaxy (NGC 2541), either using a star-forming or an AGN SED, this galaxy always remains in the sample of galaxies to be studied.

Focusing on the reason for exclusion, when composite and unknown galaxies are treated as SFG, 14 galaxies are omitted due to non-reliable determination of $12 + \log_{10}(O/H)$, 12 of $\log_{10}(N/O)$ and 23 of both. When composite and unknown galaxies are treated as AGN, those numbers change to 14, 17 and 21, respectively. In both cases, the determination of the ionization parameter is always below the limit shown in Equation (3.2), i.e., is always a reliable determination. A summary of all these numbers is presented in Table 3.3.

Spectral type	**Excluded**	**Percentage (%)***
Star-forming	20	18.7
Seyfert 2	7	30.4
LINER	15	26.8
Composite	7 (10)	14.9 (21.3)
Unknown	– (–)	0.0 (0.0)
Sum	49 (52)	20.9 (22.2)

Reason	**Excluded**	**Percentage (%)****
Non-reliable O/H	14 (14)	6.0 (6.0)
Non-reliable N/O	12 (17)	5.1 (7.3)
Both	23 (21)	9.8 (8.9)
Sum	49 (52)	20.9 (22.2)

Table 3.3: Statistics of the excluded galaxies. Within parenthesis are shown the results when composite and unknown galaxies are treated as AGN. *Percentage relative to each spectral type. **Percentage relative to the whole sample.

3.3.2 Results for star-forming galaxies

The results obtained for the relative abundance of oxygen show that the median value is around $12 + \log(O/H) = 8.71 \pm 0.16$, with a minimum value of 7.85 and a maximum of 8.80. This range is in agreement with previous studies based on the T_e-method [Vila-Costas and Edmunds (1993); Andrews and Martini (2013)], calibrations based on strong emission lines [Pérez-Montero et al. (2013); Dors et al. (2015)] or on photoionization models [Pérez-Montero and Contini (2009); Vincenzo et al. (2016)] (see Table 3.4 for more details). It must be noticed that some of these studies show values above $12 + \log_{10}(O/H) > 9.0$ [Vila-Costas and Edmunds (1993); Andrews and Martini (2013); Pérez-Montero et al. (2013)].

The results obtained for the chemical abundance ratio $\log_{10}(N/O)$ show a median value around -0.73 ± 0.22, with a minimum value of -1.41 and a maximum of -0.38. These values are also in agreement with previous studies such as Vincenzo et al. [2016] or Pérez-Montero et al. [2009; 2013; 2014] (see Table 3.5).

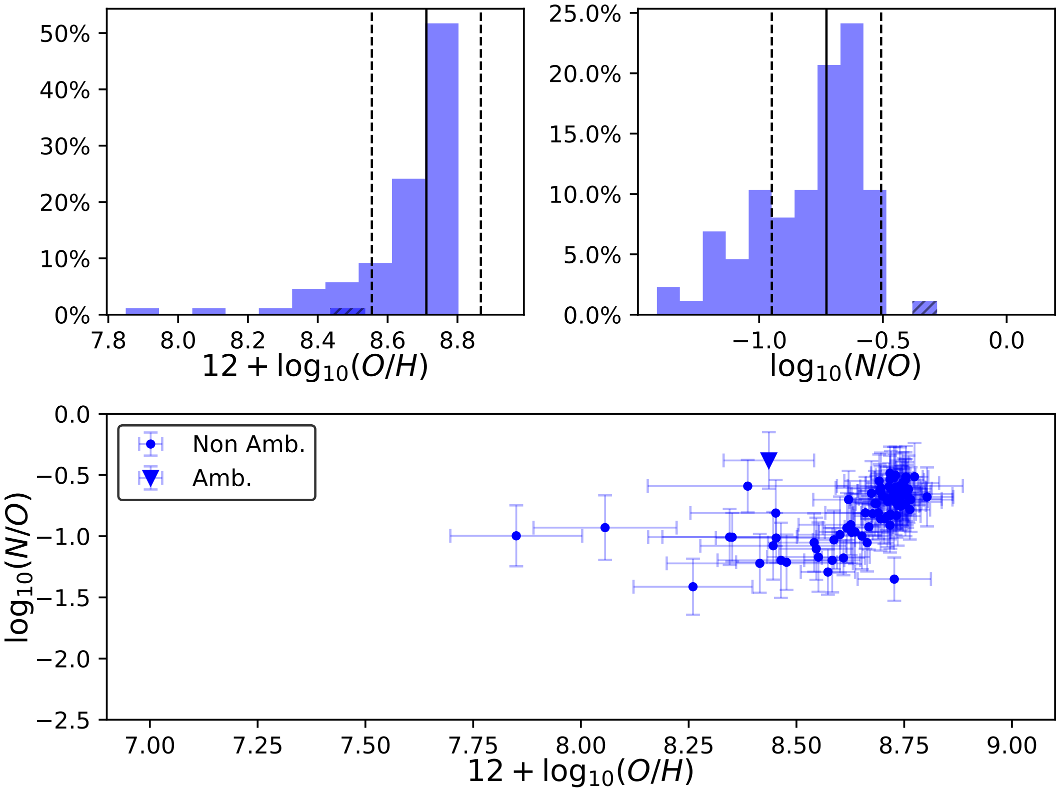

Figure 3.3: Chemical abundances obtained for star-forming galaxies. The top left plot shows the histogram of the chemical abundance $12 + \log_{10}(O/H)$. The top right plot shows the histogram of $\log_{10}(N/O)$. For both histograms, the solid lines represent the median values and the dashed lines the standard deviations. The dashed-filled histograms are associated to ambiguous galaxies. The bottom plot shows the relation between the chemical abundance ratio $\log_{10}(N/O)$ and $12 + \log_{10}(O/H)$.

The diagram $\log_{10}(N/O)$ vs $12 + \log_{10}(O/H)$ (see Figure 3.3, bottom plot) reflects the behavior already reported by Vila-Costas and Edmunds [1993] or Andrews and Martini [2013]. For lower values of O/H ($12 + \log_{10}(O/H) < 8.6$), the abundance ratio N/O remains constant at $\log_{10}(N/O) \approx -1.5$, however the low statistics of low metallicity galaxies does not allow to determine this tendency. This result, already reported [Vila-Costas and Edmunds (1993); Andrews and Martini (2013)], might be interpreted as galaxies where its nitrogen has a primary origin (see section 1.4 for more details) and the variation in O/H is probably a consequence of inflows of gas to the center acting as fuel for the star formation. For higher metallicities ($12 + \log_{10}(O/H) > 8.6$), the ratio N/O increases proportionally with O/H. This result can be seen as the secondary origin of the nitrogen, i.e., the elements are already present in the gas during the star formation [Vila-Costas and Edmunds (1993); Andrews and Martini (2013)].

Range	Method	Study
[7.5, 9.3]	T_e-method	Vila-Costas and Edmunds (1993)
[7.8, 8.7]	T_e-method	Andrews and Martini (2013)
[7.2, 9.5]	Optical calibrators	Pérez-Montero et al. (2013)
[8.0, 8.7]	Optical calibrators	Dors et al. (2015)
[7.2, 8.7]	Photoionization model	Pérez-Montero and Contini (2009)
[8.1, 8.9]	Photoionization model	Vincenzo et al. (2016)
[7.9, 8.8]	Photoionization model	Our study

Table 3.4: Compilation of the chemical abundance $12 + \log_{10}(O/H)$ in star-forming galaxies obtained in different studies.

Range	Method	Study
[-2, 0]	T_e-method	Pérez-Montero (2014)
[-2.3, 0.2]	Optical calibrators	Pérez-Montero et al. (2013)
[-2.5, -0.1]	Photoionization model	Pérez-Montero and Contini (2009)
[-2.0,-0.2]	Photoionization model	Pérez-Montero (2014)
[-1.6, 0.1]	Photoionization model	Vincenzo et al. (2016)
[-1.4, -0.38]	Photoionization model	Our study

Table 3.5: Compilation of the chemical abundance $\log_{10}(N/O)$ in star-forming galaxies obtained in different studies.

While some studies show this change in the behavior at $12 + \log_{10}(O/H) \approx 8.5$ [Vila-Costas and Edmunds (1993); Andrews and Martini (2013)] and others at $12+\log_{10}(O/H) \approx 8.4$ [Vincenzo et al. (2016)], in our study this change has been detected at $12 + \log_{10}(O/H) \approx 8.6$. Considering the uncertainties in the determination of the chemical abundances, all these results are consistent among each other.

3.3.3 Results for Seyferts 2

The results obtained for the relative abundance of oxygen in Seyferts 2 show a median value around $12 + \log_{10}(O/H) = 8.78 \pm 0.23$ (near the solar value shown in Equation (1.38)), with a minimum value of 8.15 and a maximum of 9.00. This range is in good agreement with previous determinations based on optical strong emission lines calibrations [Storchi-Bergmann et al. (1998); Dors et al. (2015); Castro et al. (2017); Dors et al. (2019)], but also with the results obtained by using other photoionization models such as NebulaBayes [Thomas et al. (2019)] (see Table 3.6). However, it must be noticed that only three galaxies (NGC 3982, NGC 4138 and NGC 4477) show values above $12+\log_{10}(O/H) > 9.0$ (considering the uncertainties in the derivation of the chemical abundance), in spite of the fact that some of the previous studies [Storchi-Bergmann et al. (1998); Dors et al. (2015, 2019); Thomas et al. (2019)] report values above that limit. Nevertheless, the range $[8.1, 9.0]$ is in good agreement with the previous determination presented by Dors et al. [2015] of 12 Seyferts from the Palomar Survey.

The chemical abundance ratio $\log_{10}(N/O)$ presents a median value of -0.43 ± 0.15, with a minimum value of -0.67 and a maximum of -0.20. This range is in good agreement with the range $[-0.8, -0.3]$ presented by Carvalho et al. [2020].

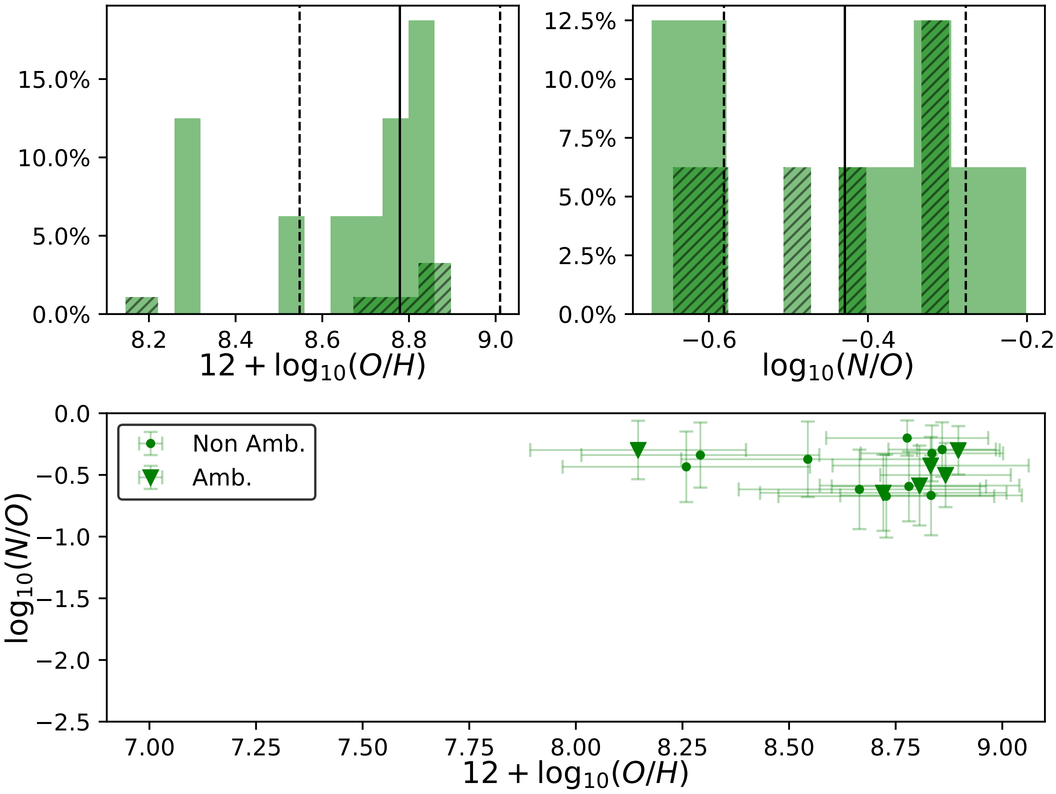

Figure 3.4: Chemical abundances obtained for Seyferts 2. The top left plot shows the histogram of the chemical abundance $12 + \log_{10}(O/H)$. The top right plot shows the histogram of $\log_{10}(N/O)$. For both histograms, the solid lines represent the median values and the dashed lines the standard deviations. The dashed-filled histograms are associated to ambiguous galaxies. The bottom plot shows the relation between the chemical abundance ratio $\log_{10}(N/O)$ and $12 + \log_{10}(O/H)$..

Range	Method	Study
[7.1, 9.5]	T_e-method	Dors et al. (2015)
[7.4, 9.2]	T_e-method	Dors et al. (2019)
[8.9, 9.3]	Optical calibrators	Storchi-Bergmann et al. (1998)
[8.4, 9.4]	Optical calibrators	Dors et al. (2015)
[8.2, 9.0]	Optical calibrators	Castro et al. (2017)
[8.4, 9.2]	Optical calibrators	Dors et al. (2019)
[8.1, 9.1]	Photoionization model	Dors et al. (2019)
[7.9, 9.4]	Photoionization model	Thomas et al. (2019)
[8.2, 9.0]	Photoionization model	Our study

Table 3.6: Compilation of the chemical abundance $12 + \log_{10}(O/H)$ in Seyferts 2 obtained in different studies.

It must be noticed that the histograms in Figure 3.4 reveal that two populations of Seyferts can be distinguished by their chemical abundances. This result is emphasized when only the histogram $\log_{10}(N/O)$ is considered. However, due to the small number of objects (16 Seyferts), this result needs to be explored with a larger sample. The solar and supra-solar values of the chemical abundance of oxygen can be explained by two models (that are not incompatible): 1) dust destruction in the NLR causing the release of metals into the ISM [Nagao et al. (2006); Matsuoka et al. (2009)]; and, 2) AGN-driven outflows that are originated in the central metal-rich region [Maiolino and Mannucci (2019)].

Finally, the N/O vs O/H plot (see Figure 3.4, bottom panel) does not show any particular trend. Again, the small size of the Seyferts 2 sample requires a new revisiting of these result in larger samples due to its implication: as discussed in subsection 1.4.2, the calibrations based on strong optical emission lines assumed a relation between O/H and N/O which is determined by analyzing star-forming galaxies. However, our results suggest that the trend in star-forming galaxies cannot be extrapolated to Seyferts 2.

3.3.4 Results for LINERs

The NLR in LINERs presents a median oxygen abundance of $12 + \log_{10}(O/H) = 8.63 \pm 0.26$, with a minimum value of 7.90 and a maximum of 8.85. This range is consistent with the study presented by Storchi-Bergmann et al. [1998], although they only analyzed 4 LINERs, obtaining a shorter range of values $[8.64, 9.03]$.

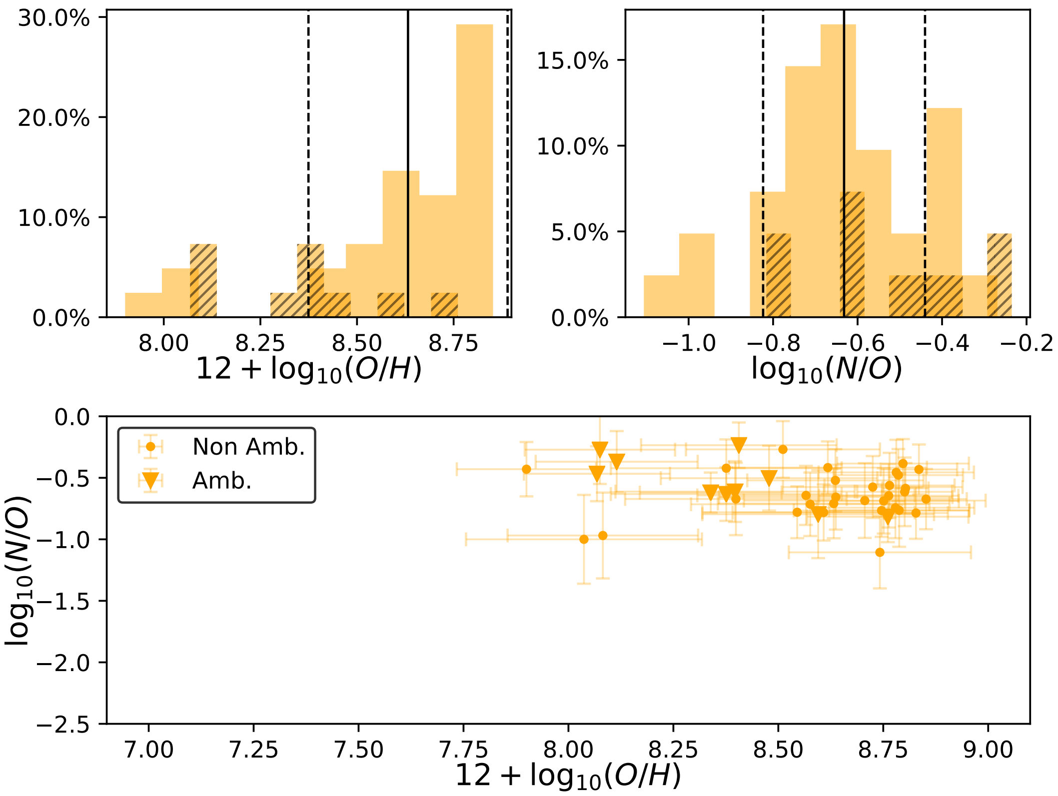

Figure 3.5: Chemical abundances obtained for LINERs. The top left plot shows the histogram of the chemical abundance $12 + \log_{10}(O/H)$. The top right plot shows the histogram of $\log_{10}(N/O)$. For both histograms, the solid lines represent the median values and the dashed lines the standard deviations. The dashed-filled histograms are associated to ambiguous galaxies. The bottom plot shows the relation between the chemical abundance ratio $\log_{10}(N/O)$ and $12 + \log_{10}(O/H)$.

The chemical abundance ratio $\log_{10}(N/O)$ presents a median value of -0.63 ± 0.19, with a minimum value of -1.11 and a maximum of -0.24.

The histogram of the chemical abundance O/H (see Figure 3.5, top left plot), reveals a small population of LINERs (6 galaxies, which represent 15% of the sample of these AGN) with low metallicities ($12 + \log_{10}(O/H) < 8.2$). However, most LINERs present an oxygen abundance in the range [8.3, 8.9], which is in good agreement with the results presented by Storchi-Bergmann [1998]. The histogram of the chemical abundance ratio $\log_{10}(N/O)$ shows a tail in the distribution (composed only by 3 galaxies, representing 7% of the sample), but there is no correlation between this tail in $\log_{10}(N/O)$ (composed by NGC 185, NGC 3226 and NGC 4278) and that observed in $12 + \log_{10}(O/H)$ (composed by NGC 410, NGC 3193, NGC 3226, NGC 4278, NGC 4321 and NGC 4429), i.e., the galaxies are different, with the exception of NGC 3226.

The N/O vs O/H diagram (see Figure 3.5, bottom panel) shows that there is no correlation between both values (as it is the case for Seyferts 2), which implies that the trend seen in star-forming galaxies (see subsection 3.3.2 for more details) cannot be used in LINERs.

3.3.5 Results for NGC 2541

The chemical abundances obtained for NGC 2541 are shown in Table 3.7. The value of $\log_{10}(N/O)$ is compatible under both models (star-formation or AGN) within the errors. However, this is not the case for $12 + \log_{10}(O/H)$, where for the AGN model a lower value is obtained.

SED	$\mathbf{12 + \log_{10}(O/H)}$	$\mathbf{\log_{10}(N/O)}$	$\mathbf{\log_{10}(U)}$
Star-forming	8.52 ± 0.09	-1.31 ± 0.18	-2.98 ± 0.08
AGN	7.87 ± 0.13	-1.23 ± 0.20	-3.17 ± 0.25

Table 3.7: Chemical abundances of NGC 2541.

3.3.6 Comparison between spectral types

The global results for the oxygen abundance $12 + \log_{10}(O/H)$ show that its upper limit is higher in AGN than in star-forming galaxies (see Figure 3.6). In both star-forming galaxies and AGN, there is a high percentage (> 30%) of galaxies with values close to the upper limits. This percentage increases to the 50% in the case of star-forming galaxies. This is in good agreement with the results obtained by Dors et al. [2015] for a sample of 12 Seyferts 2 and 33 star-forming galaxies from the Palomar Survey.

Analyzing the nitrogen to oxygen abundance ratio $\log_{10}(N/O)$, is slightly higher ($1\ \sigma$ higher) in AGN than in star-forming galaxies (see Figure 3.7 and Table 3.8).

To end with this comparison, the diagram *N/O vs O/H* is presented for all types of AGN. For Seyferts 2 and LINERs, no trend was found in this diagram. By representing together both results in Figure 3.8, it can be seen that Seyferts 2 present higher metallicities in their NLR than LINERs. However, this result should be confirmed with a larger sample of AGN, since in our study the Seyferts 2 sample is small (16 objects).

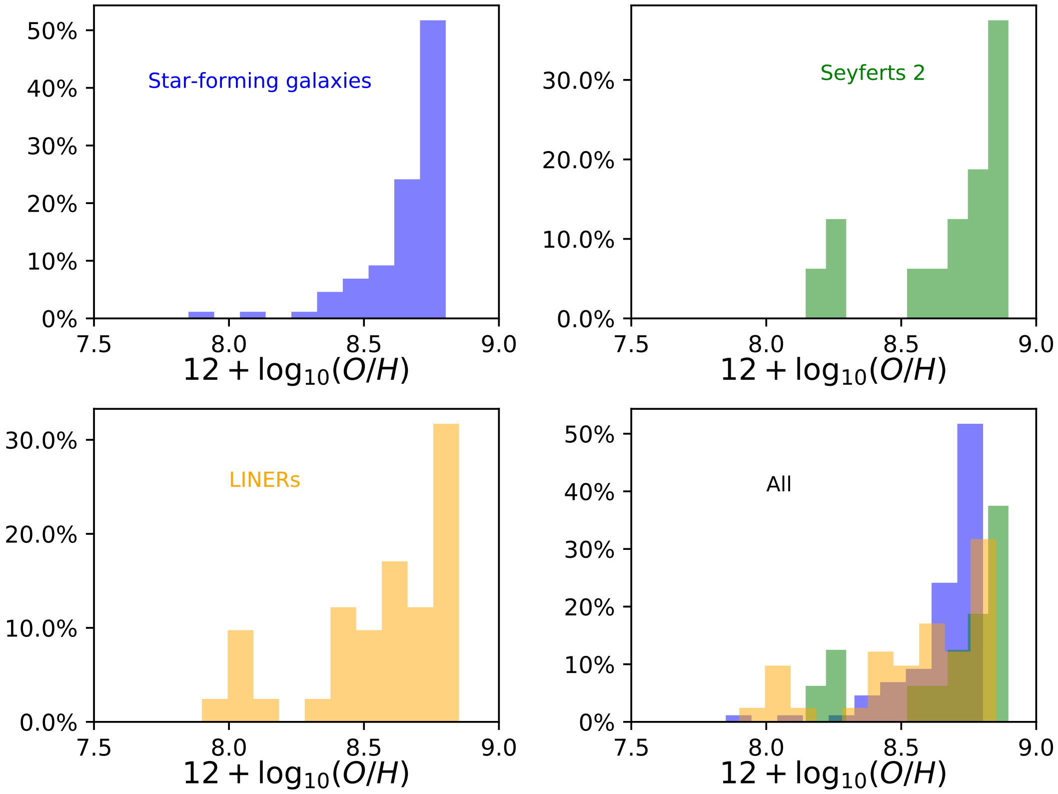

Figure 3.6: Distributions of the chemical abundance $12 + \log_{10}(O/H)$ for star-forming galaxies, Seyferts 2 and LINERs.

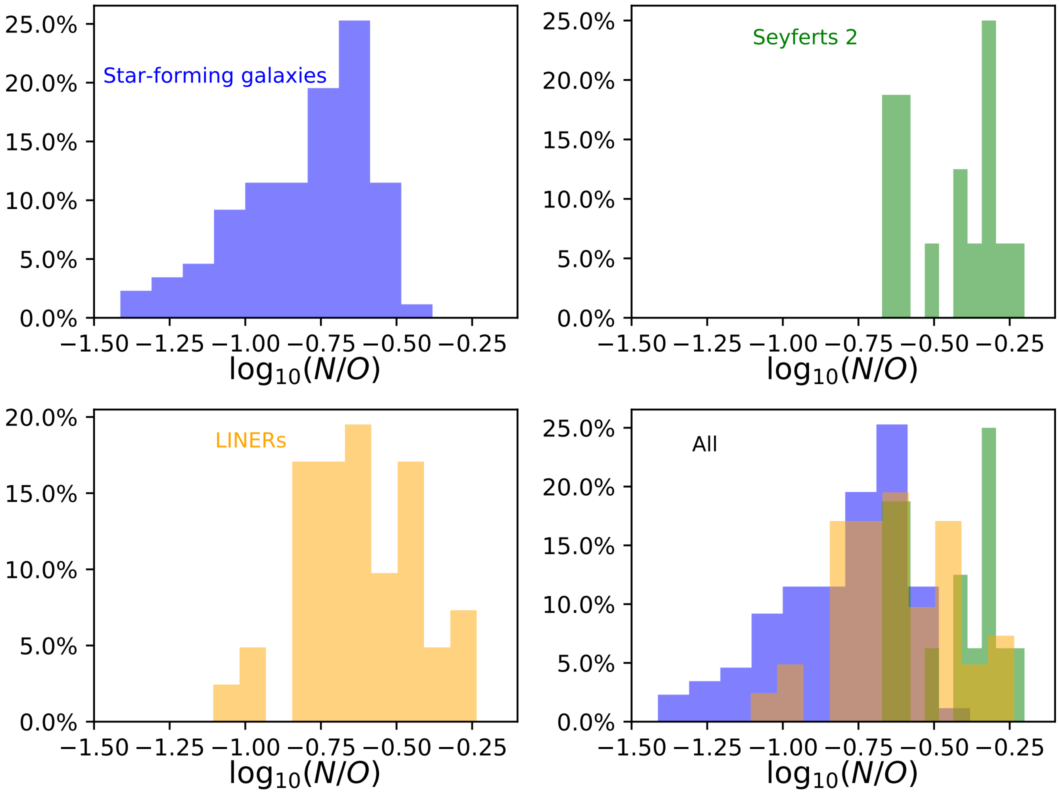

Figure 3.7: Same as Figure 3.6 but for $\log_{10}(N/O)$.

$12 + \log_{10}(O/H)$				
Type	**Number**	**Median**	**Std. Dev.**	**Range**
Star-forming	87	8.71	0.16	[7.85, 8.80]
Seyferts 2	16	8.78	0.23	[8.15, 8.90]
LINERs	41	8.63	0.26	[7.90, 8.85]

$\log_{10}(N/O)$				
Type	**Number**	**Median**	**Std. Dev.**	**Range**
Star-forming	87	-0.73	0.22	[-1.41, -0.38]
Seyferts 2	16	-0.43	0.15	[-0.67, -0.20]
LINERs	41	-0.63	0.19	[-1.11, -0.24]

Table 3.8: Statistics of the chemical abundances for each spectral type.

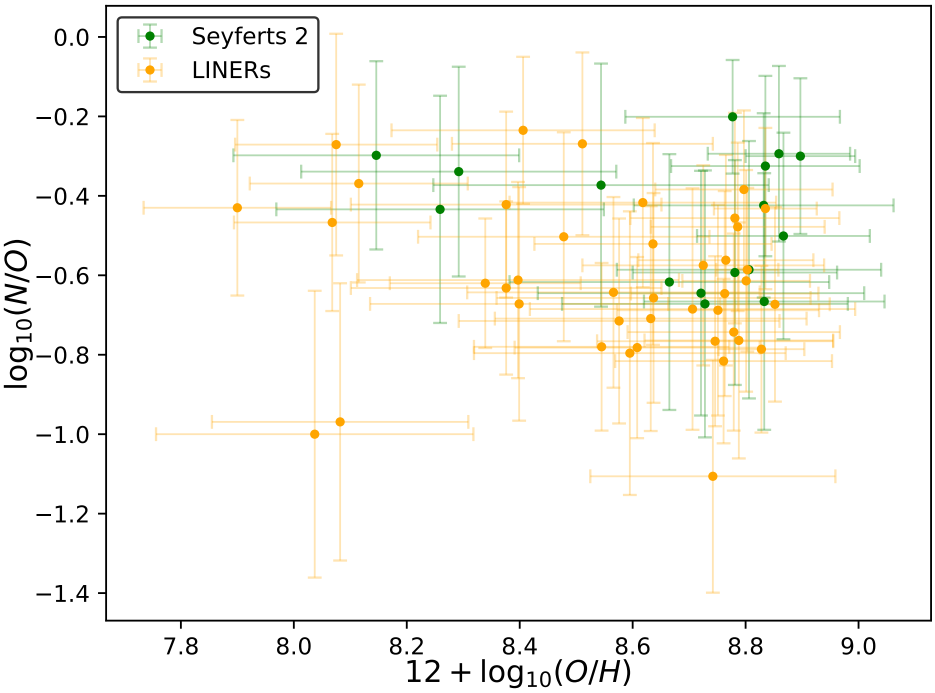

Figure 3.8: Diagram $\log_{10}(N/O)$ vs $12 + \log_{10}(O/H)$ for AGN.

3.4 Ionization parameter in the sample

In subsection 3.3.1 it is explained that the final sample is reduced to either 185 or 183 objects depending on the treatment of composite galaxies. Since the ionization parameter presents reliable results for all the composite galaxies, the sample does not change from that used in the study of chemical abundances.

3.4.1 Results for star-forming galaxies

The ionization parameter in star-forming galaxies presents a median value of $\log_{10}(U) - 3.21 \pm 0.17$, with a minimum value of -3.43 and a maximum of -2.45. This range of values is in good agreement with previous studies based on strong emission line calibrations such as the range $[-3.5, -2.5]$ by Dopita et al. [2000] and the range $[-3.3, -2.5]$ by Moustakas et al. [2010]. The upper limit ($\log_{10}(U) = -2.45$) in the ionization parameter, which is obtained for the galaxy IC 10, is practically the same as that found in the local Universe for young, massive super star clusters located in galaxies with intense star formation episodes [Smith et al. (2006)]. This upper limit suggests the existence of a mechanism (or mechanisms) that maintains the ionization below this limit, whereas this is still an open question [Yeh and Matzner (2012); Kewley et al. (2019)].

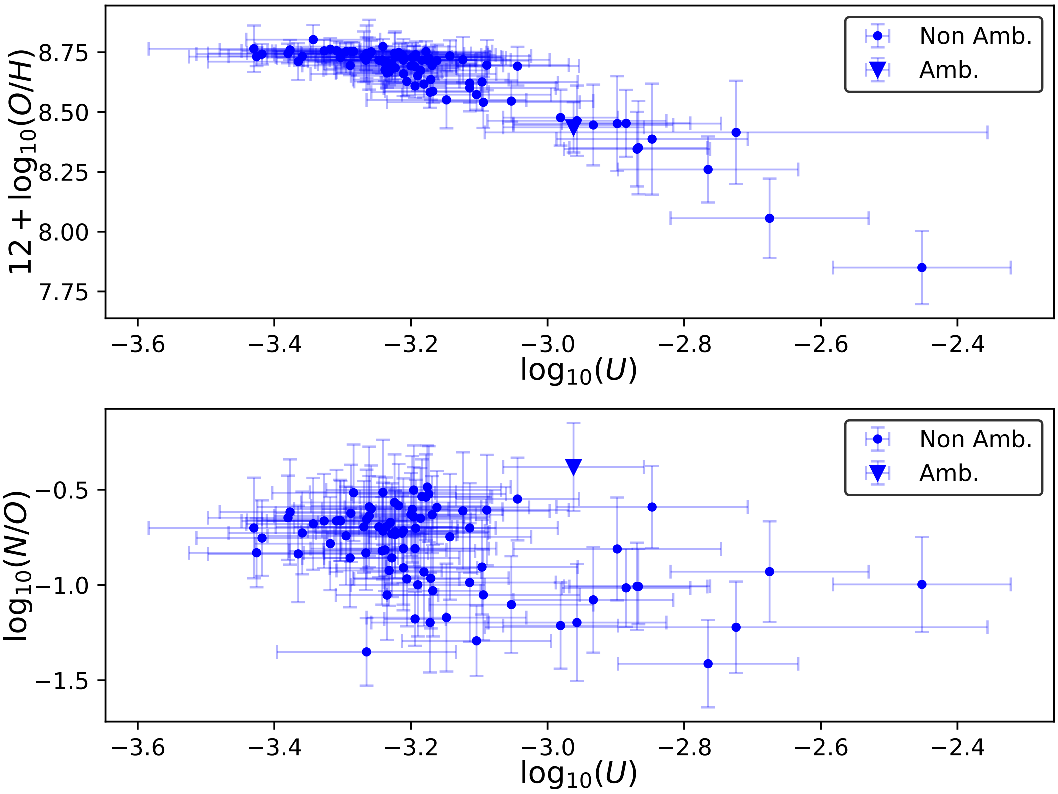

Figure 3.9: Variation of the chemical abundances $12+\log_{10}(O/H)$ and $\log_{10}(N/O)$ with the ionization parameter $\log_{10}(U)$ in star-forming galaxies.

The dependence of the chemical abundances with the ionization parameter is analyzed in Figure 3.9. There is a strong anti-correlation (the Pearson correlation coefficient is $r = -0.92$) between $12+\log(O/H)$ and $\log_{10}(U)$ (see the top panel): for higher values of the ionization, lower abundances are retrieved. This result was already reported by Pérez-Montero [2014], by using the T_e-method. In the case of the relative abundance of nitrogen to oxygen, there seems to be a bi-valuation due to the change in sign of the slope at $\log_{10}(U) \approx -3.30$. Using the relation between O/H and U, the corresponding abundance for this value of the ionization parameter is $12+\log_{10}(O/H) \approx 8.6$, which is the value at which $\log_{10}(N/O)$ scales with the oxygen abundance as discussed in subsection 3.3.2. Therefore, the upper branch can be interpreted as the values for star-forming galaxies whose nitrogen abundance has a secondary origin, while the lower branch is associated to galaxies whose nitrogen has a primary origin.

3.4.2 Results for Seyferts 2

The mean value of the ionization parameter in Seyferts 2 is $\log_{10}(U) = -1.64 \pm 0.26$, with a minimum value of -2.09 and a maximum of -1.26. These values are compatible with those presented by previous studies for Seyferts: Ferland and Netzer [1983] proposed $\log_{10}(U) = -2.0$ for Seyferts 1 and $\log_{10}(U) = -2.5$ for Seyferts 2, Ho et al. [1993; 2003] obtained $\log_{10}(U) = -2.5 \pm 0.5$, Almeida et al. [2006] found $\log_{10}(U) \approx -1.5$ for the Seyfert Mrk 78 and Kewley et al. [2006] obtained the range $[-2.5, -2.0]$.

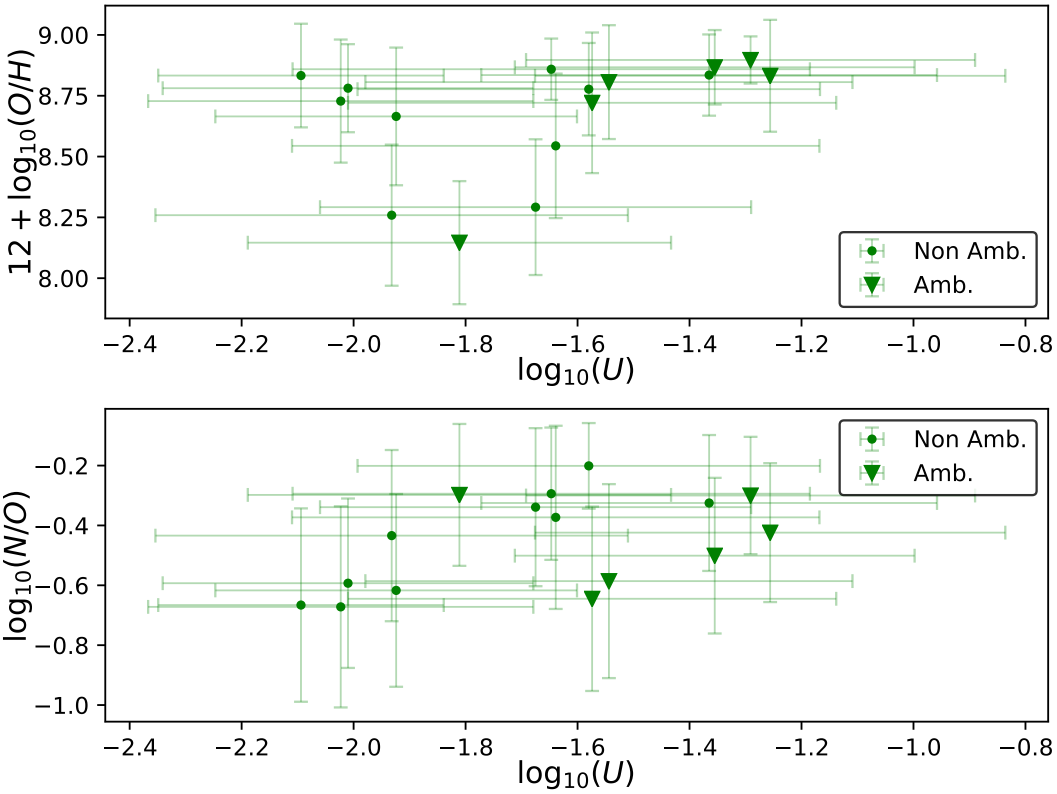

Figure 3.10: Variation of the chemical abundances $12+\log_{10}(O/H)$ and $\log_{10}(N/O)$ with the ionization parameter $\log_{10}(U)$ in Seyferts 2.

The plot of the chemical abundance $\log_{10}(N/O)$ with the ionization parameter shows that there is no correlation (the Pearson correlation coefficient has a value $r = 0.49$) between both values (see Figure 3.10, bottom panel). While the sample of Seyferts 2 is the smallest in this study (with only 16 galaxies), Carvalho et al. [2020] find a similar result with the analysis of a sample of 463 Seyferts 2. In addition to this, from our study it can be seen that the ionization parameter $\log_{10}(U)$ is not correlated with $12+\log_{10}(O/H)$ (see Figure 3.10, top panel). This last result needs to be contrasted with a larger sample of Seyferts 2 galaxies.

3.4.3 Results for LINERs

As discussed in sections 1.1 and 1.2, the ionization parameter of the NLR in LINERs should be lower than in Seyferts. Since the grid of models in the case of LINERs is limited to the range $[-4.0, -2.5]$ for the ionization parameter (see subsection 2.4.2 for more details), the previous statement is guaranteed in our results. The median value obtained for LINERs is $\log_{10}(U) = -3.46 \pm 0.15$, with a minimum value of -3.70 and a maximum of -2.97. These values are in good agreement not only with the theoretical $\log_{10}(U) \approx -3.5$ proposed by Ferland and Netzer [1983] or Halpern and Steiner [1983] (among many others), but also with the empirical fits from photoionization models [Binette (1985); Kewley et al. (2006)] with $\log_{10}(U) \approx -3.0$.

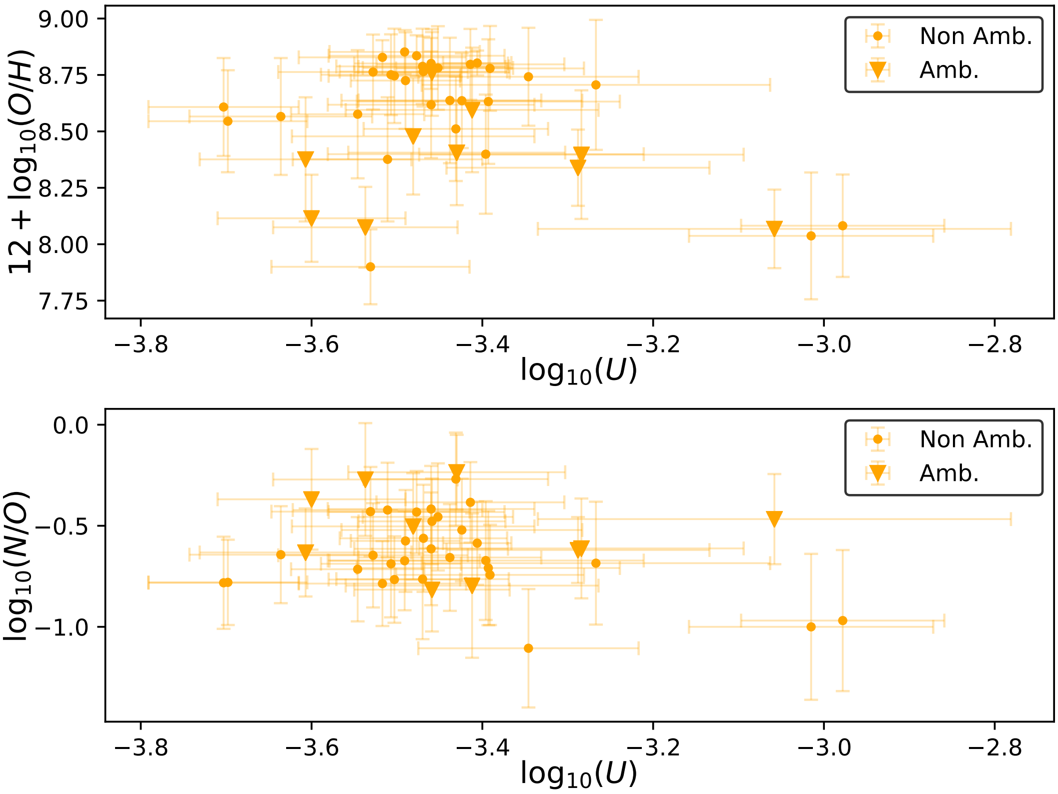

Figure 3.11: Same as Figure 3.10 but for LINERs.

Figure 3.11, where the chemical abundances are plotted against the ionization parameter, shows that there is no correlation between the abundances $12 + \log_{10}(O/H)$ or $\log_{10}(N/O)$ and the ionization parameter $\log_{10}(U)$ (the Pearson correlation coefficients are $r = -0.34$ and -0.26, respectively). This is the same result as what is obtained for Seyferts 2.

3.4.4 Results for NGC 2541

The values of the ionization parameter under both models, star forming and AGN SED, are shown in Table 3.7. The value of $\log_{10}(U) = -2.98 \pm 0.08$ obtained by using the star forming SED decreases to -3.17 ± 0.25 if the AGN model is considered. However, it should be noticed that, within the errors, both values are compatible.

3.4.5 Comparison between spectral types

As it is expected from theory, $\log_{10}(U)$ is the best parameter in our study for distinguishing the different spectral types. From Figure 3.12 , it is clear that Seyferts 2 present the highest values of the ionization parameter. Although there is an overlap between star-forming galaxies and LINERs, the peaks of their distributions are separated by more than 0.2 dex (see Table 3.9). This distinction between star-forming galaxies, Seyferts 2 and LINERs is in fact the underlying principle of work of the diagnostic diagrams (see section 1.3 for more details).

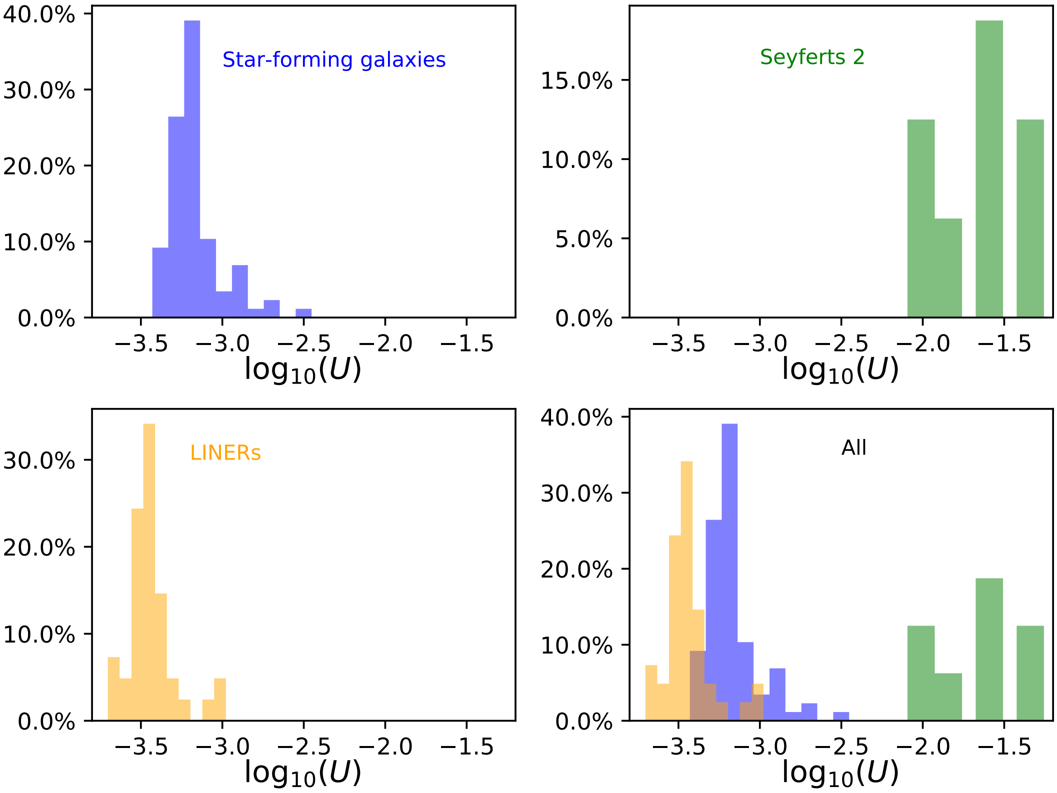

Figure 3.12: Distributions of the ionization parameter $\log_{10}(U)$ for star-forming galaxies, Seyferts 2 and LINERs.

$\log_{10}(U)$				
Type	**Number**	**Median**	**Std. Dev.**	**Range**
Star-forming	87	-3.21	0.17	[-3.43, -2.45]
Seyferts 2	16	-1.64	0.26	[-2.09, -1.25]
LINERs	41	-3.46	0.15	[-3.70, -2.98]

Table 3.9: Statistics of the ionization parameter for each spectral type.

4. Metallicity and host galaxy properties

Once the chemical abundances for star-forming galaxies and AGN are determined, an analysis of the different host galaxies properties (morphology, B-magnitude, H_α luminosity, SMBH mass and stellar mass) is provided in this chapter, quantifying their influence in the metallicity for each spectral type.

4.1 Morphology

The morphological type for each galaxy was retrieved from Ho et al. [1997a]. They used the classification presented by de Vaucouleurs [1963], where each morphological type is associated to a value of the parameter T (the so-called *de Vaucouleurs' number* or *morphological type*). The correspondence between the morphological classes (elliptical, lenticular, spiral, irregular,...) and T is presented in Table 4.1.

Morphological class	**T**	**Standard types**
Elliptical (E)	$[-6, -4]$	cE, E, E^+
Lenticular (S0)	$[-3, -1]$	$S0^-$, $S0^0$, $S0^+$
Early spiral (ES)	$[0, 2]$	S0/a, Sa, Sab
Intermediate spiral (IS)	$[3, 4]$	Sb, Sbc
Late spiral (LS)	$[5, 8]$	Sc, Scd, Sd, Sdm
Magellanic irregular (Irr)	$[9, 10]$	Sm, Im
Non-Magellanic irregular (Irr Non Mag)	90	Non-Magellanic irregular
Peculiar (Pec)	99	Peculiar

Table 4.1: Morphological classes used in this study.

The distribution of the morphological type (T) is shown in Figure 4.1. The different samples presented correspond to the sample constructed for the study (see section 2.2) and the final sample once galaxies with non-reliable determinations of the chemical abundances are excluded (see subsection 3.3.1). The relative distribution in Figure 4.1 (b) shows that during the construction of the samples, no bias is introduced in the morphological type (the p-value obtained through a KS-test is ≈ 0.18).

The distribution of the morphological class for each spectral type is presented in Figure 4.2 and the associated statistics in Table 4.2. The majority of star-forming galaxies (54.1%) present a late spiral morphology. Since later spiral types seems to have more star formation than earlier types [Ho et al. (1997b); Kennicutt (1998); Schiminovich et al. (2007); Guglielmo et al. (2015); González Delgado et al. (2017)], this result may reflect a relation between spectral types and star formation. The host galaxies of Seyferts 2 are mainly intermediate spiral galaxies (50.0%), which is in good agreement with previous studies [Ho

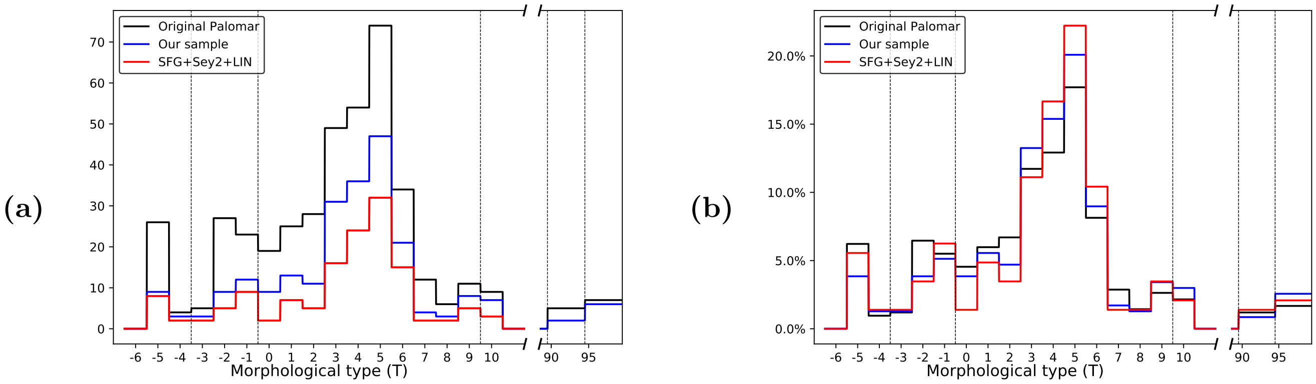

Figure 4.1: Absolute (a) and relative (b) distributions of the morphological type (T). The different colors indicate: black for all the galaxies with nuclear emission in the Palomar Survey (418 objects), blue for the galaxies in our sample (234 objects) and red for the sample composed by star-forming galaxies, Seyferts 2 and LINERs with reliable determinations in their chemical abundances (144 objects).

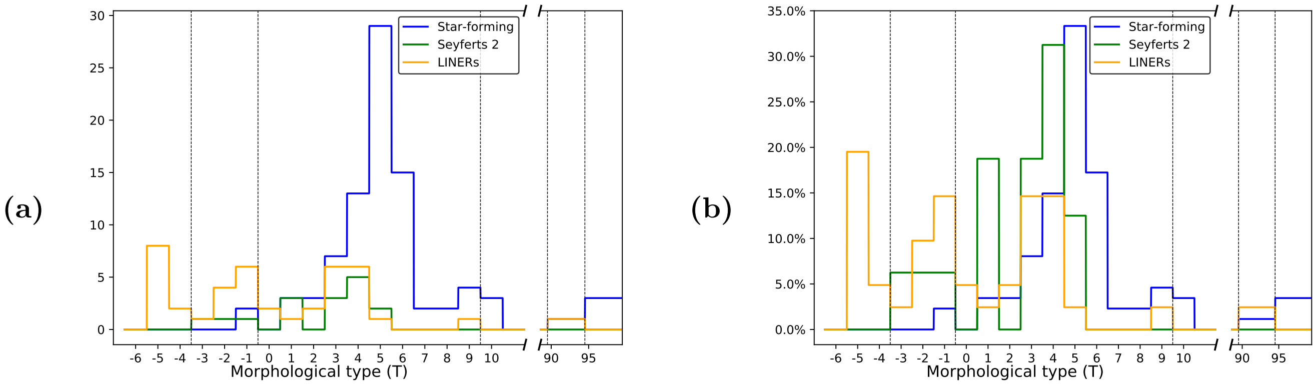

Figure 4.2: Absolute (a) and relative (b) distributions of De Vaucouleurs' number (T) for the different spectral types in our sample only considering galaxies with reliable determinations of their chemical abundances.

Spectral type	Number	Perc.* (%)	Median	Std. Dev.*	Minimum	Maximum
Star-forming	87	60.4	5	2.10	-1	99
Seyferts 2	16	11.1	3	2.43	-3	5
LINERs	41	28.5	-1	3.63	-5	90

Table 4.2: Morphological statistics for each spectral type. *The percentage (Perc.) is calculated excluding composite galaxies from the sample. **The standard deviation (Std. Dev.) is calculated considering only galaxies with morphological types $T \leq 10$.

et al. (1997b); Koulouridis et al. (2006); Slavcheva-Mihova and Mihov (2011); Chen and Hwang (2017)] showing that Seyferts 2 (Seyferts 1) are mainly located in late-type (early-type) galaxies. The distribution of LINERs is wider than both star-forming galaxies and Seyferts 2: ∼ 25% are hosted by ellipticals;

$\sim 25\%$ by lenticulars; and, $\sim 50\%$ by spiral galaxies. This distribution of LINERs agrees with the study by Ho et al. [1997b], but contrasts with Coldwell et al. [2018] where they found that LINERs are mainly ($\sim 70\%$) located in early-type galaxies (ellipticals and lenticulars).

Since some of our samples are not big enough for a very detailed binning in T (for instance, in our study only 16 galaxies are Seyferts 2), a total of eight morphological classes are considered in our study (see Table 4.1). Consequently, the statistics in each morphological type are increased, as Figure 4.3 shows (for more details on the associated statistics see Table 4.3).

Morphology	**Star-forming**	**Seyferts 2**	**LINERs**	**Total**	**Percentage (%)**
E	0 (0.0%)	0 (0.0%)	10 (24.4%)	10	6.9
S0	2 (2.3%)	3 (18.8%)	11 (26.8%)	16	11.1
ES	6 (6.9%)	3 (18.8%)	5 (12.2%)	14	9.7
IS	21 (24.2%)	8 (50.0%)	12 (29.4%)	41	28.5
LS	47 (54.1%)	2 (12.4%)	1 (2.4%)	50	34.7
Irr	7 (8.0%)	0 (0.0%)	1 (2.4%)	8	5.6
Irr. Non. Mag.	1 (1.1%)	0 (0.0%)	1 (2.4%)	2	1.4
Pec	3 (3.4%)	0 (0.0%)	0 (0.0%)	3	2.1
Sum	87 (100%)	16 (100%)	41 (100%)	144	100.0

Table 4.3: Distribution of galaxies for each morphological type. It is shown the number of objects for each morphological type and, within parenthesis, the percentage of the given morphological type for each spectral type.

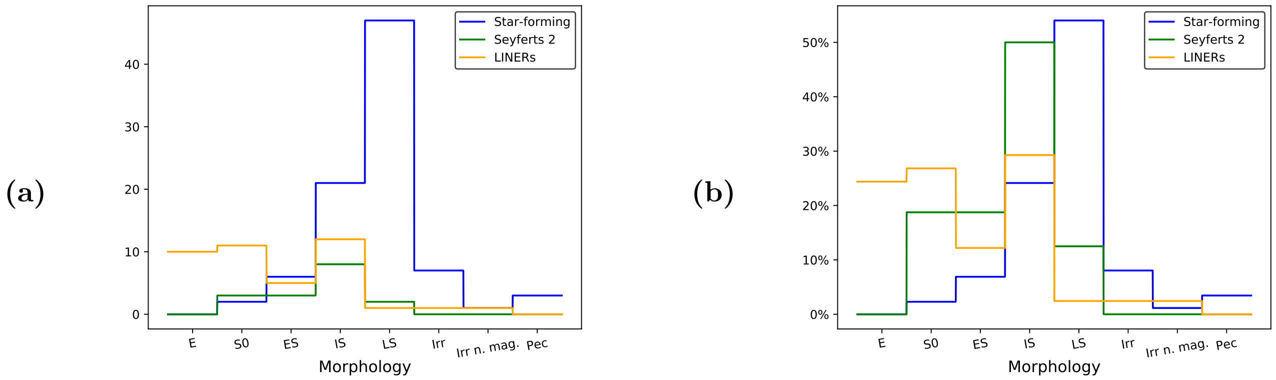

Figure 4.3: Absolute (a) and relative (b) distributions of the morphology (considering only the types defined in Table 4.1) for each spectral type.

The metallicities obtained for each morphological type considering only star-forming galaxies, Seyferts 2 and LINERs are shown in Figure 4.4 and the associated values are presented in Table 4.4. For lenticular (S0) and spiral galaxies, where the three spectral classes are presented, the chemical abundance $12 + \log_{10}(O/H)$ shows the highest values for Seyferts 2. While in S0 and IS galaxies this abundance presents a higher median value for Seyferts 2, in IS and LS galaxies the median values for Seyferts 2 are the lowest.

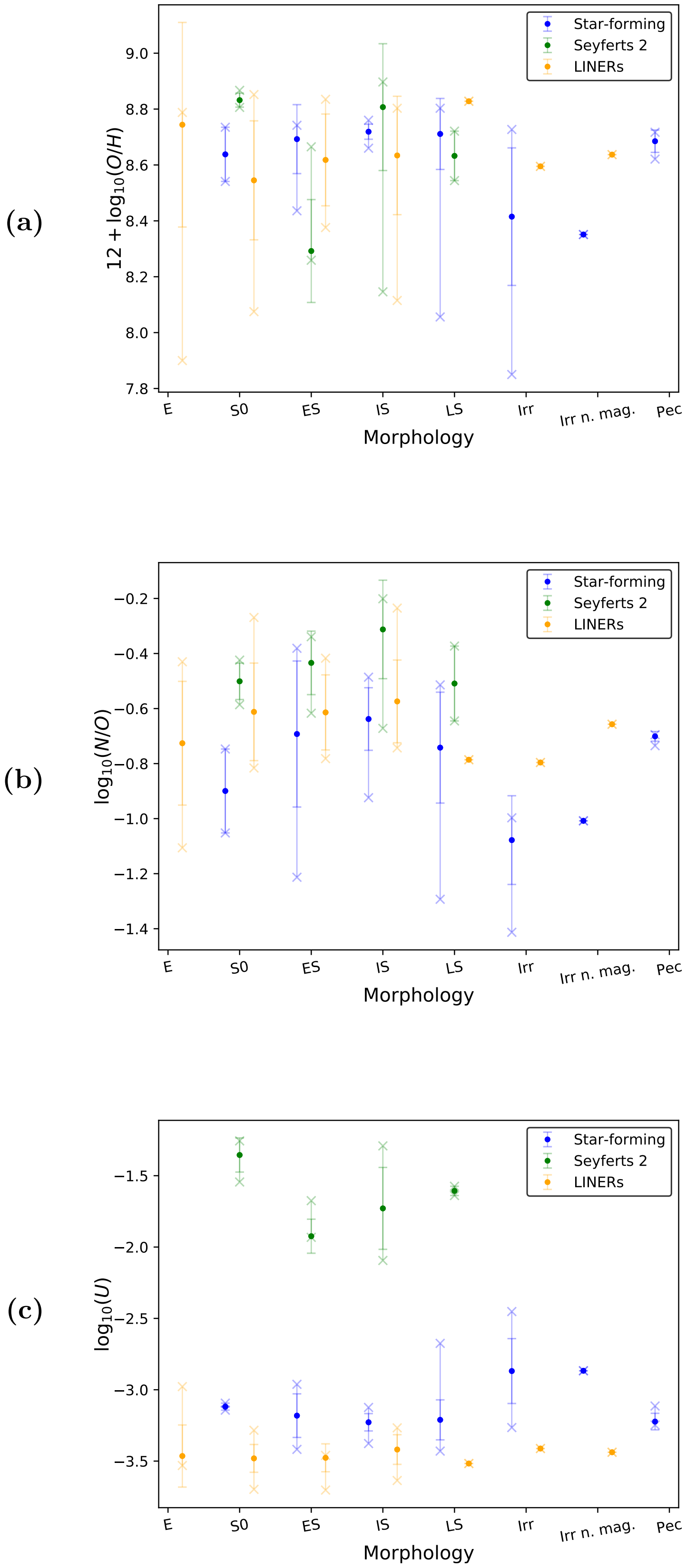

Figure 4.4: Chemical abundances $12+\log_{10}(O/H)$ (a) and $\log_{10}(N/O)$ (b) and ionization parameter $\log_{10}(U)$ (c) for each morphological type. The points correspond to the median value, the error bars marked with "-" denote the standard deviation and the error bars marked with "x" the minimum and maximum value for each morphology.

However, only 3 galaxies with ES (NGC 660, NGC 2273 and NGC 3185) and 2 with LS morphology (NGC 3486 and NGC 7479) host Seyferts 2, so this result must be confirmed in larger sample of galaxies. The median value of the chemical abundance ratio $\log_{10}(N/O)$ is higher in Seyferts 2 than in star-forming galaxies, and similar within the errors to those obtained for LINERs. In addition, for lenticular and spiral galaxies, the chemical abundance ratios $\log_{10}(N/O)$ obtained for LINERs are similar (within the errors) to those obtained for star-forming galaxies, although in lenticular galaxies the median value is higher in LINERs.

Morphology	**$12 + \log_{10}(O/H)$**		
	Star-forming	**Seyferts 2**	**LINERs**
E	-	-	8.74±0.37 [7.90, 8.79]
S0	8.64±0.10 [8.54, 8.73]	8.83±0.02 [8.81, 8.87]	8.55±0.21 [8.07, 8.85]
E.S.	8.69±0.12 [8.44, 8.74]	8.29±0.18 [8.26, 8.66]	8.62±0.21 [8.11, 8.80]
I.S.	8.72±0.03 [8.66, 8.76]	8.81±0.23 [8.15, 8.90]	8.63±21 [8.11, 8.80]
L.S.	8.71±0.13 [8.06, 8.80]	8.63±0.09 [8.54, 8.72]	8.83
Irr	8.41±0.25 [7.85, 8.73]	-	8.60
Irr Non Mag	8.35	-	8.64
Pec	8.69±0.04[8.62, 8.72]	-	-

Morphology	**$\log_{10}(N/O)$**		
	Star-forming	**Seyferts 2**	**LINERs**
E	-	-	-0.73±0.22 [-1.11, -0.43]
S0	-0.90±0.15 [-1.05, -0.75]	-0.50±0.07 [-0.59, -0.42]	-0.61±0.18 [-0.82, 0.27]
E.S.	-0.69±0.27 [-1.21, -0.38]	-0.43±0.12 [-0.62, -0.34]	-0.61±0.14 [-0.78, -0.42]
I.S.	-0.64±0.11 [-0.92, -0.49]	-0.31±0.18 [-0.67, -0.20]	-0.57±0.15 [-0.74, -0.23]
L.S.	-0.74±0.20 [-1.29, -0.51]	-0.51±0.14 [-0.64, -0.37]	-0.79
Irr	-1.08±0.16 [-1.41, -1.00]	-	-0.80
Irr Non Mag	-1.01	-	-0.66
Pec	-0.70±0.02[-0.74, -0.69]	-	-

Morphology	**$\log_{10}(U)$**		
	Star-forming	**Seyferts 2**	**LINERs**
E	-	-	-3.46±0.22 [-3.53, -2.98]
S0	-3.12±0.02 [-3.14, -3.09]	-1.36±0.12 [-1.54, -1.26]	-3.48±0.10 [-3.70, -3.28]
E.S.	-3.18±0.15 [-3.42, -2.96]	-1.92±0.12 [-1.93, -1.67]	-3.48±0.10 [-3.70, -3.46]
I.S.	-3.23±0.06 [-3.38, 3.12]	-1.73±0.29 [-2.09, -1.29]	-3.42±0.10 [-3.64, -3.27]
L.S.	-3.21±0.14 [-3.43, -2.67]	-1.61±0.03 [-1.64, -1.57]	-3.52
Irr	-2.87±0.23 [-3.27, -2.45]	-	-3.41
Irr Non Mag	-2.87	-	-3.44
Pec	-3.22±0.06[-3.25, -3.11]	-	-

Table 4.4: Statistics of the chemical abundances and ionization parameters for each morphological type. The median values are presented with the minimum and maximum in the form: median± standard deviation [minimum, maximum]. Only star-forming galaxies, Seyferts 2 and LINERs are considered. The statistics when the number of objects is smaller than 3 are presented in color red.

Focusing on star-forming galaxies, there is little change in the chemical abundance $12 + \log_{10}(O/H)$

in S0, ES, IS, LS and peculiar galaxies, showing a median value around the solar value $12+\log_{10}(O/H) = 8.69$. For irregular galaxies (both types), this abundance drops to the sub-solar values $12+\log_{10}(O/H) \approx 8.40$. The same behavior is presented in the chemical abundance ratio $\log_{10}(N/O)$, where for spiral and peculiar galaxies the median value remains at ≈ -0.70. However, in lenticular galaxies this abundance drops to ≈ -0.90, similar value that those obtained for irregular galaxies. Since only two star-forming galaxies present a lenticular morphology (NGC 4124 and NGC 4460), this result needs to be confirmed in a larger sample. The ionization parameter also presents slightly higher values in irregular than in lenticular, spiral and peculiar galaxies, although the median values are compatible for all morphologies within the errors.

Analyzing Seyferts 2, the chemical abundance $12+\log_{10}(O/H)$ shows higher values (≈ 8.80) in S0 and IS galaxies than in ES and LS galaxies. It should be noticed that this abundance in ES galaxies is quite low (≈ 8.29) in comparison with the other types. Since only 3 Seyferts 2 are hosted by ES galaxies (NGC 660, NGC 2273 and NGC 3185), this last result must be contrasted with larger samples. The differences in the oxygen to hydrogen abundance are not correlated with the nitrogen to oxygen abundance ratio, that presents the same value for S0 and LS galaxies ($\log_{10}(N/O) \approx -0.50$) and increases for ES and IS galaxies. This result is in good agreement with our study in subsection 3.3.3, where the $\log_{10}(N/O)$ vs $12+\log_{10}(O/H)$ diagram (see Figure 3.4) shows that there is no correlation between both abundances. Finally, the ionization parameter shows the highest values for lenticular (S0) galaxies, with a median $\log_{10}(U) \approx -1.40$.

In the case of LINERs, the chemical abundance $12+\log_{10}(O/H)$ slightly varies from the median value of ≈ 8.63 (solar metallicity). This median value increases to $12+(O/H) \approx 8.74$ in the case of elliptical (E) galaxies. This increase from later-types (spiral galaxies) to early-types (elliptical galaxies) is expected since the later ones usually present old stellar populations [Kennicutt (1998); Sparke and Gallagher III (2007)], i.e., stars are in their later stages of evolution and have already deposited into the ISM the metals generated during the stellar nucleosynthesis process. Although there is a slight increase in the oxygen to hydrogen abundance for LS galaxies ($12+\log_{10}(O/H) \approx 8.83$), only one LINER presents this morphology (NGC 4651), thus this result must be confirmed with larger samples. While the median values of the chemical abundance ratio $\log_{10}(N/O)$ show little variation, the highest values are obtained for elliptical, lenticular and ES galaxies, which reinforces the previous statement that the ISM is rich in metals for early-type galaxies. The ionization parameter is virtually the same for all the morphologies with a median value $\log_{10}(U) \approx -3.46$.

As a conclusion from this morphological study, the chemical abundance $12+\log_{10}(O/H)$ is slightly affected by the morphological type, although in star-forming galaxies there is an important decrease in irregular galaxies. Considering a particular morphological type, the chemical abundance ratio $\log_{10}(N/O)$ is higher in Seyferts 2 than in LINERs or star-forming galaxies, that present similar values. The ionization parameter $\log_{10}(U)$ is only affected by the morphological type in star-forming galaxies, while for AGN it practically remains constant.

4.2 Absolute B-magnitude

The absolute B-magnitude (M_B) of a galaxy is a measured of its luminosity in the B-band defined in the Johnson-Morgan system (or UBV system) of filters [Johnson and Morgan (1953)]. Since the B-filter has an effective wavelength $\lambda_{eff} = 4360\mathring{A}$ and a bandwidth $\Delta\lambda = 960\mathring{A}$ [Johnson and Morgan (1953)], this filter provides the luminosity of the blue light emitted by the galaxy.

The values of the apparent B-magnitude (m_B) were taken from Ho et al. [1997a]. The relation between absolute and apparent magnitude, given by:

$$M_B = m_B - 5\log_{10}(d[Mpc]) - 25 \tag{4.1}$$

where d is the distance of the galaxy. The values of the distance for each galaxy were also taken from Ho et al. [1997a], who used the Nearby Galaxies Catalog by Tully [1988] to determine the distance for galaxies with $d < 40\ Mpc$ and the Hubble's law ($v = H_0 d$) for the remaining, assuming a value of the Hubble constant $H_0 = 75\ km \cdot s^{-1} \cdot Mpc^{-1}$.

Since Ho et al. [1997a] provide observed apparent B-magnitudes, it is needed to correct them from reddening. In this case, the values of $c\,(H_\beta)$ determined in section 3.1 cannot be used because they express the reddening only associated to their nuclei. Since the B-magnitude is from the whole galaxy, only the second source of reddening must be considered. The values of the galactic reddening (denoted as *galactic reddening magnitude*, A_g) used by Ho et al. [1997a] were retrieved from the HI maps presented by Burstein and Heiles [1982; 1984]. While Ho et al. used the extinction curve by Cardelli [1989], that by Howarth [1983] is used in our study. Both extinction curves are related by Equation (1.13), so the absolute B-magnitude corrected from reddening is obtained by adding to Equation (4.1) the reddening correction, i.e.:

$$M_B^0 = m_{b,obs} - 5\log_{10}(d\,[Mpc]) - 25 - \frac{A_g}{R_\nu} f\,(\lambda_B) \tag{4.2}$$

where the wavelength λ_B is the effective wavelength in the B-filter, f is the extinction curve by Howarth [1983] and $R_\nu = 3.1$ is assumed (see subsection 1.2.4 for more details on this assumption).

Spectral type	Number	Median	Std. Dev.	Min.	Max.
Star-forming	87	-19.48	1.20	-23.72	-15.94
Seyferts 2	16	-19.92	1.16	-21.99	-18.31
LINERs	41	-20.16	1.32	-22.26	-15.22

Table 4.5: Statistics of the absolute B-magnitude for each spectral type.

Figure 4.5 shows the distribution of the corrected absolute B-magnitude (M_B^0). During the construction of the different samples, no change is induced in the distribution of M_B^0, i.e., no bias is introduced (the p-value obtained through a KS-test is ≈ 0.31). All the distributions seems to be symmetric with a median value around $M_B^0 \approx [-20.5, -19.5]$.

Analyzing the distribution for each spectral type (see Figure 4.6 and Table 4.5), star-forming galaxies

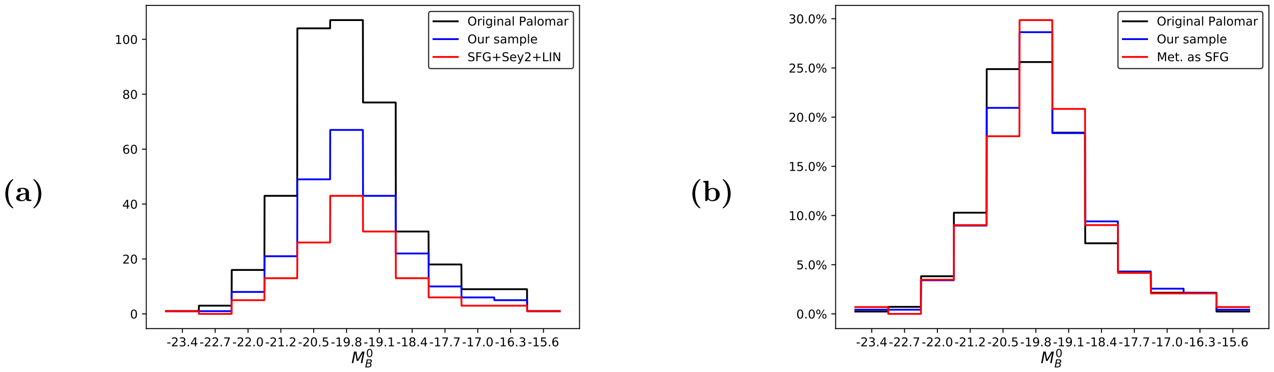

Figure 4.5: Absolute (a) and relative (b) distributions of the absolute B-magnitudes corrected from reddening (M_B^0). The different colors indicate: black for all the galaxies with nuclear emission in the Palomar Survey (418 objects), blue for the galaxies in our sample (234 objects) and red for the sample composed by star-forming galaxies, Seyferts 2 and LINERs with reliable determinations in their chemical abundances (144 objects).

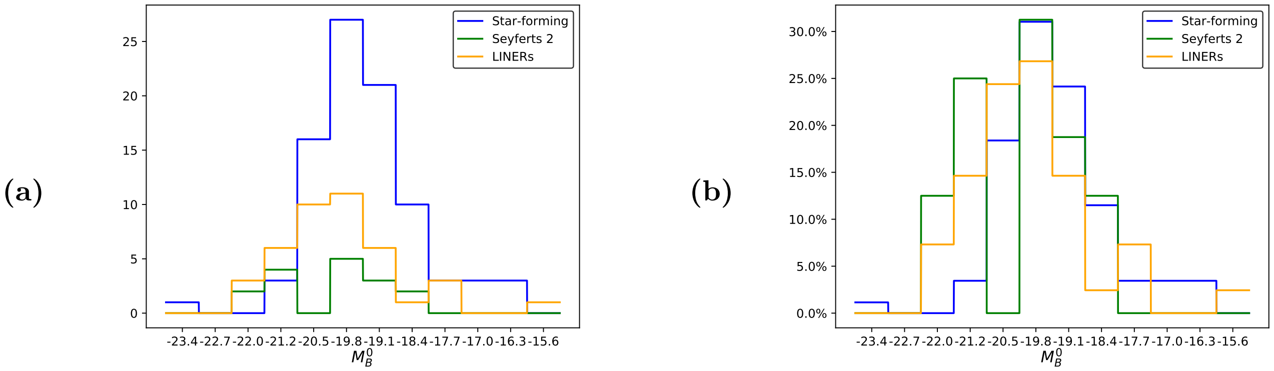

Figure 4.6: Absolute (a) and relative (b) distributions of the absolute B-magnitudes (M_B^0) corrected from reddening for the different spectral types in our sample, only considering galaxies with reliable determinations of their chemical abundances.

present fainter luminosities (higher values of the B-magnitude) than AGN: only $\sim 5\%$ of star-forming galaxies have magnitudes $M_B^0 < -20.5$, while this percentage increases to $\sim 37.5\%$ in Seyferts 2 and $\sim 20\%$ in LINERs. This result is in good agreement with Ho et al. [1997b], where they found that the median value for Seyferts 2 ($M_B^0 = -20.46$) was lower than for star-forming galaxies ($M_B^0 = -20.01$). In our study, the median value for Seyferts 2 is $M_B^0 = -19.91$ while for star-forming galaxies it is $M_B^0 = -19.48$. Considering LINERs, they have a slightly higher median value $M_B^0 = -20.16$, but it remains compatible within the errors with the previous ones.

In general, for a given value of M_B^0, there is no significant differences in the chemical abundance $12 + \log_{10}(O/H)$ between Seyferts 2 and LINERs, since both present a considerable dispersion of values (see Figure 4.7 (b)). In addition, M_B^0 is not correlated with this chemical abundance in AGN (the Pearson

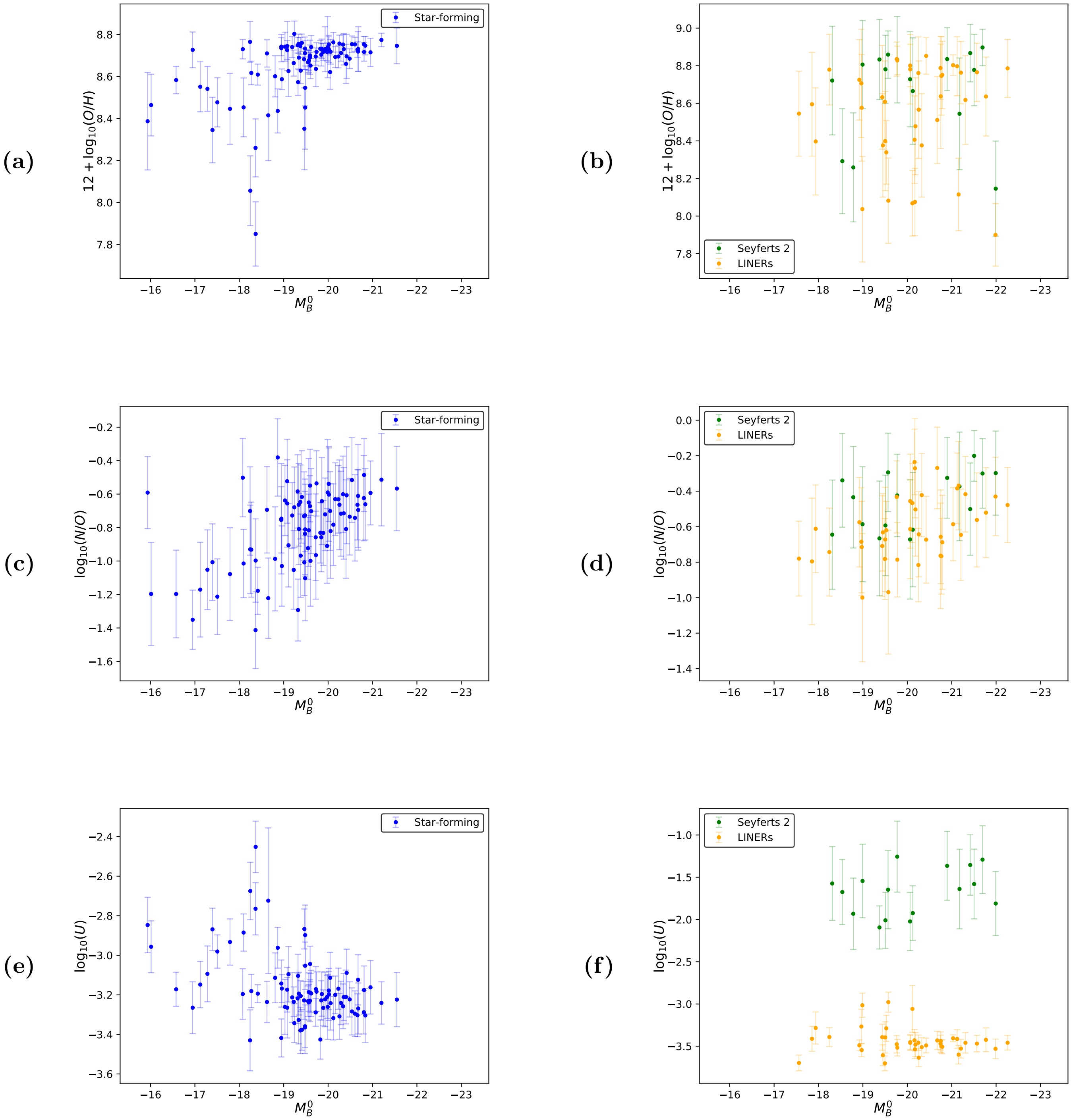

Figure 4.7: Chemical abundances $12 + \log_{10}(O/H)$ (a) and (b), $\log_{10}(N/O)$ (c) and (d) and ionization parameter $\log_{10}(U)$ (e) and (f) vs the corrected absolute B-magnitude (M_B^0). The left column shows the results for star-forming galaxies and the right column those for AGN (Seyferts 2 and LINERs).

correlation coefficient for Seyferts 2 is $r = -0.076$ and $r = 0.0028$ for LINERs), which contrasts with the study at high redshift of quasars presented by Nagao et al. [2006], where a strong correlation was found between the chemical abundance and the luminosity of the galaxy. Star-forming galaxies cluster around around $12 + \log_{10}(O/H) \approx 8.7$ (solar-values) for galaxies brighter than $M_B^0 \sim -19.5$ (see Figure 4.7 (a)). For lower luminosities, the chemical abundance shows a decrease to sub-solar values. Following the discussion presented in subsection 3.3.2, this result might be interpreted as the most luminous star-forming galaxies ($M_B^0 < -19.5$) are those which present a correlation between $\log_{10}(N/O)$ and $12 + \log_{10}(O/H)$, i.e., the most luminous star-forming galaxies are those that present a secondary origin of the nitrogen (the ISM of these galaxies is already rich in carbon and oxygen). This slightly increase of $12+\log_{10}(O/H)$ with the luminosity in star-forming galaxies was already reported by several studies [Lequeux et al. (1979); Contini et al. (2002); Melbourne and Salzer (2002); Lamareille et al. (2004); Tremonti et al. (2004); Izotov et al. (2015)]. In addition, our study shows that for magnitudes $M_B^0 < -19.5$, there is a saturation in the values and does not increase with the luminosity, remaining at solar values.

The plot of the chemical abundance ratio $\log_{10}(N/O)$ versus M_B^0 (Figure 4.7 (c)) reinforces that the most luminous star-forming galaxies have a secondary origin in their nitrogen, since this abundance increases with the luminosity, although the Pearson correlation coefficient is low ($r = 0.38$). In addition, for $M_B^0 > -19.5$ (low luminosities), the chemical abundance ratio $\log_{10}(N/O)$ remains constant at a value ≈ -1.30 for star-forming galaxies, which is the expected behavior for a primary origin of the nitrogen [Vila-Costas and Edmunds (1993); Andrews and Martini (2013); Vincenzo et al. (2016)]. There seems to be a trend in the chemical abundance ratio $\log_{10}(N/O)$ in LINERs, but this is not case for Seyferts 2, where $\log_{10}(N/O)$ gets values around ≈ -0.30 (see Figure 4.7 (d)).

Finally, the ionization parameter $\log_{10}(U)$ does not present any correlation with M_B^0 in AGN (see Figure 4.7 (f)) since for Seyferts 2 the Pearson correlation coefficient is $r = 0.32$ and $r = 0.18$ for LINERs. In the case of star-forming galaxies, there is an increase of the ionization parameter for magnitudes $M_B^0 \in [-18, -16.5]$ (see Figure 4.7 (e)), but the Pearson coefficient correlation ($r = 0.081$) shows that they are actually not correlated.

In conclusion, $12 + \log_{10}(O/H)$ and $\log_{10}(N/O)$ increase with M_B^0 for $M_B^0 > -19.5$ and remain constant for higher luminosities only in star-forming galaxies. For AGN, M_B^0 is not correlated with the chemical abundances. The ionization parameter $\log_{10}(U)$ is not affected by M_B^0 for both star-forming galaxies and AGN, although in the former ones presents a slightly increase.

4.3 H_α luminosity

The luminosity of the Balmer line H_α provides additional information of both, star-forming regions and AGN. Considering star-forming regions, studies of the local Universe [Kennicutt (1998); Tresse and Maddox (1998); Kennicutt et al. (2009)] have shown that the luminosity $L(H_\alpha)$ is related to the star-formation rate (hereafter SFR) by:

$$\text{SFR}\ \left[M_\odot \cdot yr^{-1}\right] = 7.9 \cdot 10^{-42} \cdot L(H_\alpha)\ \left[ergs \cdot s^{-1}\right] \tag{4.3}$$

In AGN, the H_α luminosity is related to the optical continuum luminosity (L_{op}), with a slope between the logarithm of both luminosities close to unity [Shuder (1981); Greene and Ho (2005)]. This relation between the emission lines and the continuum emission favors the photoionization model for the emission lines in AGN [Shuder (1981)].

Ho et al. [1997a] provide the H_α luminosity without taking into account the correction from reddening. Although this emission line is less affected by reddening than bluer lines, the correction in the sample supposes a median increase $\Delta \log_{10}[L(H_\alpha)] = 0.39 \pm 0.32$. In this case, our study is focused on the luminosity emitted by the nuclear region of the galaxies, so the extinction correction must take into account both the internal and galactic reddening. Therefore, the values of the extinction parameter $c(H_\beta)$ obtained in section 3.1 are used here, with the extinction curve f by Howarth (Equation (1.11)), in order to correct from reddening the luminosity, as:

$$\log_{10}(L(H_\alpha)_{Corr}) = \log_{10}(L(H_\alpha)_{Obs}) + c(H_\beta)\frac{f(H_\alpha)}{f(H_\beta)} \tag{4.4}$$

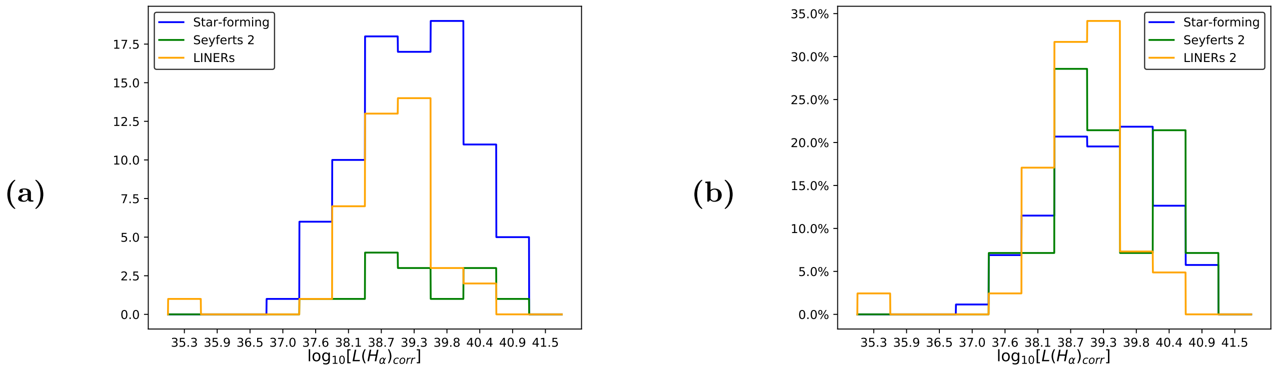

Figure 4.8: Absolute (a) and relative (b) distributions of H_α luminosities ($L(H_\alpha)$) corrected from reddening for the different spectral types, only considering galaxies with reliable determinations of their chemical abundances.

Spectral type	Number	Median	Std. Dev.	Min.	Max.
Star-forming	87	39.22	0.93	36.82	41.01
Seyferts 2	16	39.64	0.92	37.86	40.95
LINERs	41	38.84	0.83	35.06	40.33

Table 4.6: Statistics of $\log_{10}[L(H_\alpha)_{corr}]$ for each spectral type.

The inspection of Figure 4.8 and Table 4.6 shows that the distribution of H_α luminosity is pretty similar for all the spectral types, although the median value for LINERs is slightly lower. It should be noticed that the LINER galaxy NGC 185 presents a extremely low H_α luminosity ($< 10^{36}\ erg \cdot s^{-1}$), being in fact a dwarf elliptical galaxy and, hence, will not be considered for this study (see section 4.4).

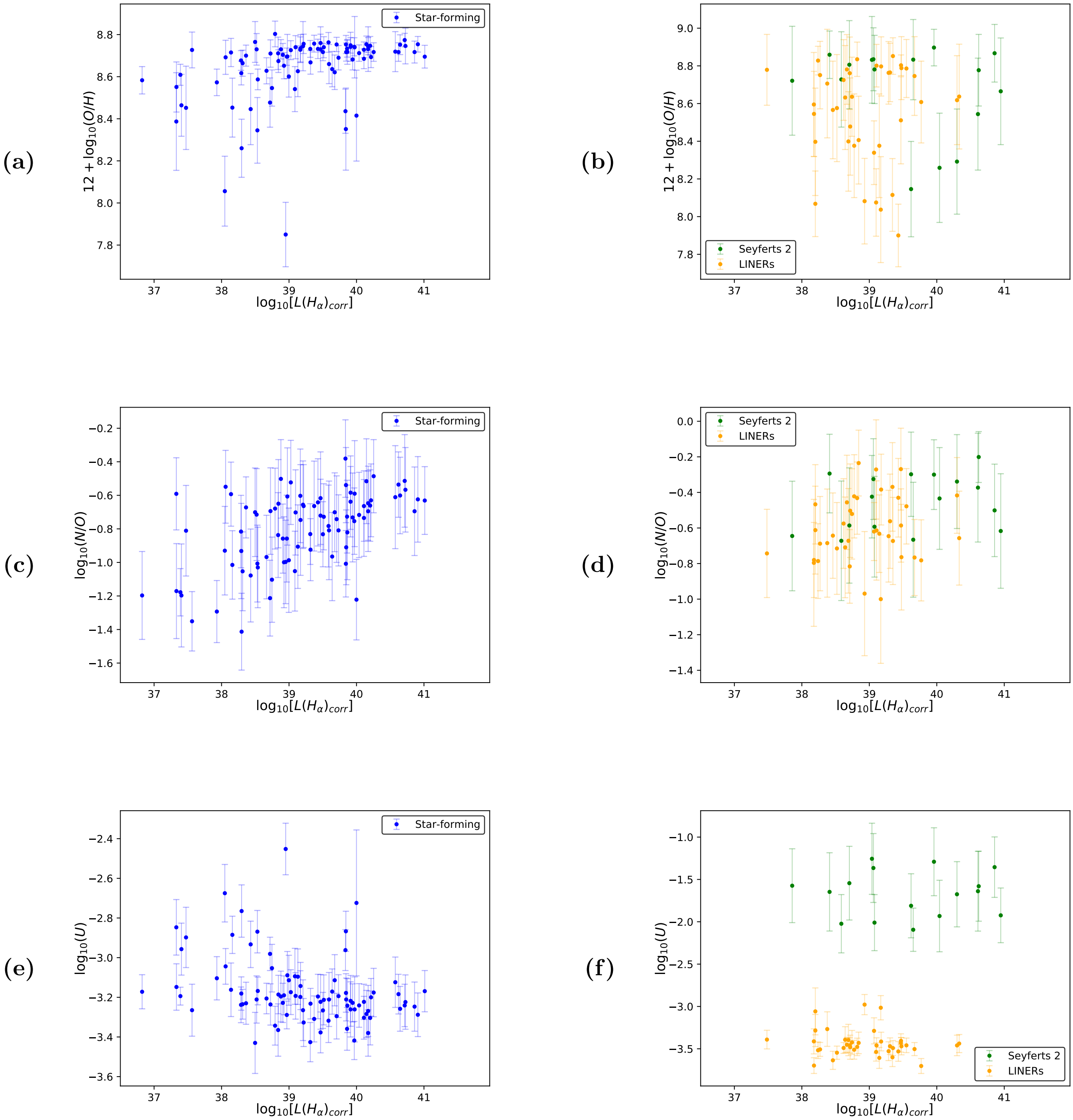

Figure 4.9: Chemical abundances $12+\log_{10}(O/H)$ (a) and (b), $\log_{10}(N/O)$ (c) and (d) and ionization parameter $\log_{10}(U)$ (e) and (f) vs the corrected H_α luminosity $\log_{10}[L(H_\alpha)_{corr}]$. The left column shows the results for star-forming galaxies and the right column those for AGN (Seyferts 2 and LINERs).

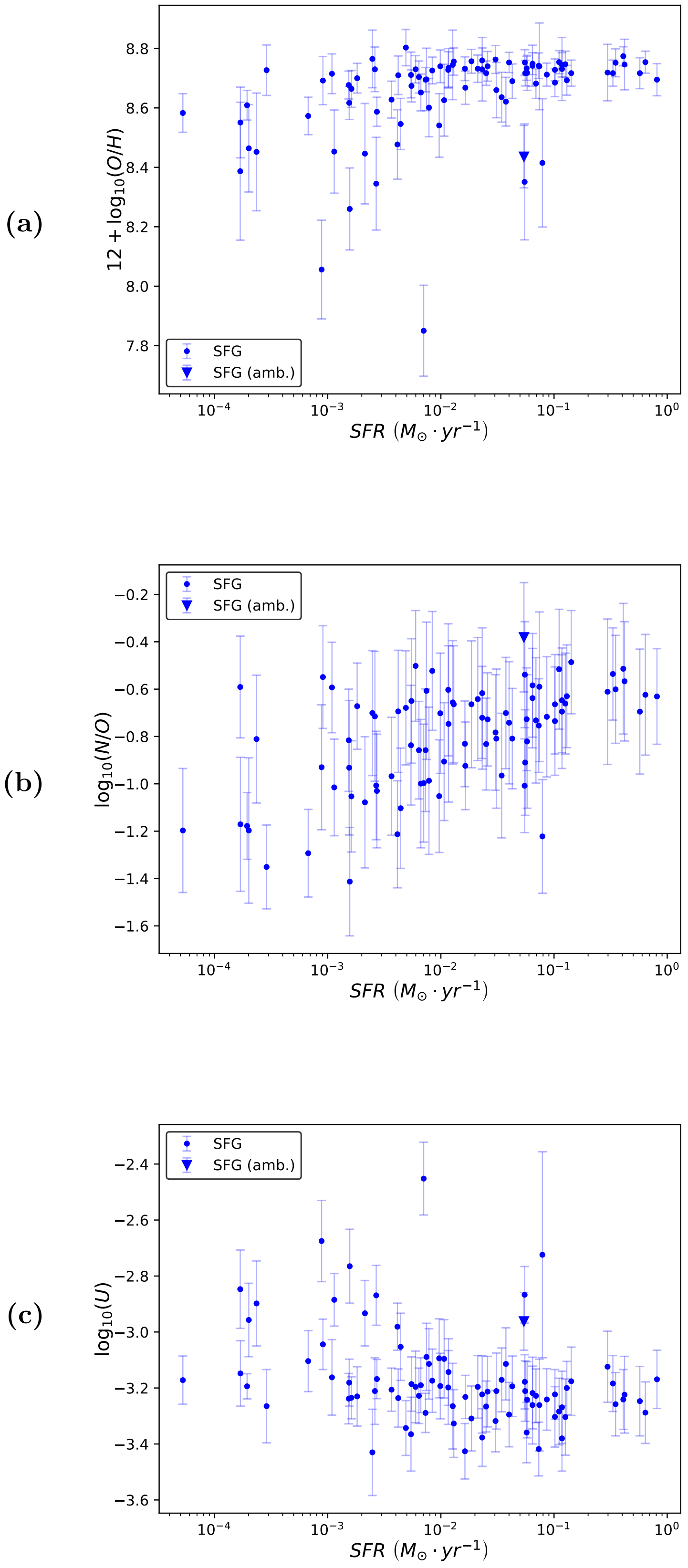

Figure 4.10: Chemical abundances $12 + \log_{10}(O/H)$ (a) and $\log_{10}(N/O)$ (b) and ionization parameter $\log_{10}(U)$ (c) vs the star formation rate (SFR).

The plot $12 + \log_{10}(O/H)$ vs $\log_{10}(L(H_\alpha))$ (see Figure 4.9 (b)) shows that there is little correlation between both quantities for AGN (the Pearson correlation coefficients are $r = -0.25$ and $r = -0.087$ for Seyferts 2 and LINERs, respectively). For star-forming galaxies (Figure 4.9 (a)), the highest values of the chemical abundance $12 + \log_{10}(O/H)$ are obtained for the highest luminosities ($L(H_\alpha) > 10^{39}\ ergs \cdot s^{-1}$), where the chemical abundance remains constant at a value $12 + \log_{10}(O/H) \approx 8.70$ (solar abundance).

The chemical abundance ratio $\log_{10}(N/O)$ shows a slightly increase (the Pearson correlation coefficient is $r = 0.56$) with the H_α luminosity for star-forming galaxies, being more correlated with this luminosity than the absolute B-magnitude (see section 4.2 for more details). For AGNs, no correlation between $\log_{10}(N/O)$ and $L(H_\alpha)$ is observed since the Pearson correlations coefficients are $r = 0.30$ for Seyferts 2 and $r = 0.42$ for LINERs (see also Figure 4.9 (d)).

The ionization parameter $\log_{10}(U)$ seems to be independent of the H_α luminosity in both star-forming galaxies ($r = -0.33$) and AGN ($r = 0.00031$ and $r = -0.17$ for Seyferts 2 and LINERs, respectively), as it can be seen in Figure 4.9 (e) and (f).

For star-forming the H_α luminosity is translated into star-formation rate by Equation (4.3). The SFR for these galaxies and their relation with the chemical abundances and ionization parameters are shown in Figure 4.10. Since SFR and $L(H_\alpha)$ are directly proportional, the same behavior discussed above for star-forming galaxies in $L(H_\alpha)$ is also presented in SFR. The plot $12 + \log_{10}(O/H)$ vs SFR shows that in star-forming galaxies there is little correlation between both magnitudes, although there is a slightly decrease in the chemical abundance for the lowest star-formation rates ($SFR < 10^{-3}\ M_\odot \cdot yr^{-1}$). This lack of correlation between SFR and $L(H_\alpha)$ is in good agreement with the study presented by Sánchez et al. [2013] for the CALIFA Survey, where they show that there is no correlation between metallicity and SFR, although several studies suggest the opposite [Ellison et al. (2007); Yates et al. (2012); Andrews and Martini (2013); Salim et al. (2014)]. To explain this behavior, Sánchez et al. [2013] propose that, although SFR depends on the gas inflow rate, which is expected to dilute the oxygen abundance, the star formation is a local process (not radial as the gas movement) that might enrich the falling gas due to the different time scales of the processes.

4.4 Supermassive black hole masses in AGN

The mass of the SMBH (M_{SMBH}) in AGN is an important parameter. The study by Heckman and Best [2014] shows that AGN with prominent jets are associated to higher masses of the SMBH. In addition, the Eddington ratio depends on M_{SMBH} (see Equation (1.1)), and this ratio is proposed to be related to the Unified Model for AGN when LINERs are taken into account [Márquez et al. (2017)].

The relation between this quantity and the stellar velocity dispersion $\sigma_{central}$ in the galactic nucleus given by Equation (1.2) is used to estimate the masses of the SMBH. This relation can only be applied in AGN hosted by galaxies that present a velocity dispersion structure (bulge or elliptical core). Since the host galaxy of NGC 5363 (LINER) has an irregular morphology, this galaxy will be omitted from the study. The values of $\sigma_{central}$ are retrieved from the catalog presented by Ho et al. [2009], where they combined determinations from the nuclear spectra in the Palomar Survey and results from previous and independent studies.

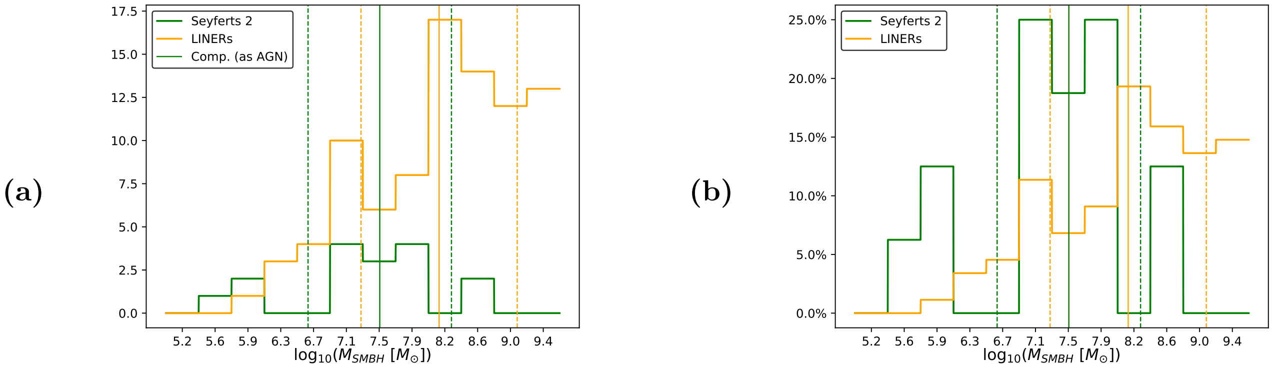

Figure 4.11: Absolute (a) and relative (b) distributions of SMBH masses $\log_{10}(M_{SMBH}\ [M_\odot])$ for AGN. The solid vertical lines represent the median values and the dashed vertical lines the standard deviations.

Spectral type	Number	Median	Std. Dev.	Min.	Max.
Seyferts 2	16	7.48	0.84	5.57	8.55
LINERs	41	8.17	0.91	5.86	9.38

Table 4.7: Statistics of $\log_{10}(M_{SMBH}\ [M_\odot])$ for each spectral type.

For this study, only Seyferts 2 and LINERs are considered. Analyzing the distribution of M_{SMBH} (see Figure 4.11 and Table 4.7), Seyferts 2 present masses in the range $10^{5.67} - 10^{8.56}\ M_\odot$, in agreement with the range $10^{6.04} - 10^{8.44}\ M_\odot$ obtained by Bian and Gu [2007]. In the case of LINERs, excluding the galaxy NGC 185, this range of the black hole masses is $10^{5.86} - 10^{9.38}\ M_\odot$, which agrees with the range $10^{6.0} - 10^{9.5}\ M_\odot$ obtained by Nisbert and Best [2015]. The M_{SMBH} determined in NGC 185 is extremely low ($\approx 10^{2.7}\ M_\odot$) as a consequence of its low stellar velocity dispersion $\sigma_* \approx 19.9\ km \cdot s^{-1}$, and this might be explained because this dwarf elliptical galaxy present several bright knots that may be identified as its nucleus [Lira et al. (2007)], being also a posible explanation for its low H_α luminosity (see section 4.3). A detailed analysis should be done on NGC 185, thus it is excluded in our study. The median SMBH mass for LINERs $M_{SMBH} \approx 10^{8.19}\ M_\odot$, higher than for Seyferts 2 $M_{SMBH} \approx 10^{7.48}\ M_\odot$, was already reported in previous studies [Panessa et al. (2006); Nisbet and Best (2015)].

The metallicity $12 + \log_{10}(O/H)$ does not show any correlation with M_{SMBH} for neither AGN type (see Figure 4.12 (a)), being the Pearson correlation coefficients $r = 0.21$ and $r = -0.059$ for Seyferts 2 and LINERs, respectively. A similar behavior is presented in the chemical abundance ratio $\log_{10}(N/O)$ (see Figure 4.12 (b)), although the correlation coefficients are slightly higher: $r = 0.43$ (Seyferts 2) and $r = 0.33$ (LINERs). The ionization parameter $\log_{10}(U)$ remains practically constant, although in Seyferts 2 a slightly increase ($r = 0.55$) for $M_{SMBH} > 10^7\ M_\odot$ is seen in Figure 4.12 (c).

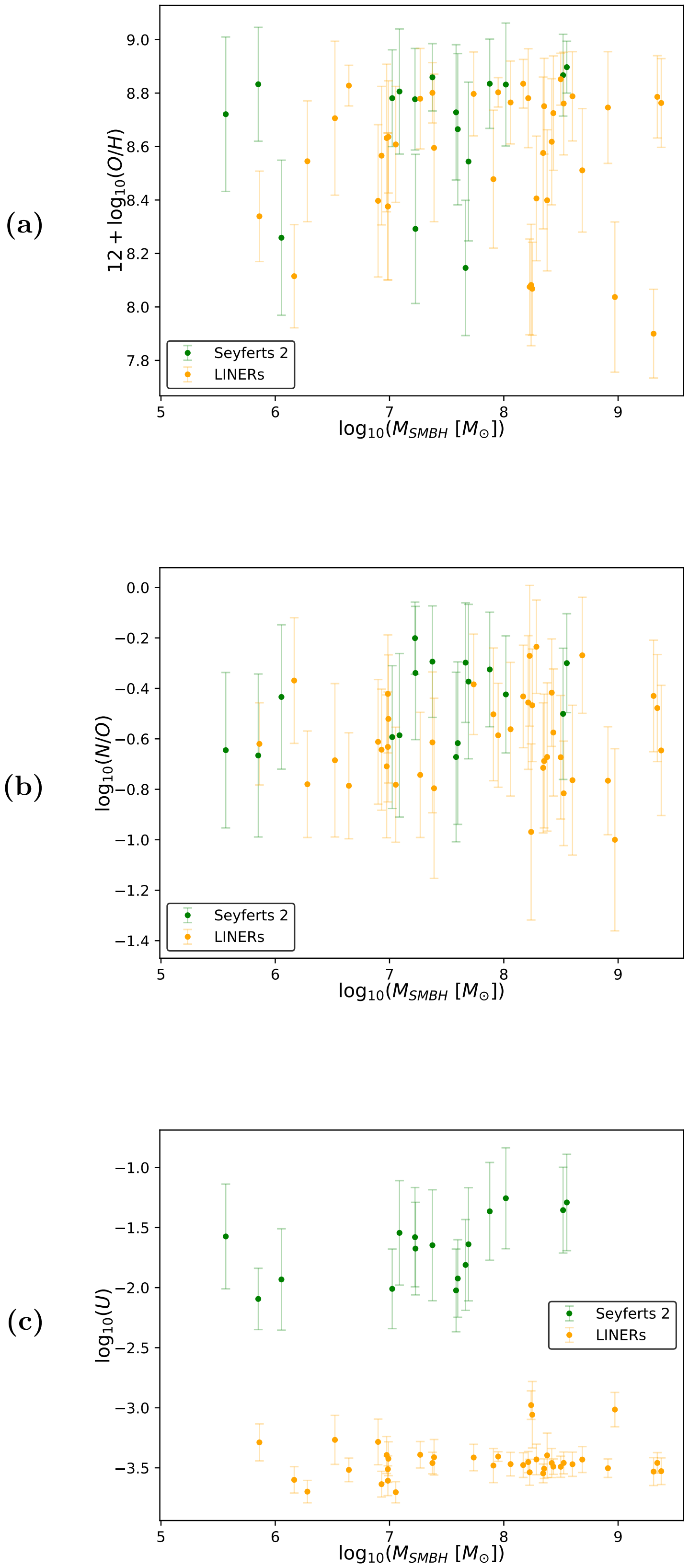

Figure 4.12: Chemical abundances $12 + \log_{10}(O/H)$ (a) and $\log_{10}(N/O)$ (b) and ionization parameter $\log_{10}(U)$ (c) vs the SMBH mass M_{SMBH} for AGN.

4.5 Stellar mass

The relation between the ISM metallicity and the stellar mass was firstly observed for the Local Group of galaxies [Van den Bergh (1968)]. The subsequent studies by Lequeux et al. [1979] and Kinman and Davidson [1981] studying star-forming galaxies, corroborated the existence of such a relation in larger samples of galaxies. In the recent years, this relation in star-forming galaxies has been confirmed in several orders of magnitude larger samples at low redshift [Contini et al. (2002); Melbourne and Salzer (2002); Lamareille et al. (2004); Tremonti et al. (2004)], and also at high redshift [Erb et al. (2006a); Izotov et al. (2015); Gao et al. (2018); Torrey et al. (2019)]. More recently, studies of Seyferts 2 show that this relation can be also applied for the NLR of this type of AGN at low [Thomas et al. (2019); Dors et al. (2019)] and high [Matsuoka et al. (2018)] redshift.

Several models have been proposed in other to explain this metallicity-stellar mass relation in star-forming galaxies. Some of them proposed a selective loss of metals from galaxies with shallow gravitational potentials through galactic outflows [Tremonti et al. (2004)]. Others contemplate that, in average, high mass galaxies evolve faster than low mass galaxies, so the ISM in the former ones is more rich in metals [Erb et al. (2006b)]. There are also models that suggest that the recycled gas from previous periods of star-formation can be richer in metals in high mass galaxies [Ma et al. (2015); Vincenzo et al. (2015)]. Nevertheless, the origin of this relation is still an open question. It must be noticed that Dors et al. [2019] found that there is no such a correlation when the chemical abundances are derived by strong emission line calibrators. A thorough and recent review of this topic can be found in Mailoino and Manucci [2019].

To analyze this issue in our sample of galaxies, their stellar masses are calculated by using the empirical calibration, based on infrared magnitudes used in the *Wide-field Infrared Survey Explorer* (hereafter WISE), presented by Cluver et al. [2014]. They found that the absolute magnitude in the W1-band (at $\lambda = 3.4\mu m$), M_{W_1}, and in the W2-band (at $\lambda = 4.6\mu m$), M_{W_2}, trace the stellar mass for galaxies at low redshift by the relation:

$$\log_{10}\left(\frac{M_*\,[M_\odot]}{L_{W_1}\,[L_\odot]}\right) = -2.54\,(M_{W_1} - M_{W_2}) - 0.17 \tag{4.5}$$

with:

$$L_{W_1}\,[L_\odot] = 10^{-0.4\left(M_{W_1} - 3.24\right)} \tag{4.6}$$

Putting together Equation (4.5) and Equation (4.6), the final relation is:

$$\log_{10}\left(M_*\,[M_\odot]\right) = -2.54\,(M_{W_1} - M_{W_2}) - 0.4\,(M_{W_1} - 3.24) - 0.17 \tag{4.7}$$

The values of the absolute magnitudes measured in WISE were obtained after a crossmatching between our sample of galaxies and the data presented in the Infrared Science Archive. The galaxy IC 10, classified as star-forming galaxy, was not observed in WISE, so it is omitted in our study of the mass-metallicity relation.

Figures 4.13 (a) and (b) show that a bias was introduced during the construction of the sample (the KS-test provides a p-value ≈ 0.015, so both distributions do not follow the same statistics), since

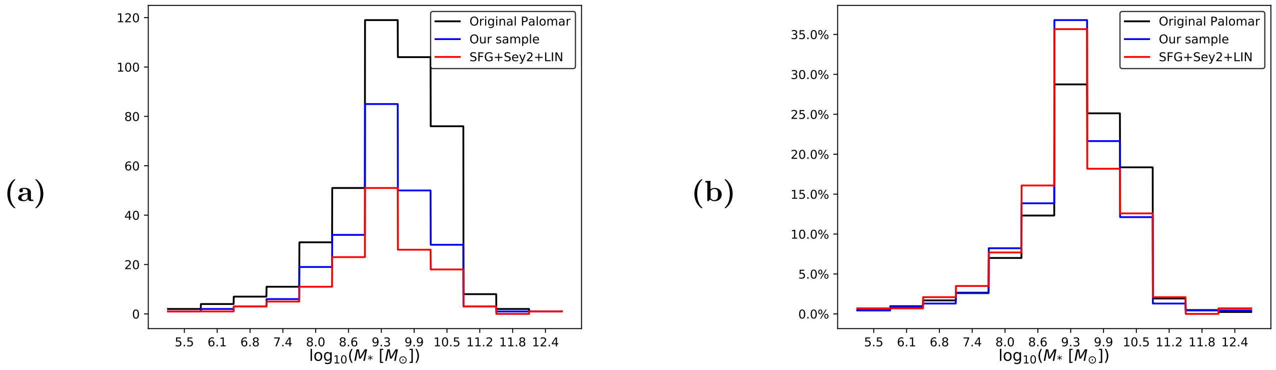

Figure 4.13: Absolute (a) and relative (b) distributions of the stellar masses (M_*). The different colors indicate: black for all the galaxies with nuclear emission in the Palomar Survey (418 objects), blue for the galaxies in our sample (234 objects) and red for the sample composed by star-forming galaxies, Seyferts 2 and LINERs with reliable determinations in their chemical abundances (144 objects).

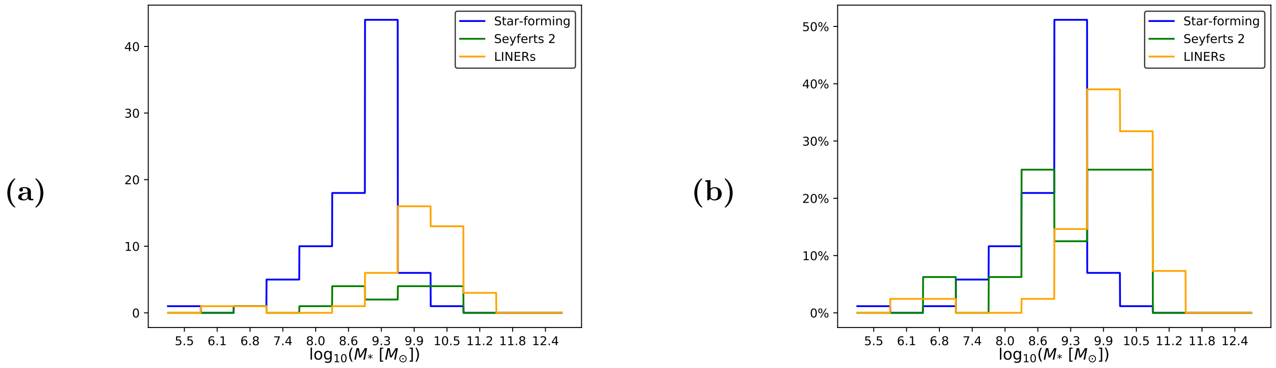

Figure 4.14: Absolute (a) and relative (b) distributions of the stellar masses (M_*) for the different spectral types.

Spectral type	**Number**	**Median**	**Std. Dev.**	**Min.**	**Max.**
Star-forming	86	9.03	0.75	5.39	10.63
Seyferts 2	16	9.65	1.03	6.85	10.81
LINERs	41	10.07	0.91	6.09	11.05

Table 4.8: Statistics of $\log_{10}(M_* \, [M_\odot])$ for each spectral type.

the percentage of galaxies with stellar masses $M_* > 10^{9.6} \, M_\odot$ decreases while the percentage of galaxies with stellar masses in $10^{9.0} - 10^{9.6} \, M_\odot$ increases from the 28% to 38%. Analyzing the distribution for each spectral type (see Figure 4.14 and Table 4.8), star-forming galaxies present a median value of $\log_{10}(M_* \, [M_\odot]) = 9.03 \pm 0.75$, while in Seyferts 2 it is 9.64 ± 1.03 and in LINERs 10.07 ± 0.91. Therefore, at face values, LINERs are hosted by the most massive galaxies ($M_* > 10^{10} \, M_\odot$), followed by Seyferts 2 and star-forming galaxies, which is in good agreement with previous studies on the stellar mass distribution for star-forming galaxies and AGN [Kauffmann et al. (2003); Kewley et al. (2006); Vitale et al. (2013); Thomas et al. (2019)].

Analyzing star-forming galaxies, the chemical abundance $12 + \log_{10}(O/H)$ increases with the stellar mass in the range $10^7 - 10^9\ M_\odot$ (see Figure 4.15 (a)), which is the expected behavior due to the mass-metallicity relation [Contini et al. (2002); Melbourne and Salzer (2002); Lamareille et al. (2004); Tremonti et al. (2004); Erb et al. (2006a); Gao et al. (2018)]. However, while previous studies [Contini et al. (2002); Tremonti et al. (2004); Maiolino and Mannucci (2019)] show that the relation flattens for $M_* > 10^{10}\ M_\odot$, the change in the slope in our study occurs at $M_* \approx 10^9\ M_\odot$. In the case of the chemical abundance ratio $\log_{10}(N/O)$, Figure 4.15 (c) shows that this abundance also scales with the stellar mass, implying that mass-metallicity relation is also presented for $\log_{10}(N/O)$, as previously reported [Pérez-Montero and Contini (2009); Amorín et al. (2010)]. In contrast with the mass-metallicity relation, the ionization parameter $\log_{10}(U)$ presents higher values for galaxies with $M_* \approx 10^7 - 10^8\ M_\odot$, and a constant value ≈ -3.3 for higher stellar masses.

Analyzing Seyferts 2, the chemical abundance $12 + \log_{10}(O/H)$ increases with the stellar mass for 13 out of 16 galaxies. The mass-metallicity relation for this AGN is more flattened than for star-forming galaxies, as already reported by Thomas et al. [2019]. However, three galaxies (18% of Seyferts 2), NGC 660, NGC 3185 and NGC 3646, do not present such a relation (see Figure 4.15 (b)). Due to the small size of the sample, this apparent rupture of the mass-metallicity relation requires a carefully re-examination with a larger sample. The chemical abundance ratio $\log_{10}(N/O)$ and the ionization parameter $\log_{10}(U)$ remain practically constant for all stellar masses (see Figure 4.15 (d) and (f)).

In the case of LINERs, the plot $12+\log_{10}(O/H)$ vs $\log_{10}(M_*)$ shows that there is no relation between both quantities, with a Pearson correlation coefficient $r = -0.043$ (see also Figure 4.15 (b)), and with a high dispersion of values for high stellar masses, $M_* > 10^9\ M_\odot$ that emphasizes this statement. In contrast, the chemical abundance ratio $\log_{10}(N/O)$ shows a saturation for high stellar masses, property that most of their host galaxies verify. However, the lack of objects with stellar masses in $10^7 - 10^9\ M_\odot$ (see Figure 4.15 (d)) does not allow to verify if the stellar mass-metallicity relation presented in star-forming galaxies is also presented for this objects. Finally, the ionization parameter $\log_{10}(U)$ does not show any particular trend ($r = -0.07$) with the stellar mass.

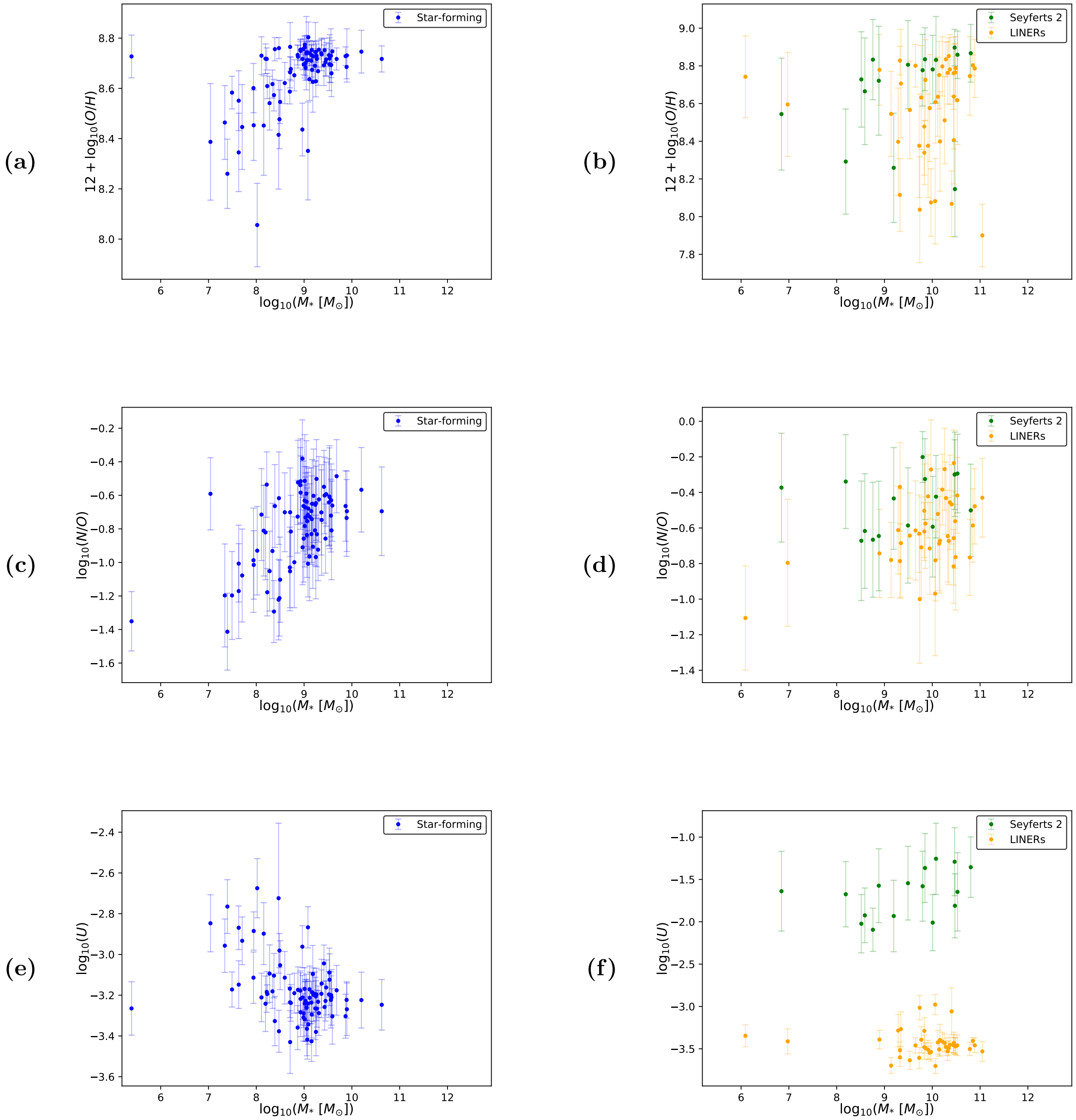

Figure 4.15: Chemical abundances $12+\log_{10}(O/H)$ (a) and (b), $\log_{10}(N/O)$ (c) and (d) and ionization parameter $\log_{10}(U)$ (e) and (f) vs the stellar mass $\log_{10}(M_*\,[M_\odot])$. The left column shows the results for star-forming galaxies and the right column those for AGN (Seyferts 2 and LINERs).

5. Conclusions and future perspectives

5.1 General conclusions

Our study of the well-known Palomar Spectroscopic Survey has revealed that HCm code is a very efficient tool to estimate chemical abundances in a large sample of galaxies. Firstly, this program can be used with a set of strong emission lines that are available for optical spectroscopic surveys. Secondly, it can be applied for both, star-forming galaxies and AGN. And thirdly, it does not assume any underlying relation between the chemical abundance $12 + \log_{10}(O/H)$ and the chemical abundance ratio $\log_{10}(N/O)$.

- **Star-forming galaxies**: The chemical abundance ratios of oxygen to hydrogen present a median value similar to that measured for the Sun, although there is a small group of galaxies with sub-solar abundances. This abundance is related to the chemical abundance ratio of oxygen to nitrogen, demonstrating the existence of two groups of star-forming galaxies. For the first group, the chemical abundance ratio $\log_{10}(N/O)$ is practically constant, behavior explained by the production of carbon and oxygen in massive stars. For the second group, the chemical abundance ratio $\log_{10}(N/O)$ scales with $12 + \log_{10}(O/H)$, explained due to the presence of an enriched ISM. Finally, the ionization parameter $\log_{10}(U)$ shows a strong anti-correlation with the chemical abundance $12 + \log_{10}(O/H)$.
- **Seyferts 2**: The chemical abundance $12 + \log_{10}(O/H)$ shows the highest values in our sample, with a median value slighty higher than that determined for the Sun. The chemical abundance ratio $\log_{10}(N/O)$ does not show any particular trend with $12 + \log_{10}(O/H)$, contrasting with the behavior observed for star-forming galaxies. The ionization parameter $\log_{10}(U)$ seems to be independent from both chemical abundances.
- **LINERs**: The median chemical abundance $12 + \log_{10}(O/H)$ is slightly lower than in Seyferts 2 and star-forming galaxies. A similar situation is also found for the chemical abundance ratio $\log_{10}(N/O)$, but star-forming galaxies show lower values for these parameter. As observed in Seyferts 2, both chemical abundances are independent one from each other and also from the ionization parameter $\log_{10}(U)$.

Although it was needed to reduce the original sample of galaxies to present reliable determinations of the chemical abundances, our study of the host galaxy properties shows that no bias was introduced in almost all the host galaxy properties analyzed, despite the distribution of stellar masses is slightly modified.

The first host galaxy property analyzed is the morphology. From our study, the chemical abundance $12 + \log_{10}(O/H)$ is slightly affected by the morphological type, although for star-forming galaxies there is an important decrease in irregular galaxies. The chemical abundance ratio $\log_{10}(N/O)$ is only affected by the spectral type: being higher in Seyferts 2 than in LINERs or star-forming galaxies, that present similar values. The ionization parameter $\log_{10}(U)$ changes with the morphology only for star-forming galaxies, for AGN practically remains constant.

Our study of the absolute B-magnitude reveals that there is little correlation between this parameter and the chemical abundances in star-forming galaxies. In the case of AGN, they are practically not correlated. A similar behavior is observed in the H_α luminosity. For AGN, the mass of the SMBH does not introduce any change in the chemical abundances, that practically remain constant for Seyferts 2 and show high dispersion for LINERs. For all this properties, the ionization parameter is virtually the same for each spectral type.

The last property analyzed was the stellar mass, which is the property more correlated with the chemical abundances for star-forming galaxies and Seyferts 2. This is the expected behavior from the mass-metallicity relation that was previously observed for both spectral types. However, the chemical abundances in LINERs do not present such a relation with the stellar mass.

The ionization parameter $\log_{10}(U)$ has been probed to be the best tool for distinguishing among star-forming galaxies, Seyferts 2 and LINERs. Our study shows that this parameter is not affected by any host galaxy property, only the spectral type induces significant changes in $\log_{10}(U)$: the ionization parameter is higher for Seyferts 2, followed by star-forming galaxies and then by LINERs.

Our complementary analysis of composite galaxies (see Annex I) shows that the distribution of chemical abundances and their behavior with the different host galaxy properties fits better with the relations observed for star-forming galaxies. In addition, if they are considered as AGN, the chemical abundance $12 + \log_{10}(O/H)$ presents sub-solar values for almost all composites. However, there is still a small group of composite galaxies that can only be considered as AGN.

5.2 Future perspectives

Our analysis of the Palomar Spectroscopic Survey shows that HCm can be used to derivate the chemical abundances and ionization parameter for star-forming galaxies, Seyferts 2 and LINERs. However, the Palomar Survey presents two problems: 1) due to the limited spectral coverage, not all the emission lines that can be used in the code are measured; and, 2) the sample of Seyferts 2 is small. Once the soundness of our methodology is demonstrated with this study, it might be applied to larger samples of galaxies and with better spectral coverage, so as to revisit several results obtained in this study for small samples of galaxies.

In addition, our methodology may be also applied to high spatial resolution spectroscopic data of the NLR in AGN in order to evaluate whether the contribution from other mechanisms is important. In the case of composite galaxies, this high resolution view may provide new insights on how important is the contribution of star formation in the photoionization process, giving rise to their emission lines.

Bibliography

Alloin, D., Collin-Souffrin, S., Joly, M., and Vigroux, L. (1979). Nitrogen and oxygen abundances in galaxies. *A&A*, 78:200–216.

Alloin, D., Johnson, R., and Lira, P. (2006). *Physics of Active Galactic Nuclei at all Scales*, volume 693. Springer.

Almeida, C. R., Garcia, A. M. P., Acosta-Pulido, J. A., Espinosa, J. M. R., Barrena, R., and Manchado, A. (2006). The Narrow-Line Region of the Seyfert 2 galaxy Mrk 78: An Infrared View. *The Astrophysical Journal*, 645(1):148–159.

Amorín, R. O., Pérez-Montero, E., and Vílchez, J. M. (2010). On the Oxygen and Nitrogen Chemical Abundances and the Evolution of the "Green Pea" Galaxies. *The Astrophysical Journal*, 715(2):L128–L132.

Anderson, S. F., Fan, X., Richards, G. T., Schneider, D. P., Strauss, M. A., Berk, D. E. V., Gunn, J. E., Knapp, G. R., Schlegel, D., Voges, W., et al. (2001). High-Redshift Quasars Found in Sloan Digital Sky Survey Commissioning Data. VI. Sloan Digital Sky Survey Spectrograph Observations. *The Astronomical Journal*, 122(2):503.

Andrews, B. H. and Martini, P. (2013). The Mass-Metallicity Relation with the Direct Method on Stacked Spectra of SDSS Galaxies. *The Astrophysical Journal*, 765(2):140.

Antonucci, R. (1993). Unified models for active galactic nuclei and quasars. *Annual Review of Astronomy and Astrophysics*, 31(1):473–521.

Antonucci, R. (2012). A panchromatic review of thermal and nonthermal active galactic nuclei.

Asplund, M., Grevesse, N., Sauval, A. J., and Scott, P. (2009). The Chemical Composition of the Sun. *Annual Review of Astronomy and Astrophysics*, 47(1):481–522.

Baldwin, J. A., Phillips, M. M., and Terlevich, R. (1981). Classification parameters for the emission-line spectra of extragalactic objects. *Astronomical Society of the Pacific*, 93:5–19.

Bennert, N., Jungwiert, B., Komossa, S., Haas, M., and Chini, R. (2006). Size and properties of the narrow-line region in Seyfert-2 galaxies from spatially-resolved optical spectroscopy. *A&A*, 456(3):953–966.

Bian, W. and Gu, Q. (2007). The Eddington Ratios in Seyfert 2 Galaxies with and without Hidden Broad-Line Regions. *The Astrophysical Journal*, 657(1):159–166.

Binette, L. (1985). Photoionization models for Liners: gas distribution abundances. *A&A*, 143:334–346.

Blandford, R., Meier, D., and Readhead, A. (2019). Relativistic Jets from Active Galactic Nuclei. *Annual Review of Astronomy and Astrophysics*, 57(1):467–509.

Burbidge, E. M., Burbidge, G. R., Fowler, W. A., and Hoyle, F. (1957). Synthesis of the Elements in Stars. *Reviews of Modern Physics*, 29(4):547–650.

Burstein, D. and Heiles, C. (1982). Reddenings derived from H I and galaxy counts : accuracy and maps. *The Astronomical Journal*, 87:1165–1189.

Burstein, D. and Heiles, C. (1984). Reddening estimates for galaxies in the second reference catalog and the Uppsala General Catalog. *The Astrophysical Journal Supplement Series*, 54:33–79.

Cao, X. (2009). An accretion disc-corona model for X-ray spectra of active galactic nuclei. *Monthly Notices of the Royal Astronomical Society*, 394(1):207–213.

Cardelli, J. A., Clayton, G. C., and Mathis, J. S. (1989). The Relationship between Infrared, Optical, and Ultraviolet Extinction. *The Astrophysical Journal*, 345:245–256.

Carvalho, S. P., Dors, O. L., Cardaci, M. V., Hägele, G. F., Krabbe, A. C., Pérez-Montero, E., Monteiro, A. F., Armah, M., and Freitas-Lemes, P. (2020). Chemical abundances of Seyfert 2 AGNs – II. N2 metallicity calibration based on SDSS. *Monthly Notices of the Royal Astronomical Society*, 492(4):5675–5683.

Castro, C. S., Dors, O. L., Cardaci, M. V., and Hägele, G. F. (2017). New metallicity calibration for Seyfert 2 galaxies based on the N2O2 index. *Monthly Notices of the Royal Astronomical Society*, 467(2):1507–1514.

Chen, Y.-C. and Hwang, C.-Y. (2017). Morphology of Seyfert galaxies. *Astrophysics and Space Science*, 362(12).

Cid Fernandes, R., Stasińska, G., Mateus, A., and Vale Asari, N. (2011). A comprehensive classification of galaxies in the Sloan Digital Sky Survey: how to tell true from fake AGN? *Monthly Notices of the Royal Astronomical Society*, 413(3):1687–1699.

Cluver, M. E., Jarrett, T. H., Hopkins, A. M., Driver, S. P., Liske, J., Gunawardhana, M. L. P., Taylor, E. N., Robotham, A. S. G., Alpaslan, M., Baldry, I., Brown, M. J. I., Peacock, J. A., Popescu, C. C., Tuffs, R. J., Bauer, A. E., Bland-Hawthorn, J., Colless, M., Holwerda, B. W., Lara-López, M. A., Leschinski, K., López-Sánchez, A. R., Norberg, P., Owers, M. S., Wang, L., and Wilkins, S. M. (2014). Galaxy and Mass Assembly (GAMA): Mid-infrared Properties and Empirical Relations from WISE. *The Astrophysical Journal*, 782(2):90.

Coldwell, G. V., Alonso, S., Duplancic, F., and Mesa, V. (2018). LINER galaxy properties and the local environment. *Monthly Notices of the Royal Astronomical Society*, 476(2):2457–2464.

Comastri, A. (2004). Compton-Thick AGN: The Dark Side of the X-Ray Background. In *Supermassive Black Holes in the Distant Universe*, pages 245–272. Springer.

Contini, T., Treyer, M. A., Sullivan, M., and Ellis, R. S. (2002). Chemical abundances in a UV-selected sample of galaxies. *Monthly Notices of the Royal Astronomical Society*, 330(1):75–91.

Davies, R. L., Kewley, L. J., Ho, I.-T., and Dopita, M. A. (2014a). Starburst–AGN mixing – II. Optically selected active galaxies. *Monthly Notices of the Royal Astronomical Society*, 444(4):3961–3974.

Davies, R. L., Rich, J. A., Kewley, L. J., and Dopita, M. A. (2014b). Starburst–AGN mixing–I. NGC 7130. *Monthly Notices of the Royal Astronomical Society*, 439(4):3835–3846.

de Vaucouleurs, G. (1963). Revised Classification of 1500 Bright Galaxies. *The Astrophysical Journal Supplement*, 8:31.

Della Ceca, R., Pellegrini, S., Bassani, L., Beckmann, V., Cappi, M., Palumbo, G. G. C., Trinchieri, G., and Wolter, A. (2001). Unveiling the AGN powering the “Composite” Seyfert/Star-forming galaxy NGC 7679: BeppoSAX and ASCA results. *A&A*, 375(3):781–790.

Devereux, N. (2017). Photoionization modelling of the giant broad-line region in NGC 3998. *Monthly Notices of the Royal Astronomical Society*, 473(3):2930–2938.

Dopita, M., Koratkar, A., Evans, I., Allen, M., Bicknell, G., Sutherland, R., Hawley, J., and Sadler, E. (1996). Shock excitation of liners. In *The Physics of Liners in View of Recent Observations*, volume 103, page 44.

Dopita, M. A., Kewley, L. J., Heisler, C. A., and Sutherland, R. S. (2000). A Theoretical Recalibration of the Extragalactic HII Region Sequence. *The Astrophysical Journal*, 542(1):224–234.

Dors, O. L., J., Cardaci, M. V., Hägele, G. F., Rodrigues, I., Grebel, E. K., Pilyugin, L. S., Freitas-Lemes, P., and Krabbe, A. C. (2015). On the central abundances of active galactic nuclei and star-forming galaxies. *Monthly Notices of the Royal Astronomical Society*, 453(4):4102–4111.

Dors, O. L., Freitas-Lemes, P., Amôres, E. B., Pérez-Montero, E., Cardaci, M. V., Hägele, G. F., Armah, M., Krabbe, A. C., and Faúndez-Abans, M. (2019). Chemical abundances of Seyfert 2 AGNs – I. Comparing oxygen abundances from distinct methods using SDSS. *Monthly Notices of the Royal Astronomical Society*, 492(1):468–479.

Ellison, S. L., Patton, D. R., Simard, L., and McConnachie, A. W. (2007). Clues to the Origin of the Mass-Metallicity Relation: Dependence on Star Formation Rate and Galaxy Size. *The Astrophysical Journal*, 672(2):L107–L110.

Erb, D. K., Shapley, A. E., Pettini, M., Steidel, C. C., Reddy, N. A., and Adelberger, K. L. (2006a). The Mass-Metallicity Relation at z$\gtrsim$2. *The Astrophysical Journal*, 644(2):813–828.

Erb, D. K., Steidel, C. C., Shapley, A. E., Pettini, M., Reddy, N. A., and Adelberger, K. L. (2006b). The Stellar, Gas, and Dynamical Masses of Star-forming Galaxies at z$\sim$ 2. *The Astrophysical Journal*, 646(1):107–132.

Ferland, G. J. and Netzer, H. (1983). Are there any shock-heated galaxies ? *The Astrophysical Journal*, 264:105–113.

Ferland, G. J., Porter, R. L., van Hoof, P. A. M., Williams, R. J. R., Abel, N. P., Lykins, M. L., Shaw, G., Henney, W. J., and Stancil, P. C. (2013). The 2013 Release of Cloudy. *Revista Mexicana de Astronomía y Astrofísica*, 49:137–163.

Filho, M. E., Barthel, P. D., and Ho, L. C. (2000). The Nature of Composite LINER/H II Galaxies as Revealed from High-Resolution VLA Observations. *The Astrophysical Journal Supplement Series*, 129(1):93–110.

Galama, T. J., Vreeswijk, P. M., van Paradijs, J., Kouveliotou, C., Augusteijn, T., Böhnhardt, H., Brewer, J. P., Doublier, V., Gonzalez, J. F., Leibundgut, B., Lidman, C., Hainaut, O. R., Patat, F., Heise, J., in't Zand, J., Hurley, K., Groot, P. J., Strom, R. G., Mazzali, P. A., Iwamoto, K., Nomoto, K., Umeda, H., Nakamura, T., Young, T. R., Suzuki, T., Shigeyama, T., Koshut, T., Kippen, M., Robinson, C., de Wildt, P., Wijers, R. A. M. J., Tanvir, N., Greiner, J., Pian, E., Palazzi, E., Frontera, F., Masetti, N., Nicastro, L., Feroci, M., Costa, E., Piro, L., Peterson, B. A., Tinney, C., Boyle, B., Cannon, R., Stathakis, R., Sadler, E., Begam, M. C., and Ianna, P. (1998). An unusual supernova in the error box of the γ-ray burst of 25 April 1998. *Nature*, 395(6703):670–672.

Gao, Y., Bao, M., Yuan, Q., Kong, X., Zou, H., Zhou, X., Gu, Y., Lin, Z., Liang, Z., and Huang, C. (2018). Mass-Metallicity Relation and Fundamental Metallicity Relation of Metal-poor Star-forming Galaxies at $0.6 < z < 0.9$ from the eBOSS Survey. *The Astrophysical Journal*, 869(1):15.

Giacconi, R., Gursky, H., Paolini, F. R., and Rossi, B. B. (1962). Evidence for X-Rays From Sources Outside the Solar System. *Phys. Rev. Lett.*, 9:439–443.

Gliozzi, M., Foschini, L., Sambruna, R. M., and Tavecchio, F. (2008). The polyhedral nature of LINERs: an XMM-Newton view of LINERs in radio galaxies. *A&A*, 478(3):723–737.

González Delgado, R. M., Pérez, E., Cid Fernandes, R., García-Benito, R., López Fernández, R., Vale Asari, N., Cortijo-Ferrero, C., de Amorim, A. L., Lacerda, E. A. D., Sánchez, S. F., Lehnert, M. D., and Walcher, C. J. (2017). Spatially-resolved star formation histories of CALIFA galaxies. Implications for galaxy formation. *A&A*, 607:A128.

González-Martín, O., Masegosa, J., Márquez, I., and Guainazzi, M. (2009). Fitting LINER nuclei within the AGN family: A matter of obscuration? *The Astrophysical Journal*, 704(2):1570–1585.

Greene, J. E. and Ho, L. C. (2005). Estimating Black Hole Masses in Active Galaxies Using the H_α Emission Line. *The Astrophysical Journal*, 630(1):122–129.

Greene, J. E., Strader, J., and Ho, L. C. (2019). Intermediate-Mass Black Holes.

Groves, B. (2006). The Narrow Line Region: Current Models and Future Questions. *arXiv preprint astro-ph/0612309.*

Guglielmo, V., Poggianti, B. M., Moretti, A., Fritz, J., Calvi, R., Vulcani, B., Fasano, G., and Paccagnella, A. (2015). The star formation history of galaxies: the role of galaxy mass, morphology and environment. *Monthly Notices of the Royal Astronomical Society*, 450(3):2749–2763.

Halpern, J. P. and Steiner, J. E. (1983). Low ionization active galactic nuclei : X-ray or shock heated ? *The Astrophysical Journal Letters*, 269:L37–L41.

Hawkins, M. R. S. (2007). Timescale of variation and the size of the accretion disc in active galactic nuclei. *A&A*, 462(2):581–589.

Heckman, T. M. and Best, P. N. (2014). The coevolution of galaxies and supermassive black holes: Insights from surveys of the contemporary universe. *Annual Review of Astronomy and Astrophysics*, 52(1):589–660.

Hewish, A., Bell, S. J., Pilkington, J. D. H., Scott, P. F., and Collins, R. A. (1968). Observation of a Rapidly Pulsating Radio Source. *Nature*, 217(5130):709–713.

Hilborn, R. C. (1982). Einstein coefficients, cross sections, f values, dipole moments, and all that. *American Journal of Physics*, 50(11):982–986.

Ho, L. C. (2004). *Coevolution of Black Holes and Galaxies: Volume 1, Carnegie Observatories Astrophysics Series*, volume 1. Cambridge University Press.

Ho, L. C., Filippenko, A. V., and Sargent, W. L. (1995). A Search for “Dwarf” Seyfert Nuclei. II. An Optical Spectral Atlas of the Nuclei of Nearby Galaxies. *The Astrophysical Journal Supplement Series*, 98:477.

Ho, L. C., Filippenko, A. V., and Sargent, W. L. W. (1997a). A Search for “Dwarf” Seyfert Nuclei. III. Spectroscopic Parameters and Properties of the Host Galaxies. *The Astrophysical Journal Supplement Series*, 112(2):315–390.

Ho, L. C., Filippenko, A. V., and Sargent, W. L. W. (1997b). A Search for “Dwarf” Seyfert Nuclei. V. Demographics of Nuclear Activity in Nearby Galaxies. *The Astrophysical Journal*, 487(2):568–578.

Ho, L. C., Filippenko, A. V., and Sargent, W. L. W. (2003). A Search for “Dwarf” Seyfert Nuclei. VI. Properties of Emission-Line Nuclei in Nearby Galaxies. *The Astrophysical Journal*, 583(1):159–177.

Ho, L. C., Filippenko, A. V., Sargent, W. L. W., and Peng, C. Y. (1997c). A Search for “Dwarf” Seyfert Nuclei. IV. Nuclei with Broad Hα Emission. *The Astrophysical Journal Supplement Series*, 112(2):391–414.

Ho, L. C., Greene, J. E., Filippenko, A. V., and Sargent, W. L. W. (2009). A Search for “Dwarf” Seyfert Nuclei. VII. A catalog of central stellar velocity dispersions of nearby galaxies. *The Astrophysical Journal Supplement Series*, 183(1):1–16.

Ho, L. C., Shields, J. C., and Filippenko, A. V. (1993). The Ionizing Radiation of Seyfert 2 Galactic Nuclei. *The Astrophysical Journal*, 410:567.

Howarth, I. D. (1983). LMC and galactic extinction. *Monthly Notices of the Royal Astronomical Society*, 203(2):301–304.

Imanishi, M., Ichikawa, K., Takeuchi, T., Kawakatu, N., Oi, N., and Imase, K. (2011). Infrared 3–4 μm Spectroscopy of Nearby PG QSOs and AGN–Nuclear Starburst Connections in High-Luminosity AGN Populations. *Publications of the Astronomical Society of Japan*, 63(sp2):S447–S456.

Izotov, Y. I., Guseva, N. G., Fricke, K. J., and Henkel, C. (2015). On the universality of luminosity–metallicity and mass–metallicity relations for compact star-forming galaxies at redshifts $0 < z < 3$. *Monthly Notices of the Royal Astronomical Society*, 451(3):2251–2262.

Johnson, H. L. and Morgan, W. W. (1953). Fundamental stellar photometry for standards of spectral type on the Revised System of the Yerkes Spectral Atlas. *The Astrophysical Journal*, 117:313.

Kauffmann, G., Heckman, T. M., Tremonti, C., Brinchmann, J., Charlot, S., White, S. D. M., Ridgway, S. E., Brinkmann, J., Fukugita, M., Hall, P. B., Ivezic, Z., Richards, G. T., and Schneider, D. P. (2003). The host galaxies of active galactic nuclei. *Monthly Notices of the Royal Astronomical Society*, 346(4):1055–1077.

Kennicutt, R. C. (1998). Star Formation in Galaxies Along the Hubble Sequence. *Annual Review of Astronomy and Astrophysics*, 36(1):189–231.

Kennicutt, R. C., Hao, C.-N., Calzetti, D., Moustakas, J., Dale, D. A., Bendo, G., Engelbracht, C. W., Johnson, B. D., and Lee, J. C. (2009). Dust-corrected Star Formation Rates of Galaxies. I. Combinations of H_α and Infrared Tracers. *The Astrophysical Journal*, 703(2):1672–1695.

Kewley, L. J. and Dopita, M. A. (2002). Using Strong Lines to Estimate Abundances in Extragalactic H II Regions and Starburst Galaxies. *The Astrophysical Journal Supplement Series*, 142(1):35–52.

Kewley, L. J., Groves, B., Kauffmann, G., and Heckman, T. (2006). The host galaxies and classification of active galactic nuclei. *Monthly Notices of the Royal Astronomical Society*, 372(3):961–976.

Kewley, L. J., Nicholls, D. C., and Sutherland, R. S. (2019). Understanding Galaxy Evolution Through Emission Lines. *Annual Review of Astronomy and Astrophysics*, 57(1):511–570.

Kim, S.-H., Martin, P. G., and Hendry, P. D. (1994). The Size Distribution of Interstellar Dust Particles as Determined from Extinction. *The Astrophysical Journal*, 422:164.

Kinman, T. D. and Davidson, K. (1981). Spectroscopic observations of 10 emission-line dwarf galaxies. *The Astrophysical Journal*, 243:127–139.

Kobulnicky, H. A., Kennicutt, Robert C., J., and Pizagno, J. L. (1999). On Measuring Nebular Chemical Abundances in Distant Galaxies Using Global Emission-Line Spectra. *The Astrophysical Journal*, 514(2):544–557.

Kojima, T., Ouchi, M., Nakajima, K., Shibuya, T., Harikane, Y., and Ono, Y. (2017). Evolution of N/O abundance ratios and ionization parameters from z $\sim$ 0 to 2 investigated by the direct temperature method. *Publications of the Astronomical Society of Japan*, 69(3). 44.

Kolb, E. W. and Turner, M. S. (1990). The Early Universe. *Front. Phys.*, 69:1–547.

Kolmogorov-Smirnov, A., Kolmogorov, A., and Kolmogorov, M. (1933). Sulla determinazione empírica di uma legge di distribuzione.

Koulouridis, E., Plionis, M., Chavushyan, V., Dultzin-Hacyan, D., Krongold, Y., and Goudis, C. (2006). Local and Large-Scale Environment of Seyfert Galaxies. *The Astrophysical Journal*, 639(1):37–45.

Lamareille, F., Mouhcine, M., Contini, T., Lewis, I., and Maddox, S. (2004). The luminosity–metallicity relation in the local Universe from the 2dF Galaxy Redshift Survey. *Monthly Notices of the Royal Astronomical Society*, 350(2):396–406.

Lequeux, J., Peimbert, M., Rayo, J. F., Serrano, A., and Torres-Peimbert, S. (1979). Reprint of 1979A&A....80..155L. Chemical composition and evolution of irregular and blue compact galaxies. *A&A*, 500:145–156.

Lira, P., Johnson, R. A., Lawrence, A., and Cid Fernandes, R. (2007). Multiwavelength study of the nuclei of a volume-limited sample of galaxies – II. Optical, infrared and radio observations. *Monthly Notices of the Royal Astronomical Society*, 382(4):1552–1590.

Liu, H.-Y., Yuan, W., Dong, X.-B., Zhou, H., and Liu, W.-J. (2018). A Uniformly Selected Sample of Low-mass Black Holes in Seyfert 1 Galaxies. II. the SDSS DR7 Sample. *The Astrophysical Journal Supplement Series*, 235(2):40.

Ma, X., Hopkins, P. F., Faucher-Giguère, C.-A., Zolman, N., Muratov, A. L., Kereš, D., and Quataert, E. (2015). The origin and evolution of the galaxy mass–metallicity relation. *Monthly Notices of the Royal Astronomical Society*, 456(2):2140–2156.

Maddox, N. (2018). [OII] as a proxy for star formation in AGN host galaxies: beware of extended emission line regions. *Monthly Notices of the Royal Astronomical Society*, 480(4):5203–5210.

Maiolino, R. and Mannucci, F. (2019). De re metallica: the cosmic chemical evolution of galaxies. *The Astronomy and Astrophysics Review*, 27(1):3.

Matsuoka, K., Nagao, T., Maiolino, R., Marconi, A., and Taniguchi, Y. (2009). Chemical evolution of high-redshift radio galaxies. *A&A*, 503(3):721–730.

Matsuoka, K., Nagao, T., Marconi, A., Maiolino, R., Mannucci, F., Cresci, G., Terao, K., and Ikeda, H. (2018). The mass-metallicity relation of high-z type-2 active galactic nuclei. *A&A*, 616:L4.

Melbourne, J. and Salzer, J. J. (2002). Metal Abundances of KISS Galaxies. I. Coarse Metal Abundances and the Metallicity-Luminosity Relation. *The Astronomical Journal*, 123(5):2302–2311.

Meyer-Hofmeister, E., Liu, B. F., and Qiao, E. (2017). Interaction of the accretion flows in corona and disk near the black hole in active galactic nuclei. *A&A*, 607:A94.

Miller, B. P., Brandt, W. N., Schneider, D. P., Gibson, R. R., Steffen, A. T., and Wu, J. (2010). X-ray Emission from Optically Selected Radio-intermediate and Radio-loud Quasars. *The Astrophysical Journal*, 726(1):20.

Mollá, M., García-Vargas, M. L., and Bressan, A. (2009). PopStar I: evolutionary synthesis model description. *Monthly Notices of the Royal Astronomical Society*, 398(1):451–470.

Mor, R., Netzer, H., and Elitzur, M. (2009). Dusty Structure Around Type-I Active Galactic Nuclei: Clumpy Torus Narrow Line Region and Near-Nucleus Hot Dust. *The Astrophysical Journal*, 705(1):298–313.

Moustakas, J., Kennicutt, R. C., Tremonti, C. A., Dale, D. A., Smith, J.-D. T., and Calzetti, D. (2010). Optical Spectroscopy and Nebular Oxygen Abundances of the Spitzer/SINGS Galaxies. *The Astrophysical Journal Supplement Series*, 190(2):233–266.

Márquez, I., Masegosa, J., González-Martin, O., Hernández-Garcia, L., Pović, M., Netzer, H., Cazzoli, S., and del Olmo, A. (2017). The AGN Nature of LINER Nuclear Sources. *Frontiers in Astronomy and Space Sciences*, 4:34.

Nagao, T., Maiolino, R., and Marconi, A. (2006). Gas metallicity in the narrow-line regions of high-redshift active galactic nuclei. *A&A*, 447(3):863–876.

Netzer, H. (2013). *The Physics and Evolution of Active Galactic Nuclei*. Cambridge University Press.

Netzer, H. (2015). Revisiting the Unified Model of Active Galactic Nuclei. *Annual Review of Astronomy and Astrophysics*, 53(1):365–408.

Nisbet, D. M. and Best, P. N. (2015). The mass fraction of AGN and the Fundamental Plane of black hole activity from a large X-ray-selected sample of LINERs. *Monthly Notices of the Royal Astronomical Society*, 455(3):2551–2566.

Osterbrock, D. E. (1977). Spectrophotometry of Seyfert 1 galaxies. *The Astrophysical Journal*, 215:733–745.

Osterbrock, D. E. (1981). Seyfert galaxies with weak broad H alpha emission lines. *The Astrophysical Journal*, 249:462–470.

Osterbrock, D. E. and Ferland, G. J. (2006). *Astrophysics of gaseous nebulae and active galactic nuclei*. Sausalito, Calif. : University Science Books.

Padovani, P., Alexander, D. M., Assef, R. J., De Marco, B., Giommi, P., Hickox, R. C., Richards, G. T., Smolcic, V., Hatziminaoglou, E., Mainieri, V., and et al. (2017). Active galactic nuclei: what's in a name? *The Astronomy and Astrophysics Review*, 25(1).

Pagel, B. E. J., Edmunds, M. G., Blackwell, D. E., Chun, M. S., and Smith, G. (1979). On the composition of H II regions in southern galaxies – I. NGC 300 and 1365. *Monthly Notices of the Royal Astronomical Society*, 189(1):95–113.

Panessa, F., Bassani, L., Cappi, M., Dadina, M., Barcons, X., Carrera, F. J., Ho, L. C., and Iwasawa, K. (2006). On the X-ray, optical emission line and black hole mass properties of local Seyfert galaxies. *A&A*, 455(1):173–185.

Panessa, F., Wolter, A., Pellegrini, S., Fruscione, A., Bassani, L., Ceca, R. D., Palumbo, G. G. C., and Trinchieri, G. (2005). The Nature of Composite Seyfert/Star-forming Galaxies Revealed by X-Ray Observations. *The Astrophysical Journal*, 631(2):707–719.

Pérez-Montero, E. (2014). Deriving model-based T_*e*-consistent chemical abundances in ionized gaseous nebulae. *Monthly Notices of the Royal Astronomical Society*, 441(3):2663–2675.

Pérez-Montero, E. (2015). HII-CHI-mistry: A new model-based method to derive chemical abundances consistent with the direct method. In *Highlights of Spanish Astrophysics VIII*, pages 286–291.

Pérez-Montero, E. and Contini, T. (2009). The impact of the nitrogen-to-oxygen ratio on ionized nebula diagnostics based on [NII] emission lines. *Monthly Notices of the Royal Astronomical Society*, 398(2):949–960.

Pérez-Montero, E., Contini, T., Lamareille, F., Maier, C., Carollo, C. M., Kneib, J.-P., Le Fèvre, O., Lilly, S., Mainieri, V., Renzini, A., Scodeggio, M., Zamorani, G., Bardelli, S., Bolzonella, M., Bongiorno, A., Caputi, K., Cucciati, O., de la Torre, S., de Ravel, L., Franzetti, P., Garilli, B., Iovino, A., Kampczyk, P., Knobel, C., Kovac, K., Le Borgne, J.-F., Le Brun, V., Mignoli, M., Pellò, R., Peng, Y., Presotto, V., Ricciardelli, E., Silverman, J. D., Tanaka, M., Tasca, L. A. M., Tresse, L., Vergani, D., and Zucca, E. (2013). The cosmic evolution of oxygen and nitrogen abundances in star-forming galaxies over the past 10 Gyr. *A&A*, 549:A25.

Pérez-Montero, E., Dors, O L, J., Vílchez, J. M., García-Benito, R., Cardaci, M. V., and Hägele, G. F. (2019). A bayesian-like approach to derive chemical abundances in type-2 active galactic nuclei based on photoionization models. *Monthly Notices of the Royal Astronomical Society*, 489(2):2652–2668.

Peterson, B. M. (2001). Variability of Active Galactic Nuclei. *Advanced Lectures on the Starburst-AGN Connection*, page 3–68.

Pilyugin, L. S., Vílchez, J. M., and Contini, T. (2004). Oxygen and nitrogen abundances in nearby galaxies. Correlations between oxygen abundance and macroscopic properties. *A&A*, 425(3):849–869.

Reis, R. C. and Miller, J. M. (2013). On the Size and Location of the X-Ray Emitting Coronae around Black Holes. *The Astrophysical Journal Letters*, 769(1):L7.

Romero, G. E., Boettcher, M., Markoff, S., and Tavecchio, F. (2017). Relativistic Jets in Active Galactic Nuclei and Microquasars. *Space Science Reviews*, 207(1-4):5–61.

Salim, S., Lee, J. C., Ly, C., Brinchmann, J., Davé, R., Dickinson, M., Salzer, J. J., and Charlot, S. (2014). A Critical Look at the Mass-Metallicity-Star Formation Rate Relation in the Local Universe. I. An Improved Analysis Framework and Confounding Systematics. *The Astrophysical Journal*, 797(2):126.

Sánchez, S. F., Rosales-Ortega, F. F., Jungwiert, B., Iglesias-Páramo, J., Vílchez, J. M., Marino, R. A., Walcher, C. J., Husemann, B., Mast, D., Monreal-Ibero, A., Cid Fernandes, R., Pérez, E., González Delgado, R., García-Benito, R., Galbany, L., van de Ven, G., Jahnke, K., Flores, H., Bland-Hawthorn, J., López-Sánchez, A. R., Stanishev, V., Miralles-Caballero, D., Díaz, A. I., Sánchez-Blazquez, P., Mollá, M., Gallazzi, A., Papaderos, P., Gomes, J. M., Gruel, N., Pérez, I., Ruiz-Lara, T., Florido, E., de Lorenzo-Cáceres, A., Mendez-Abreu, J., Kehrig, C., Roth, M. M., Ziegler, B., Alves, J., Wisotzki, L., Kupko, D., Quirrenbach, A., Bomans, D., and The CALIFA collaboration (2013). Mass-metallicity relation explored with CALIFA. I. Is there a dependence on the star-formation rate? *A&A*, 554:A58.

Schiminovich, D., Wyder, T. K., Martin, D. C., Johnson, B. D., Salim, S., Seibert, M., Treyer, M. A., Budavari, T., Hoopes, C., Zamojski, M., Barlow, T. A., Forster, K. G., Friedman, P. G., Morrissey, P., Neff, S. G., Small, T. A., Bianchi, L., Donas, J., Heckman, T. M., Lee, Y.-W., Madore, B. F., Milliard, B., Rich, R. M., Szalay, A. S., Welsh, B. Y., and Yi, S. (2007). The UV-Optical Color Magnitude Diagram. II. Physical Properties and Morphological Evolution On and Off of a Star-forming Sequence. *The Astrophysical Journal Supplement Series*, 173(2):315–341.

Schmidt, M. (1963). 3C 273: A Star-Like Object with Large Red-Shift. *Nature*, 197(4872):1040–1040.

Seaton, M. J. (1979). Interstellar extinction in the UV. *Monthly Notices of the Royal Astronomical Society*, 187(1):73P–76P.

Shao, L. (2013). *The nature of AGN-host co-evolution*. PhD thesis, lmu.

Shuder, J. M. (1981). Emission-line-continuum correlations in active galactic nuclei. *The Astrophysical Journal*, 244:12–18.

Slavcheva-Mihova, L. and Mihov, B. (2011). Optical multiband surface photometry of a sample of Seyfert galaxies. I. Large-scale morphology and local environment analysis of matched Seyfert and inactive galaxy samples. *A&A*, 526:A43.

Smith, L. J., Westmoquette, M. S., Gallagher, J. S., O'Connell, R. W., Rosario, D. J., and De Grijs, R. (2006). HST/STIS optical spectroscopy of five super star clusters in the starburst galaxy M82. *Monthly Notices of the Royal Astronomical Society*, 370(1):513–527.

Sparke, L. S. and Gallagher III, J. S. (2007). *Galaxies in the Universe: An introduction*. Cambridge University Press.

Stasińska, G., Asari, N. V., Fernandes, R. C., Gomes, J. M., Schlickmann, M., Mateus, A., Schoenell, W., Sodré, L., J., and (the SEAGal collaboration) (2008). Can retired galaxies mimic active galaxies? Clues from the Sloan Digital Sky Survey. *Monthly Notices of the Royal Astronomical Society: Letters*, 391(1):L29–L33.

Storchi-Bergmann, T., Schmitt, H. R., Calzetti, D., and Kinney, A. L. (1998). Chemical Abundance Calibrations for the Narrow-Line Region of Active Galaxies. *The Astronomical Journal*, 115(3):909–914.

Strom, A. L., Steidel, C. C., Rudie, G. C., Trainor, R. F., and Pettini, M. (2018). Measuring the Physical Conditions in High-redshift Star-forming Galaxies: Insights from KBSS-MOSFIRE. *The Astrophysical Journal*, 868(2):117.

Tanaka, Y., Nandra, K., Fabian, A. C., Inoue, H., Otani, C., Dotani, T., Hayashida, K., Iwasawa, K., Kii, T., Kunieda, H., Makino, F., and Matsuoka, M. (1995). Gravitationally redshifted emission implying an accretion disk and massive black hole in the active galaxy MCG-6-30-15. *Nature*, 375(6533):659–661.

Tang, B.-T., Gu, Q.-S., and Huang, S. (2009). Stellar ages and metallicities of nearby elliptical galaxies. *Research in Astronomy and Astrophysics*, 9(11):1215–1229.

The GRAVITY Collaboration, Abuter, R., Amorim, A., Bauböck, M., Berger, J. P., Bonnet, H., Brandner, W., Clénet, Y., Coudé du Foresto, V., de Zeeuw, P. T., Dexter, J., Duvert, G., Eckart, A., Eisenhauer, F., Förster Schreiber, N. M., Garcia, P., Gao, F., Gendron, E., Genzel, R., Gerhard, O., Gillessen, S., Habibi, M., Haubois, X., Henning, T., Hippler, S., Horrobin, M., Jiménez-Rosales, A., Jocou, L., Kervella, P., Lacour, S., Lapeyrère, V., Le Bouquin, J.-B., Léna, P., Ott, T., Paumard, T., Perraut, K., Perrin, G., Pfuhl, O., Rabien, S., Rodriguez Coira, G., Rousset, G., Scheithauer, S., Sternberg, A., Straub, O., Straubmeier, C., Sturm, E., Tacconi, L. J., Vincent, F., von Fellenberg, S., Waisberg, I., Widmann, F., Wieprecht, E., Wiezorrek, E., Woillez, J., and Yazici, S. (2019). A geometric distance measurement to the Galactic center black hole with 0.3% uncertainty. *A&A*, 625:L10.

Thomas, A. D., Kewley, L. J., Dopita, M. A., Groves, B. A., Hopkins, A. M., and Sutherland, R. S. (2019). The Mass–Metallicity Relation of Local Active Galaxies. *The Astrophysical Journal*, 874(1):100.

Torrey, P., Vogelsberger, M., Marinacci, F., Pakmor, R., Springel, V., Nelson, D., Naiman, J., Pillepich, A., Genel, S., Weinberger, R., and Hernquist, L. (2019). The evolution of the mass–metallicity relation and its scatter in IllustrisTNG. *Monthly Notices of the Royal Astronomical Society*, 484(4):5587–5607.

Tremonti, C. A., Heckman, T. M., Kauffmann, G., Brinchmann, J., Charlot, S., White, S. D. M., Seibert, M., Peng, E. W., Schlegel, D. J., Uomoto, A., Fukugita, M., and Brinkmann, J. (2004). The Origin of the Mass-Metallicity Relation: Insights from 53,000 Star-forming Galaxies in the Sloan Digital Sky Survey. *The Astrophysical Journal*, 613(2):898–913.

Tresse, L. and Maddox, S. J. (1998). The H_α Luminosity Function and Star Formation Rate at z$\sim$ 0.2. *The Astrophysical Journal*, 495(2):691–697.

Tully, R. B. (1988). *Nearby Galaxies Catalog.* Cambridge University Press.

Urry, C. M. and Padovani, P. (1995). Unified Schemes for Radio-Loud Active Galactic Nuclei. *Publications of the Astronomical Society of the Pacific*, 107:803.

Vagnetti, F., Antonucci, M., and Trevese, D. (2013). Variability and the X-ray/UV ratio of active galactic nuclei. II. Analysis of a low-redshift Swift sample. *A&A*, 550:A71.

Van den Bergh, S. (1968). The Galaxies of the Local Group. *Journal of the Royal Astronomical Society of Canada*, 62:219.

Vaona, L., Ciroi, S., Di Mille, F., Cracco, V., La Mura, G., and Rafanelli, P. (2012). Spectral properties of the narrow-line region in Seyfert galaxies selected from the SDSS-DR7. *Monthly Notices of the Royal Astronomical Society*, 427(2):1266–1283.

Veilleux, S. and Osterbrock, D. E. (1987). Spectral Classification of Emission-Line Galaxies. *The Astrophysical Journal Supplement Series*, 63:295.

Vila-Costas, M. B. and Edmunds, M. G. (1993). The nitrogen-to-oxygen ratio in galaxies and its implications for the origin of nitrogen. *Monthly Notices of the Royal Astronomical Society*, 265(1):199–212.

Vincenzo, F., Belfiore, F., Maiolino, R., Matteucci, F., and Ventura, P. (2016). Nitrogen and oxygen abundances in the Local Universe. *Monthly Notices of the Royal Astronomical Society*, 458(4):3466–3477.

Vincenzo, F., Matteucci, F., Belfiore, F., and Maiolino, R. (2015). Modern yields per stellar generation: the effect of the IMF. *Monthly Notices of the Royal Astronomical Society*, 455(4):4183–4190.

Vitale, M., Mignoli, M., Cimatti, A., Lilly, S. J., Carollo, C. M., Contini, T., Kneib, J.-P., Le Fevre, O., Mainieri, V., Renzini, A., Scodeggio, M., Zamorani, G., Bardelli, S., Barnes, L., Bolzonella, M., Bongiorno, A., Bordoloi, R., Bschorr, T. J., Cappi, A., Caputi, K., Coppa, G., Cucciati, O., de la Torre, S., de Ravel, L., Franzetti, P., Garilli, B., Iovino, A., Kampczyk, P., Knobel, C., Koekemoer, A. M., Kovac, K., Lamareille, F., Le Borgne, J.-F., Le Brun, V., López-Sanjuan, C., Maier, C., McCracken, H. J., Moresco, M., Nair, P., Oesch, P. A., Pello, R., Peng, Y., Pérez Montero, E., Pozzetti, L., Presotto, V., Silverman, J., Tanaka, M., Tasca, L., Tresse, L., Vergani, D., Welikala, N., and Zucca, E. (2013). Investigating the relationship between AGN activity and stellar mass in zCOSMOS galaxies at $0<z<1$ using emission-line diagnostic diagrams. *A&A*, 556:A11.

Woo, J.-H. and Urry, C. M. (2002). Active Galactic Nucleus Black Hole Masses and Bolometric Luminosities. *The Astrophysical Journal*, 579(2):530–544.

Yates, R. M., Kauffmann, G., and Guo, Q. (2012). The relation between metallicity, stellar mass and star formation in galaxies: an analysis of observational and model data. *Monthly Notices of the Royal Astronomical Society*, 422(1):215–231.

Yeh, S. C. C. and Matzner, C. D. (2012). Ionization Parameter as a Diagnostic of Radiation and Wind Pressures in HII Regions and Starburst Galaxies. *The Astrophysical Journal*, 757(2):108.

Annex I: Analysis of composite galaxies

The nature of composite galaxies is still an open question in the study of AGN and star-forming galaxies, since they are considered to be a mixture between both spectral classes (see section 1.3 for more details). Consequently, there is no criterion to determine which SED (star-forming or AGN) must be selected for these galaxies. In order to avoid any kind of bias in our study, the chemical abundances and ionization parameters of composite galaxies are calculated with both SEDs: the results obtained for composite galaxies as star-forming galaxies are denoted hereinafter as *composites treated as SFG* (for simplicity) while those obtained considering composite galaxies as AGN are denoted hereinafter as *composites treated as AGN*. The results for these galaxies are shown here.

A.1 Chemical abundances

In the case of composite galaxies, there are two results for the two models considered (star-formation or AGN activity). By following the criterion shown in Equation (3.2), some of the composite galaxies only present reliable results under one model. Those galaxies and their derived parameters are presented in Table A.1 (treated as SFG) and in Table A.2 (treated as AGN).

Name	$12 + \log_{10}(O/H)$	$\log_{10}(N/O)$	$\log_{10}(U)$
NGC 63	7.57 ± 0.18	-0.77 ± 0.33	-2.55 ± 0.20
NGC 697	8.62 ± 0.08	-0.54 ± 0.25	-3.08 ± 0.13
NGC 2268	7.70 ± 0.24	-0.64 ± 0.26	-2.75 ± 0.26
NGC 3367	7.83 ± 0.29	-0.96 ± 0.36	-2.87 ± 0.15
NGC 4123	7.699 ± 0.29	-0.91 ± 0.34	-2.67 ± 0.19
NGC 5806	8.62 ± 0.06	-0.69 ± 0.31	-3.17 ± 0.12
NGC 7798	8.67 ± 0.05	-0.53 ± 0.21	-3.246 ± 0.08

Table A.1: Chemical abundances of composite galaxies that only present reliable results considering the star-formation model.

Considering the remaining composite galaxies (33 objects in total), only two of them (namely NGC 2782 and NGC 6500) present compatible results under both models, i.e., they are not affected by the SED. The remaining composite galaxies show a considerable discrepancy between both models as a consequence of the determination of $12 + \log_{10}(O/H)$. This result can be seen in the histogram of O/H in Figure A.1.

Name	$12+\log_{10}(O/H)$	$\log_{10}(N/O)$	$\log_{10}(U)$
NGC 2776	7.72 ± 0.17	-0.39 ± 0.22	-3.44 ± 0.15
NGC 3423	8.14 ± 0.23	-0.74 ± 0.29	-3.62 ± 0.13
NGC 4254	7.75 ± 0.17	-0.41 ± 0.27	-3.38 ± 0.15
NGC 6689	8.35 ± 0.28	-0.94 ± 0.27	-3.39 ± 0.19

Table A.2: Chemical abundances of composite galaxies that only present reliable results considering the AGN model.

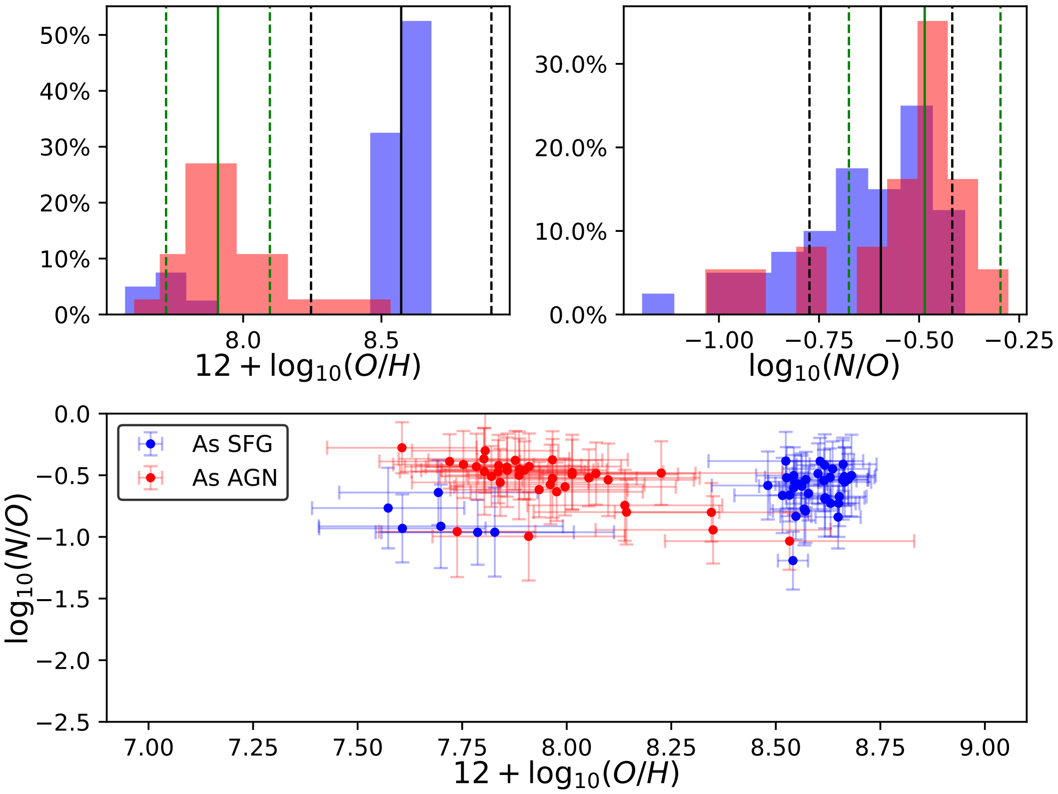

Figure A.1: CHemical abundances obtained for composite galaxies: $12+\log_{10}(O/H)$ (top left) and $\log_{10}(N/O)$ (top right). For both histograms, the blue (pink) color represent the results considering the star-forming (AGN) model. The solid lines represent the median values and the dashed lines the standard deviations (black color if they are treated as SFG and green if they are treated as AGN). The bottom plot shows $\log_{10}(N/O)$ vs $12+\log_{10}(O/H)$.

The diagram N/O vs O/H (see Figure A.1, bottom panel) shows that composites treated as SFG fit the behavior of the star-forming galaxies discussed in subsection 3.3.2. If they are considered as AGN, the range of values better fits the distribution seen in LINERs. In order to quantify these trends, a KS-test was done for each spectral class (see results in Table A.3). The p-values obtained for $12+\log_{10}(O/H)$ reject the hypothesis that composite galaxies are either star-forming galaxies, Seyferts 2 or LINERs, while the results obtained for $\log_{10}(N/O)$ show that they could be considered as AGN. However, the extremely low median value $12+\log_{10}(O/H) = 7.91 \pm 0.19$ obtained for composites treated as AGN reveal that they cannot be grouped in that spectral types.

The results for the oxygen abundance in composite galaxies show that, by setting the AGN SED, the

Distributions	**O/H***	**N/O***	**O/H****	**N/O****
O/H Star-forming	$6.5 \cdot 10^{-11}$	-	-	-
N/O Star-forming	-	$6.12 \cdot 10^{-4}$	-	-
O/H Seyferts 2	-	-	$2.1 \cdot 10^{-9}$	-
N/O Seyferts 2	-	-	-	0.11
O/H LINERs	-	-	$1.8 \cdot 10^{-12}$	-
N/O LINERs	-	-	-	0.0041

Table A.3: P-values obtained trough a KS-test for each distribution.*Composite galaxies treated as SFG.**Composite galaxies treated as AGN.

chemical abundance is lower (see Figure A.1, top left panel and Table 3.8). This result contrasts with the distributions for Seyferts 2 and LINERs, which tend to present higher abundances than star-forming regions, suggesting that most composite galaxies are indeed star-forming.

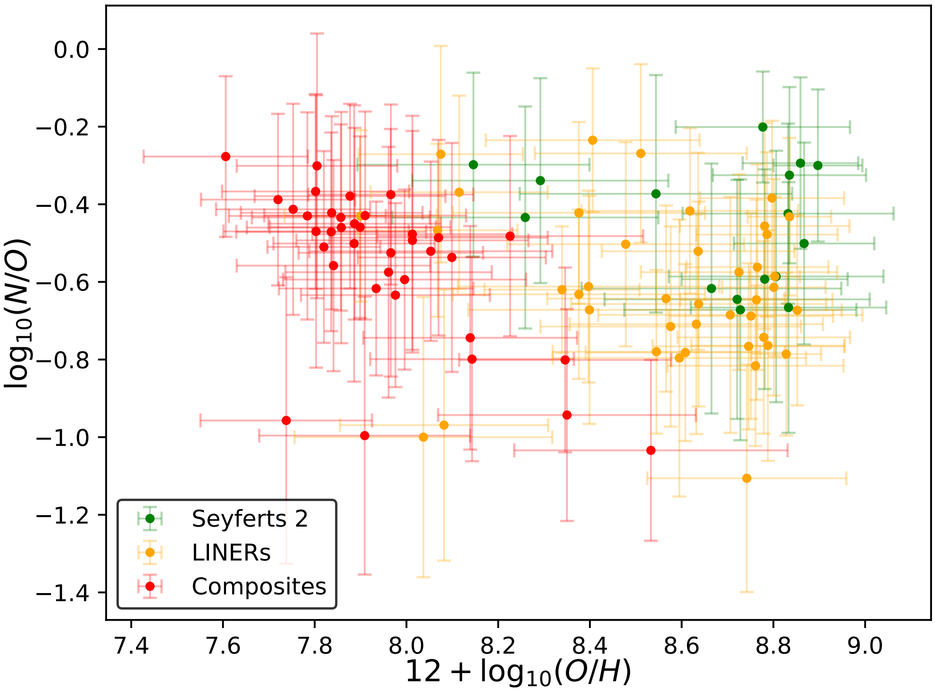

Figure A.2: Diagram $\log_{10}(N/O)$ vs $12 + \log_{10}(O/H)$ for AGN and composites treated as AGN.

The nitrogen to oxygen abundance ratio presents a slightly increase from the star formation SED to the AGN one (see Figure A.1, top right panel). This increase for the AGN model is in good agreement with the range of values obtained for both Seyferts 2 and LINERs (see Table 3.8), and is also reinforced by the KS-test.

While there is no distinction in the $12 + \log_{10}(O/H)$ vs $\log_{10}(N/O)$ diagram between Seyferts 2 and LINERs, if composite galaxies are included (see Figure A.2), a clear separation between AGN and composites can be seen. This is a expected result since the AGN SED provides lower values for the oxygen abundance.

X-ray observations of composite galaxies [Della Ceca et al. (2001); Panessa et al. (2005)] show compact central sources in those objects and AGN emission. In addition, several studies have been done in order to determine the AGN contribution for the composite galaxies in both optical [Davies et al. (2014b,a); Thomas et al. (2019)] and infrared [Imanishi et al. (2011)] ranges. In this complex picture, the extremely low chemical abundances $12 + \log_{10}(O/H)$ obtained when they are considered as AGN reveal that they are more likely star-forming galaxies, but there are also some galaxies (NGC 2776, NGC 3423, NGC 4254 and NGC 6689) that can only be treated as AGN.

A.2 Ionization parameter

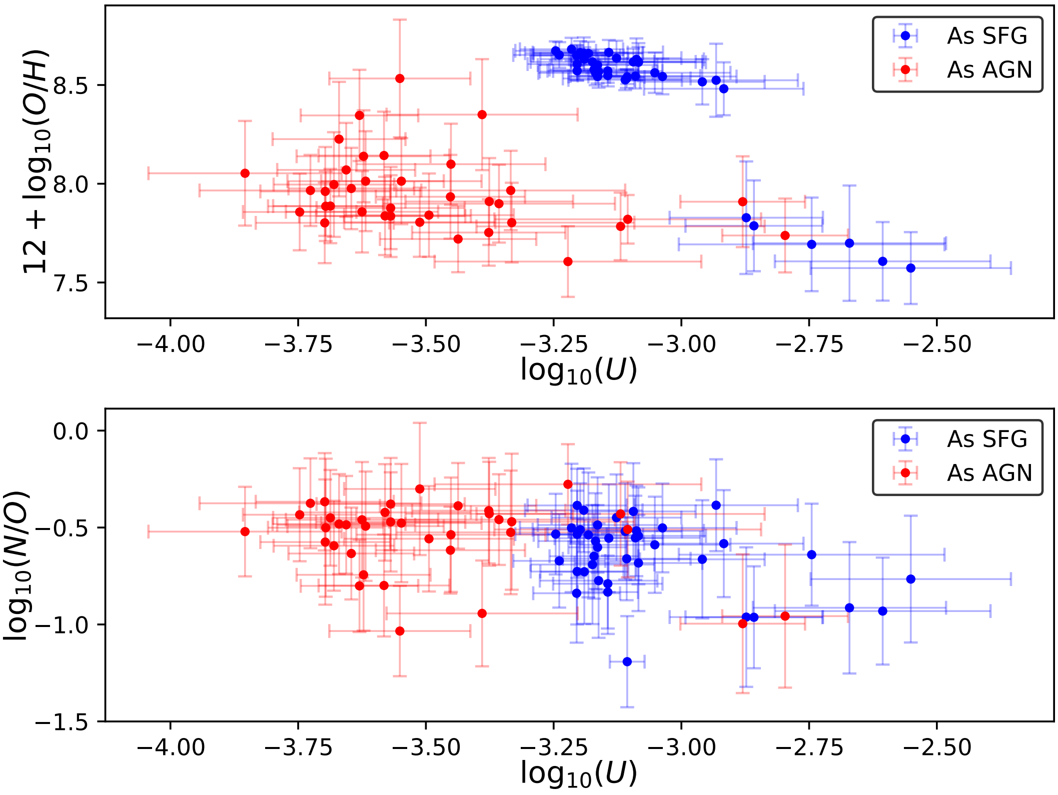

Figure A.3: Variation of the chemical abundances $12+\log_{10}(O/H)$ and $\log_{10}(N/O)$ with the ionization parameter $\log_{10}(U)$ in composite galaxies.

For composites that can only be treated as SFG, their ionization parameters (see Table A.1) are compatible with the range of values obtained for star-forming galaxies. In the case of composites that can only be treated as AGN, those values (see Table A.2) are only compatible with the range of values for LINERs. The median value for the composites treated as SFG is $\log_{10}(U) = -3.13 \pm 0.17$, with a minimum of -3.25 and a maximum of -2.55, while when they are treated as AGN, the median value drops to $\log_{10}(U) = -3.57 \pm 0.23$, ranging from -3.85 to -2.80. The results from the KS-test show that the p-value comparing composites as SFG and star-forming galaxies is low ($4.1 \cdot 10^{-5}$) but also comparing composites as AGN with Seyferts 2 and LINERs (obtaining $1.4 \cdot 10^{-13}$ and $4.92 \cdot 10^{-4}$, respectively). However, the upper limit found in composites treated as SFG is in good agreement with that obtained for star-forming galaxies (see subsection 3.4.1 for a more detailed discussion).

The analysis of the chemical abundances as a function of the ionization parameter reveals that $12 + \log_{10}(O/H)$ decreases (the Pearson correlation coefficient is $r = -0.92$) with $\log_{10}(U)$ for composites treated as SFG (see Figure A.3, the top panel). A similar result is obtained for star-forming galaxies (see subsection 3.4.1). However, either they are treated as SFG or as AGN, there is no correlation between $\log_{10}(N/O)$ and $\log_{10}(U)$ (see Figure A.3, bottom panel), being the correlation coefficients $r = -0.39$ (star-forming model) and $r = -0.30$ (AGN model).

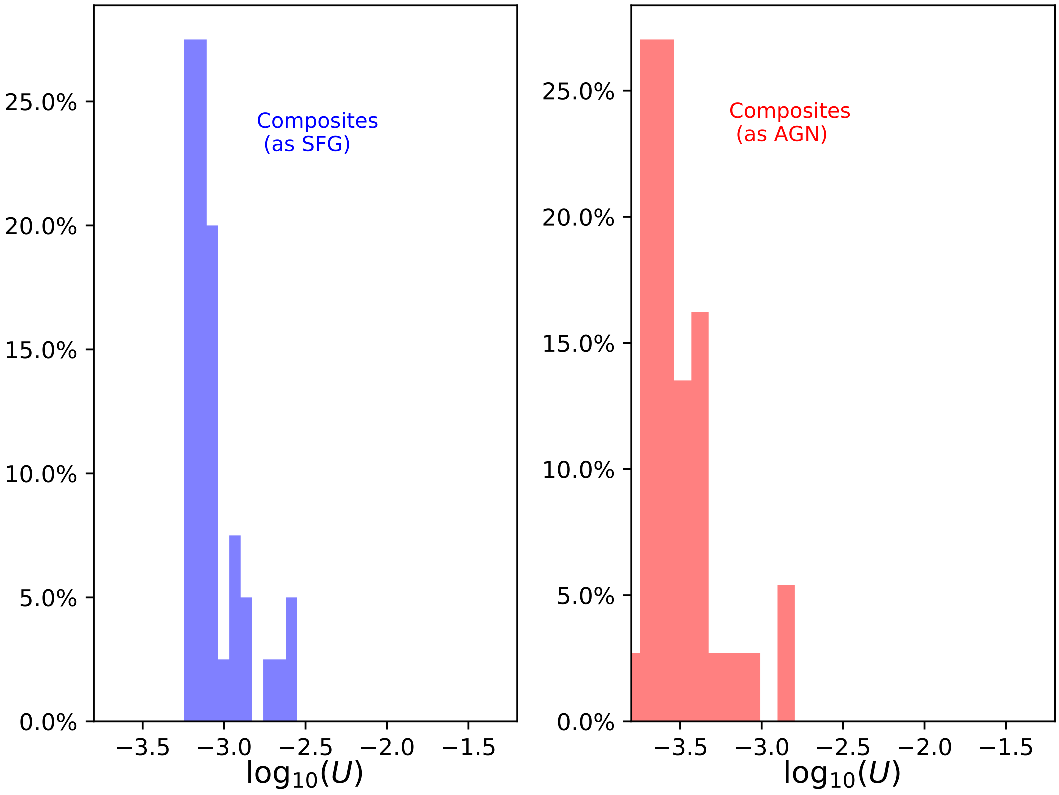

Figure A.4: Distributions of the ionization parameter $\log_{10}(U)$ for composite galaxies under both SEDs.

A.3 Metallicity and host galaxy properties

From our study in subsections A.1 and A.2, three different groups of composite galaxies should be considered. The first group is made up from those composite galaxies (7 in total) that only present reliable determinations of their chemical abundances under the SFG model (hereinafter *SFG composites*), that are listed in Table A.1. The second group is composed by those galaxies (4 in total) that only present reliable determinations under the AGN model (hereinafter *AGN composites*) and they are listed in Table A.2. The remaining composite galaxies (33 in total) constitute the third group, and they are characterized for having reliable determinations under both models, SFG and AGN. This group maintains the denomination *composite galaxies*, and the terminology introduced in subsection 3.2.3 (treated as SFG or treated as AGN) is used to distinguish between the results from the two models.

A.3.1 Morphology

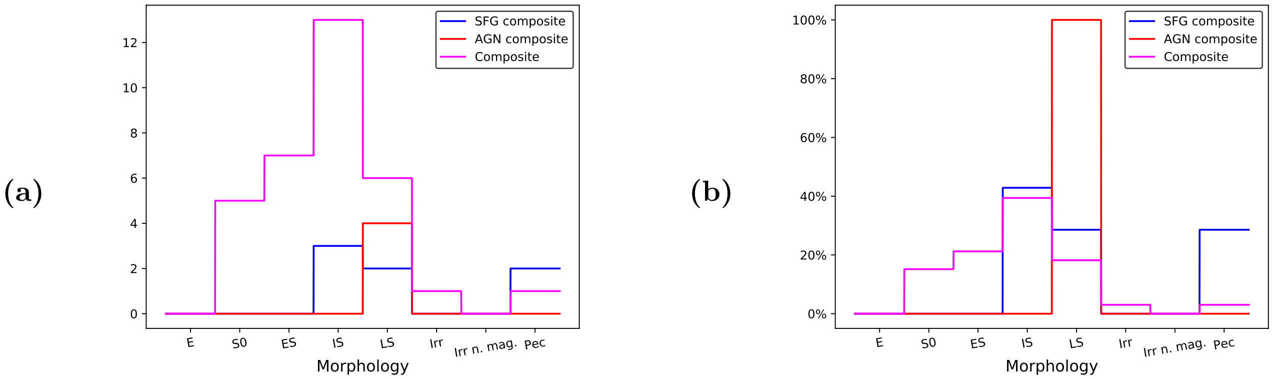

Figure A.5: Absolute (a) and relative (b) distributions of the morphology (considering only the types defined in Table 4.1) for the three groups of composite galaxies.

Group	Number	Perc.* (%)	Median	Std. Dev.*	Minimum	Maximum
SFG composite	7	15.9	5.00	0.76	3	99
AGN composite	4	9.1	5.50	0.83	5	7
LINERs	33	75	3.00	2.66	-3	99

Table A.4: Morphological statistics for composite galaxies. *The percentage (Perc.) is calculated considering only the sample of 44 composite galaxies. **The standard deviationis calculated considering only galaxies with morphological types $T \leq 10$.

Considering the distribution of composite galaxies for the different morphological types (see Figure A.5 and Tables A.4 and A.5), roughly ≈ 80% of composites present a spiral morphology (mainly I.S.). While this result is in good agreement with the previous study by Panessa et al. [2005], it contrasts with that by Ho et al. [1997b], who obtained that > 30% of composite galaxies are hosted by elliptical and lenticular galaxies. In our sample, no composite galaxy has an elliptical morphology and just only 11.4% of them are lenticulars. Although Ho et al. analyzed the Palomar Survey, this discrepancy might be explained due to the filters applied to construct our sample (see section 2.2) and the differing criterion to classify composite galaxies (see section 1.3). The KS-test shows that the morphological distribution in composite

Morphology	**SFG Composite**	**AGN Composite**	**Composite**	**Total**	**Percentage (%)**
E	0 (0.0%)	0 (0.0%)	0 (0.0%)	0	0.0
S0	0 (0.0%)	0 (0.0%)	5 (15.2%)	5	11.4
ES	0 (0.0%)	0.0 (0.0%)	7 (21.2%)	7	15.9
IS	3 (42.8%)	0 (0.0%)	13 (39.4%)	16	36.4
LS	2 (28.6%)	4 (100.0%)	6 (18.2%)	12	27.3
Irr	0 (0.0%)	0 (0.0%)	1 (3.0%)	1	2.3
Irr. Non. Mag.	0 (0.0%)	0 (0.0%)	0 (3.0%)	0	0.0
Pec	2 (28.6%)	0 (0.0%)	1 (3.0%)	3	6.8
Sum	7 (100%)	4 (100%)	33 (100%)	44	100.0

Table A.5: Distribution of composite galaxies for each morphological type.

galaxies is similar to Seyferts 2 (p-value ≈ 0.54), but clearly differs from those observed in star-forming galaxies (p-value ≈ 0.00084) and LINERs (p-value ≈ 0.0054).

In the case of SFG composites, the chemical abundance $12 + \log_{10}(O/H)$ presents compatible values (within the errors) for both IS and peculiar galaxies, 8.61 ± 0.44 and 8.12 ± 0.55, respectively (see Figure A.6 (a)). However, it drops to $12 + \log_{10}(O/H) = 7.76 \pm 0.06$ in LS galaxies. A similar behavior is observed for $\log_{10}(N/O)$ (see Figure A.6 (b)). The ionization parameter $\log_{10}(U)$ increases from peculiar and IS to LS galaxies. This behavior is expected in star-forming galaxies since $12+\log_{10}(O/H)$ is anti-correlated with the ionization parameter (see subsection 3.4.1 for more details). This change observed in LS galaxies must be confirmed with larger samples, since only two galaxies (NGC 697 and NGC 3367) have this morphology.

Analyzing AGN composites, which only have a LS morphology, both chemical abundances are compatible with the results obtained for SFG composites, but the ionization parameter (see Figure A.6 (c)) is lower than in SFG composites, as a consequence of the change in the SED (from star-forming to AGN).

Finally, composites show little variation among the different morphological types in their chemical abundances and ionization parameter. This result is independent of considering either a star forming or an AGN SED. If composite galaxies are treated as SFG, their chemical abundances agree with those obtained for SFG galaxies, with the exception of LS galaxies, where the results for SFG and AGN composite galaxies are only compatible with those obtained for composite galaxies treated as AGN.

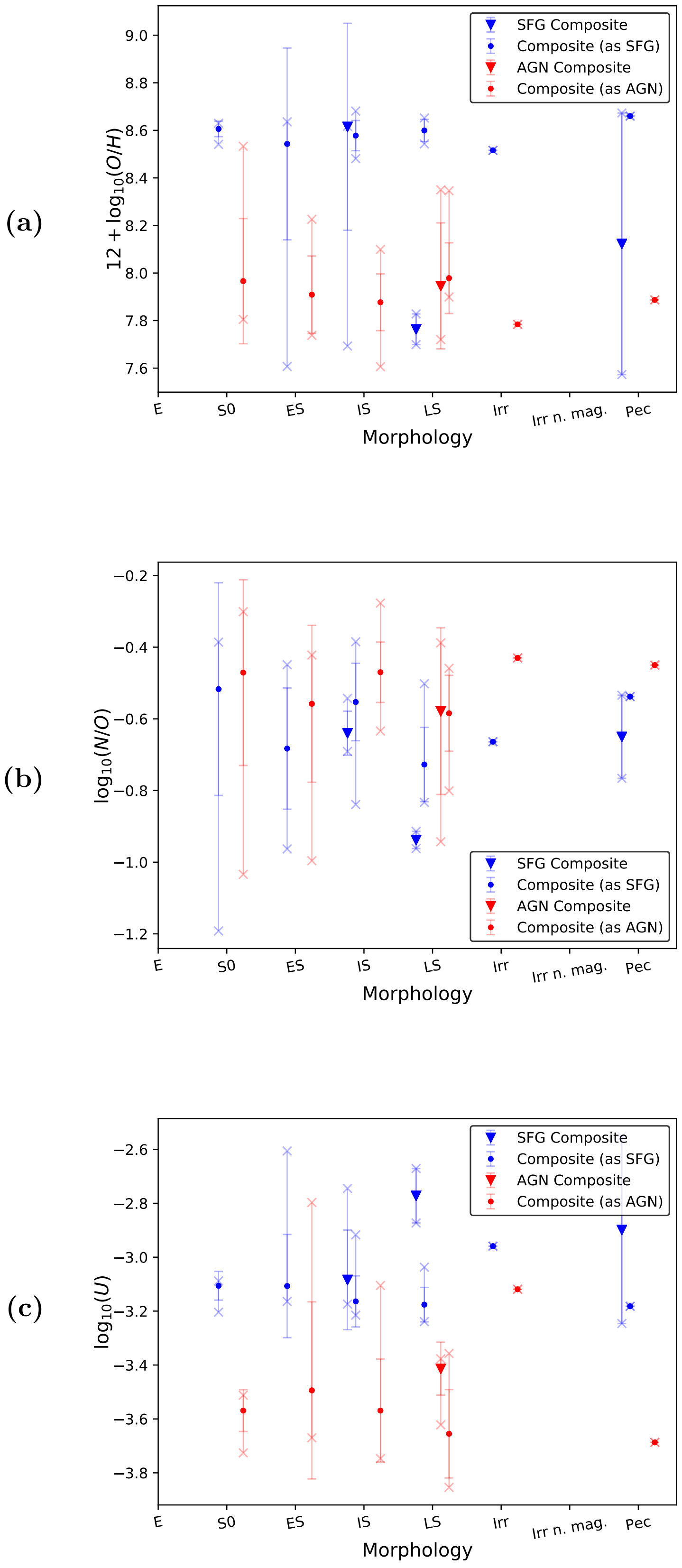

Figure A.6: Chemical abundances $12+\log_{10}(O/H)$ (a) and $\log_{10}(N/O)$ (b) and ionization parameter $\log_{10}(U)$ (c) for each morphological type. The points correspond to the median value, the error bars marked with "-" denote the standard deviation and the error bars marked with "x" the minimum and maximum value for each morphology.

A.3.2 Absolute B-magnitude

The distribution of M_B^0 for composite galaxies is shown in Figure A.7 and Table A.6. For SFG composites and composite galaxies, the distribution is almost symmetric with the same median value $M_B^0 = -20.10$. This symmetry, clearly seen for star-forming galaxies and AGN (see section 4.2), is completely broken for AGN composites, likely due to the small size of the sample (4 galaxies). The median values obtained are closer to those obtained for AGN ($M_B^0 < -19.9$) than for star-forming galaxies ($M_B^0 = -19.48$). In addition, the KS-test shows that the distribution of M_B^0 for composites differs from that obtained for star-forming galaxies (p-value ≈ 0.002) but it is pretty similar to those obtained for both Seyferts 2 (p-value ≈ 0.33) and LINERs (p-value ≈ 0.93).

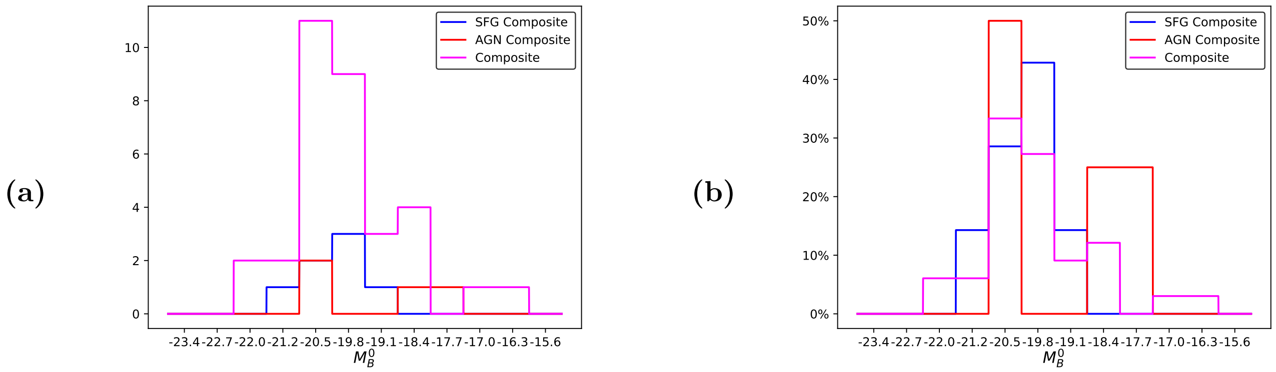

Figure A.7: Absolute (a) and relative (b) distributions of absolute B-magnitudes (M_B^0) corrected from reddening for composite galaxies.

Group	Number	Median	Std. Dev.	Min.	Max.
SFG composite	7	-20.10	0.66	-21.21	-19.05
AGN composite	4	-19.77	1.41	-20.85	-17.58
Composite	33	-20.10	1.23	-21.74	-16.01

Table A.6: Statistics of the absolute B-magnitude for the different groups of composite galaxies.

Considering the star formation model in composite galaxies, $12 + \log_{10}(O/H)$ remains constant at the solar value ≈ 8.6 (see Figure A.8 (a)), which is the behavior observed in star-forming galaxies at high luminosities ($M_B^0 < -19.5$). However there is a group of six galaxies (NGC 63, NGC 2268, NGC 2782, NGC 3367, NGC 4123 and NGC 6500) that present sub-solar abundances ($12 + \log_{10}(O/H) < 8.0$). The ionization parameter $\log_{10}(U)$ (see Figure A.8 (e)) does not present any correlation with M_B^0, being the Pearson coefficient $r = 0.056$. The chemical abundance ratio $\log_{10}(N/O)$ shows a slightly increase, but the correlation is low ($r = 0.37$).

Considering the AGN model for composite galaxies, the ionization parameter $\log_{10}(U)$ (see Figure A.8 (f)) does not correlate with M_B^0 ($r = 0.021$), similarly to what is obtained under the star formation model. The chemical abundance ratio $\log_{10}(N/O)$ seems to increase with M_B^0, but the correlation is not significant

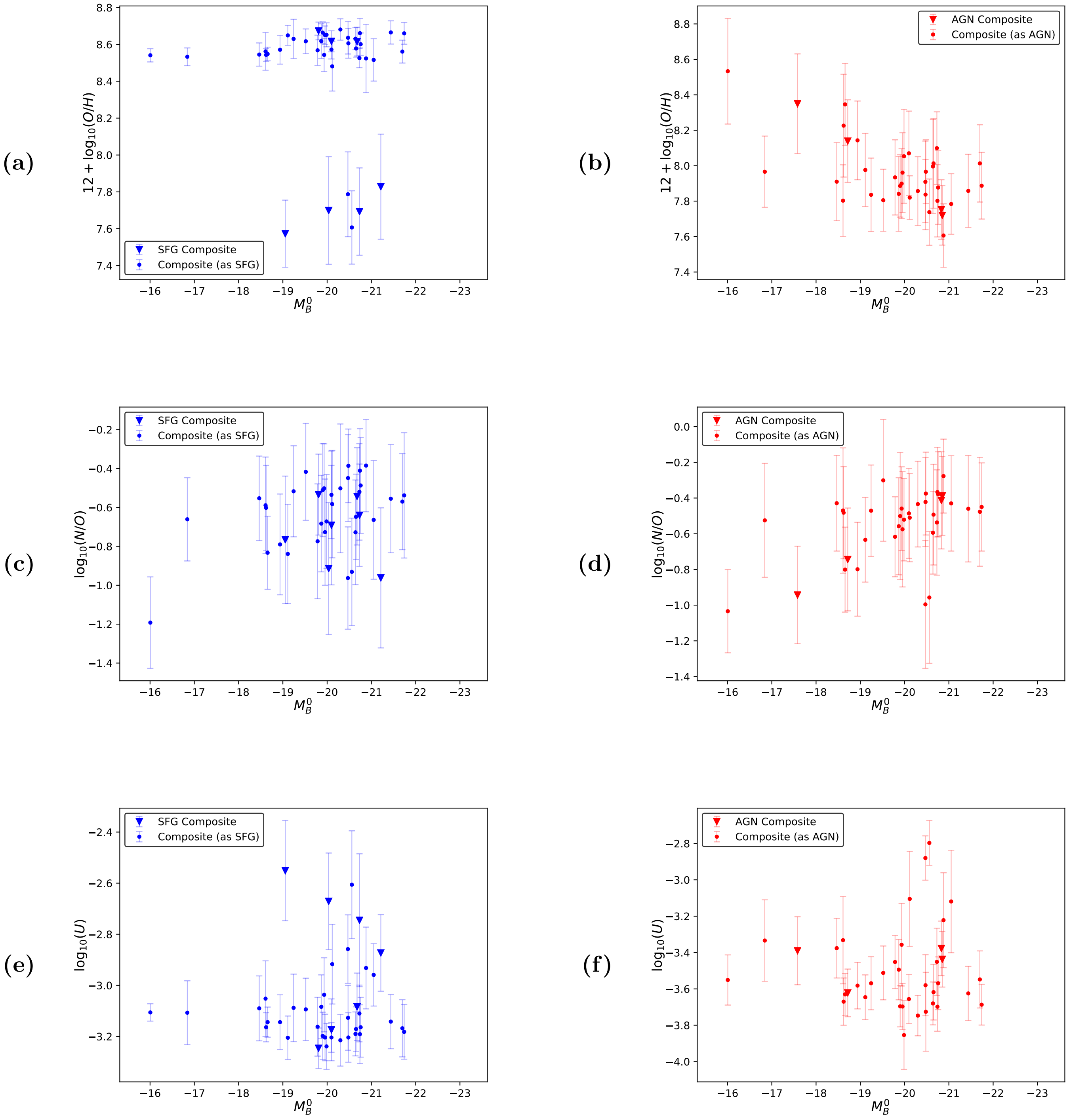

Figure A.8: Chemical abundances $12+\log_{10}(O/H)$ (a) and (b), $\log_{10}(N/O)$ (c) and (d) and ionization parameter $\log_{10}(U)$ (e) and (f) vs the corrected absolute B-magnitude (M_B^0). The left column shows the results for SFG composites and composites treated as SFG and the right column those for AGN composites and composites treated as AGN.

($r = 0.48$). Figure A.8 (b) shows that there is a slightly decrease in $12 + \log_{10}(O/H)$ with the luminosity, although it is not significant (the Pearson correlation coefficient is $r = 0.63$).

A.3.3 H_α luminosity

The distribution of the corrected H_α luminosity (see Figure A.9 and Table A.7) shows that SFG composites present higher median values than other composite galaxies. The p-values obtained through the KS-test show that the distribution of $L(H_\alpha)$ in composite galaxies is similar to that obtained for Seyferts 2 (p-value $\approx$ 0.88), but clearly differs from that observed in star-forming galaxies (p-value $\approx$ 0.0024) or LINERs (p-value $\approx$ 0.00018).

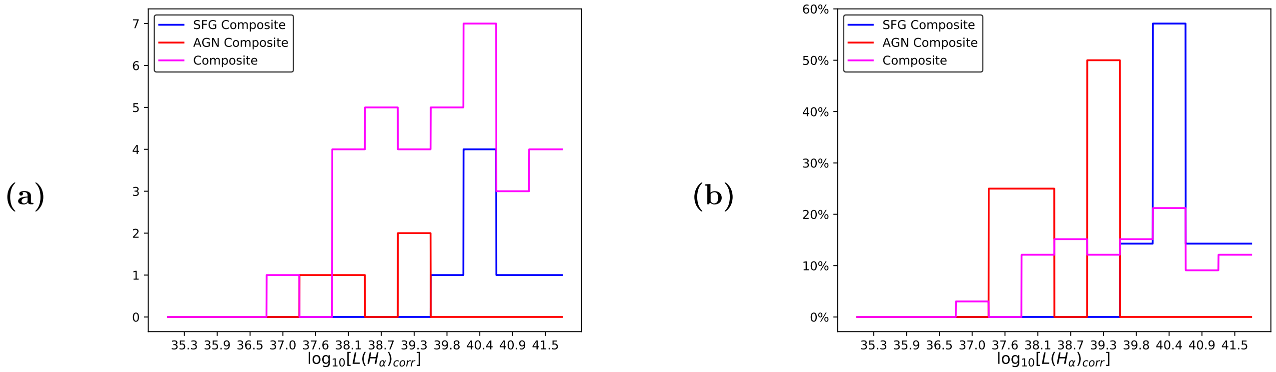

Figure A.9: Absolute (a) and relative (b) distributions of H_α luminosities ($L(H_\alpha)_{corr}$) corrected from reddening for composite galaxies.

Spectral type	Number	Median	Std. Dev.	Min.	Max.
SFG composite	7	40.44	0.53	39.58	41.37
AGN composite	4	38.64	0.76	37.85	39.53
Composite	33	39.78	1.11	37.29	41.77

Table A.7: Statistics of $\log_{10}[L(H_\alpha)_{corr}]$ for composite galaxies.

Considering the star formation model for composite galaxies, $12 + \log_{10}(O/H)$ remains constant for all luminosities, the behavior observed in star-forming galaxies for luminosities $L(H_\alpha) > 10^{39}\ erg \cdot s^{-1}$. Again, the group of six galaxies with sub-solar chemical abundances is seen in Figure A.10. The chemical abundance ratio $\log_{10}(N/O)$ and the ionization parameter do not correlate (the correlation coefficients are in both cases below $r < 0.3$) with H_α luminosity (see Figure A.10 (c) and (e)), similarly to what is observed in star-forming galaxies.

If the AGN model is considered for composite galaxies, the chemical abundance ratio $\log_{10}(N/O)$ is practically constant (see Figure A.10 (b)). The chemical abundance $12 + \log_{10}(O/H)$ shows an apparent anti-correlation (the Pearson correlation coefficient is $r = -0.66$) with $L(H_\alpha)$, behavior that contrasts with that obtained for Seyferts 2 and LINERs, where both quantities are not correlated. The ionization parameter is little correlated ($r = 0.27$) with $L(H_\alpha)$, as it was obtained for the star formation model.

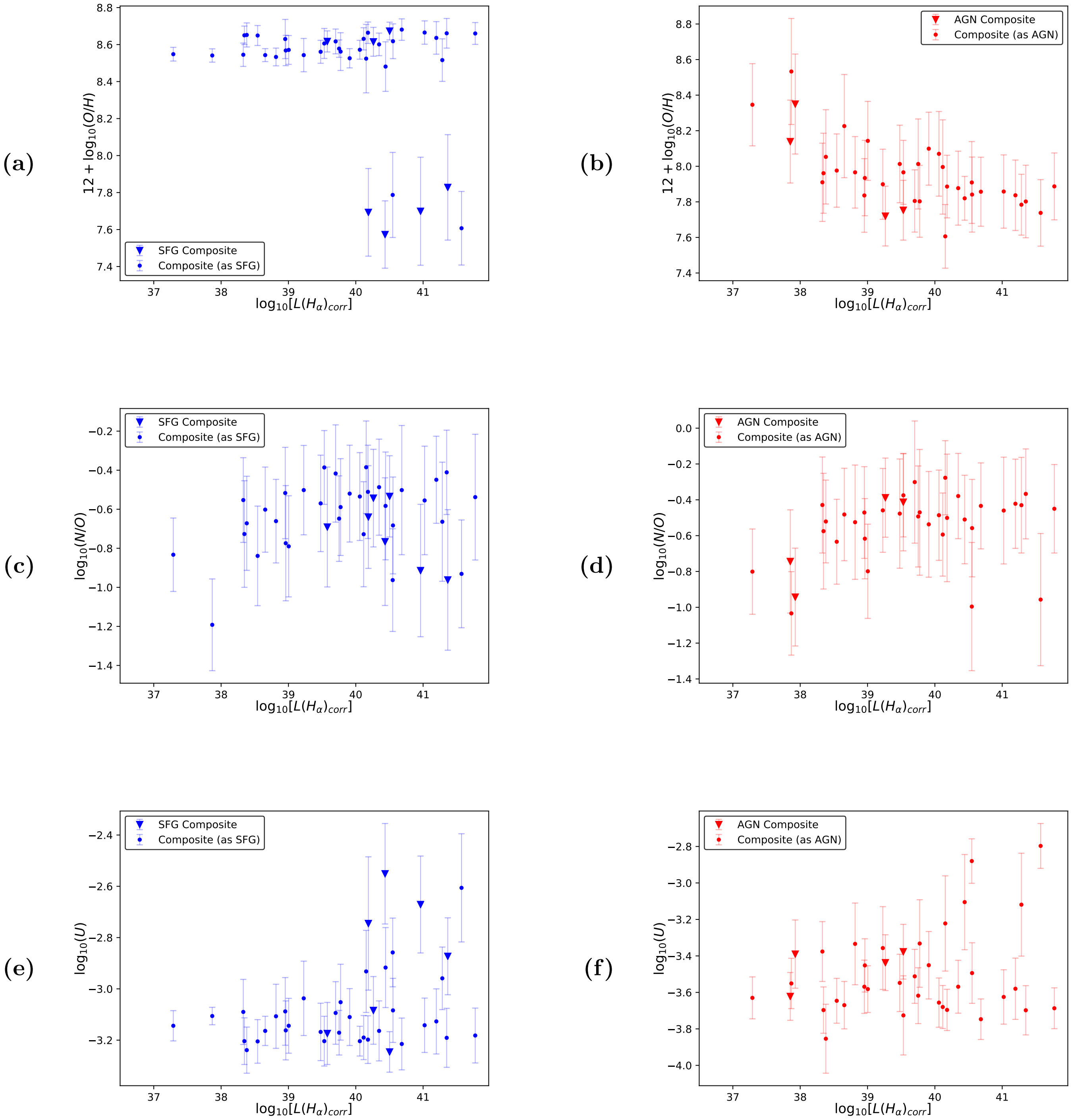

Figure A.10: Chemical abundances 12+$\log_{10}(O/H)$ (a) and (b), $\log_{10}(N/O)$ (c) and (d) and ionization parameter $\log_{10}(U)$ (e) and (f) vs the corrected H_α luminosity ($\log_{10}[L(H_\alpha)_{corr}]$). The left column shows the results for SFG composites and composites treated as SFG and the right column those for AGN composites and composites treated as AGN.

A.3.4 Supermassive black hole

This study is focused on AGN composites and composites treated as AGN, where the determination of the mass of the SMBH by Equation (1.2) is applied. This relation is found for galaxies presenting bulge structure in their nuclei, so the composite galaxy NGC 2342, which has a spiral peculiar morphology, is excluded from this study, since its morphology is irregular. In addition, 4 galaxies (NGC 404, NGC 2776, NGC 3917 and NGC 6689) present a black hole mass below 10^5 $M_\odot$, the low limit for SMBH [Greene et al. (2019)], so they are omitted from this study too. The median value $M_{SMBH} = 10^{6.86\pm0.97}$ $M_\odot$ is below that observed for Seyferts 2 ($10^{7.48\pm0.84}$ $M_\odot$) and LINERs ($10^{8.17\pm0.91}$ $M_\odot$), and the KS-test suggests that the M_{SMBH} distribution in composite galaxies differs from that in Seyferts 2 (p-value $\approx$ 0.053) and LINERs (p-value $\approx$ 0.00069).

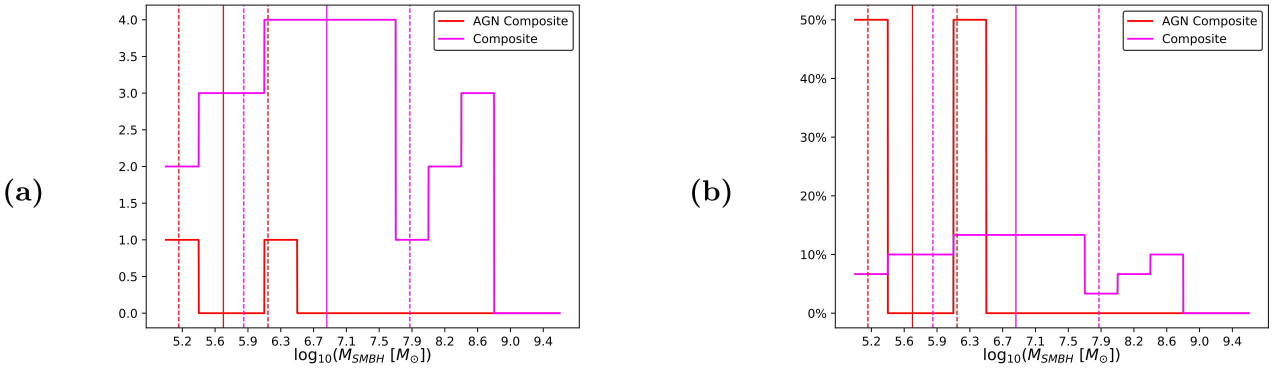

Figure A.11: Absolute (a) and relative (b) distributions of the SMBH masses $\log_{10}(M_{SMBH}\,[M_\odot])$ for composite galaxies. The solid vertical lines represent the median values and the dashed vertical lines the standard deviations.

Group	**Number**	**Median**	**Std. Dev.**	**Min.**	**Max.**
AGN composite	2	5.66	0.52	5.14	6.18
Composite	30	6.86	0.97	5.13	8.48

Table A.8: Statistics of $\log_{10}(M_{SMBH}\,[M_\odot])$ for composite galaxies.

As it was obtained for Seyferts 2 and LINERs, the ionization parameter does not correlate (the Pearson coefficient is $r = 0.17$) with the SMBH mass (see Figure A.12 (c)). However, the chemical abundances $12 + \log_{10}(O/H)$ and $\log_{10}(N/O)$ practically remain constant for all masses (see Figure A.12 (a) and (b)), contrasting with the dispersion of values observed for both Seyferts 2 and LINERs.

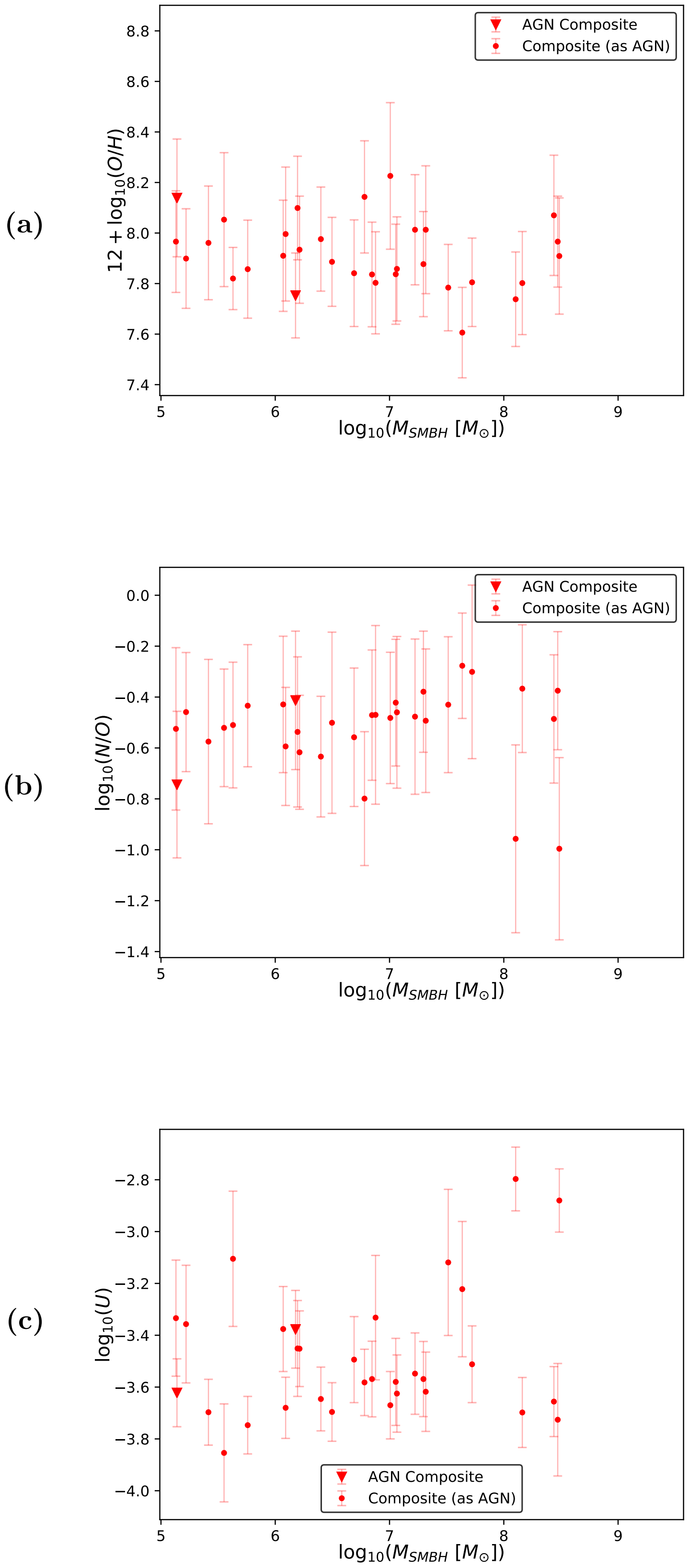

Figure A.12: Chemical abundances $12 + \log_{10}(O/H)$ (a) and $\log_{10}(N/O)$ (b) and ionization parameter $\log_{10}(U)$ (c) vs the SMBH mass M_{SMBH} for AGN composites and composites treated as AGN.

A.3.5 Stellar mass

The distribution of stellar masses for composites is presented in Figure A.13 and Table A.9. The median value, $M_* = 10^{9.49\pm0.55}$ $M_\odot$, is slightly higher than that obtained for star-forming galaxies ($10^{9.03\pm0.75}$) and similar to that for Seyferts ($10^{9.65\pm1.03}$), a result already reported by previous studies [Kauffmann et al. (2003); Kewley et al. (2006)]. The KS-test shows that the stellar mass distribution in composite galaxies is similar to that observed for Seyferts 2 (p-value ≈ 0.38), but pretty different from that obtained for star-forming galaxies (p-value $\approx 2.3 \cdot 10^{-6}$) or LINERs (p-value ≈ 0.00011).

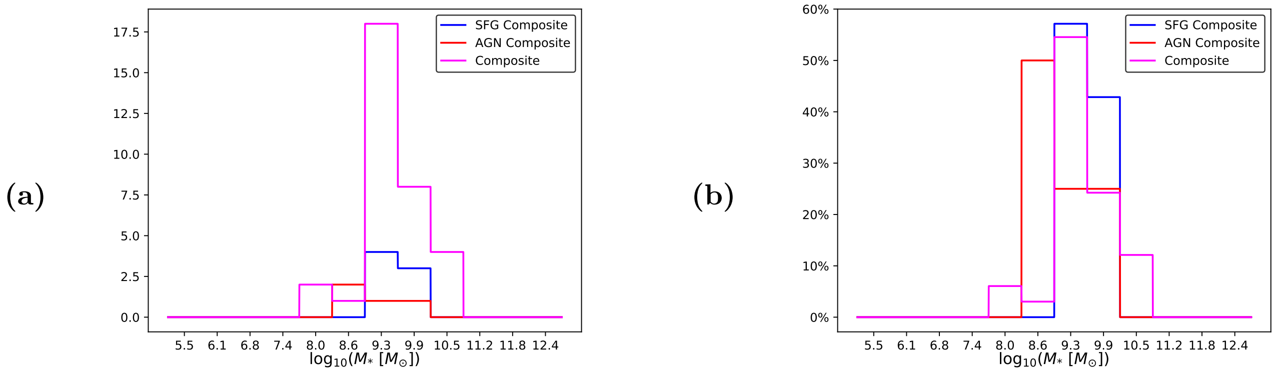

Figure A.13: Absolute (a) and relative (b) distributions of the stellar masses (M_*) for composite galaxies.

Spectral type	Number	Median	Std. Dev.	Min.	Max.
SFG composite	7	9.56	0.37	8.98	9.99
AGN composite	4	9.04	0.55	8.54	9.94
Composite	33	9.47	0.55	7.99	10.309

Table A.9: Statistics of $\log_{10}(M_*\ [M_\odot])$ for composite galaxies.

Considering the star formation model, the plots of the chemical abundances and ionization parameter vs the stellar mass presented in Figure A.14 show that $\log_{10}(U)$ does not correlate with the stellar mass (the correlation coefficients are $r = -0.10$) and the chemical abundance ratio $\log_{10}(N/O)$ is little correlated ($r = 0.45$). The chemical abundance $12 + \log_{10}(O/H)$ practically remains constant.

For the AGN model, $\log_{10}(U)$ does not correlate with the stellar mass ($r = -0.013$), the chemical abundance $12+\log_{10}(O/H)$ seems to be anti-correlated for low stellar masses ($M_* < 10^9$) and the chemical abundance ratio $\log_{10}(N/O)$ shows a slightly increase, but both Pearson correlation coefficients are not significant ($r = -0.38$ and $r = 0.38$, respectively).

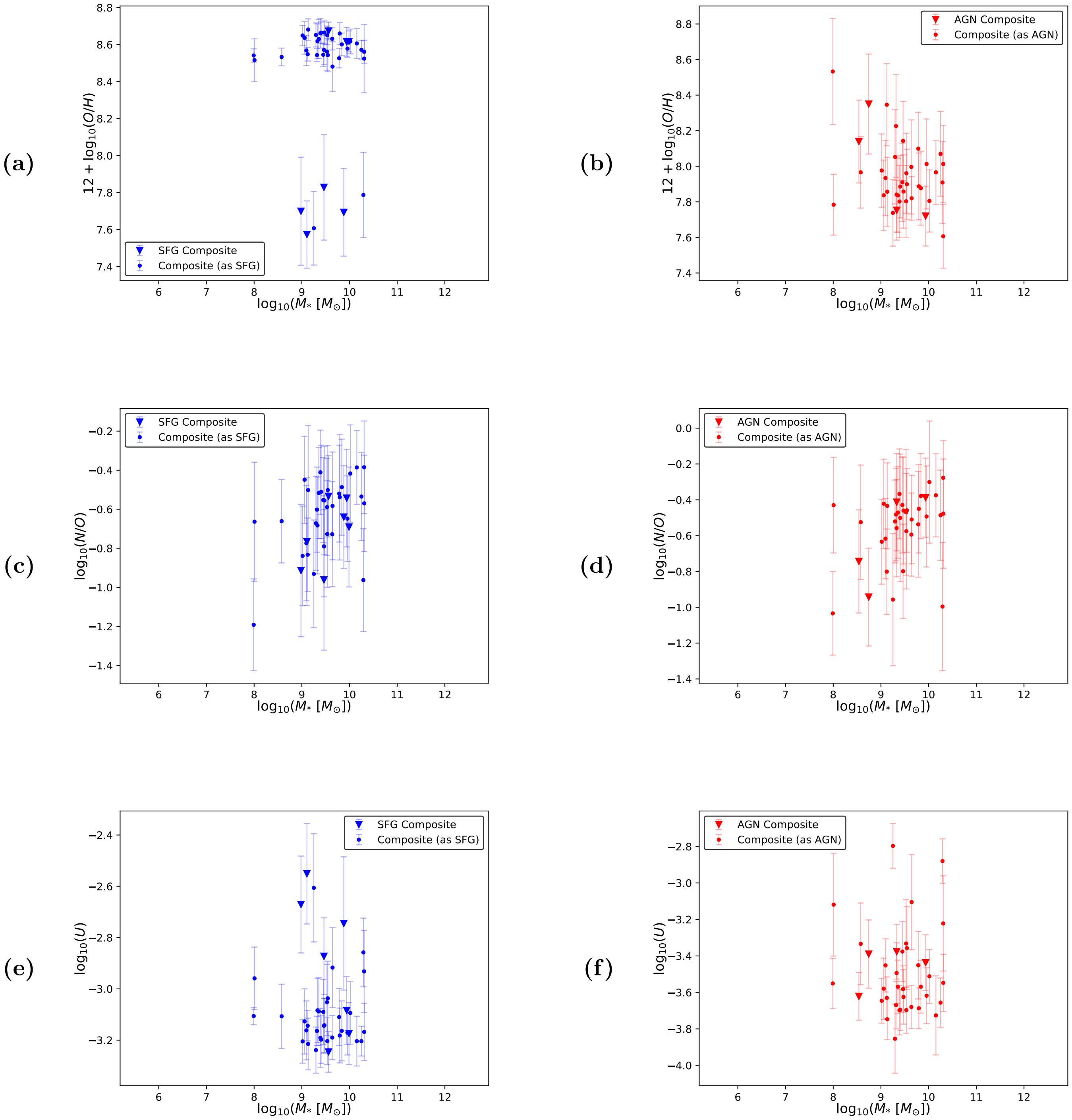

Figure A.14: Chemical abundances 12+$\log_{10}(O/H)$ (a) and (b), $\log_{10}(N/O)$ (c) and (d) and ionization parameter $\log_{10}(U)$ (e) and (f) vs the stellar mass ($\log_{10}(M_* [M_\odot])$). The left column shows the results for SFG composites and composites treated as SFG and the right column those for AGN composites and composites treated as AGN.